

QATAR UNIVERSITY

COLLEGE OF ENGINEERING

EXPERIMENTAL AND CFD INVESTIGATION OF SOLAR CENTRAL RECEIVER

TUBES

BY

SALMAN MOHAMMAD ISMAIL

A Thesis Submitted to  
the Faculty of the College of

Engineering

in Partial Fulfillment

of the Requirements

for the Degree of

Masters of Science in Mechanical Engineering

January 2018

© 2018 Salman Mohammad Ismail. All Rights Reserved.

## COMMITTEE PAGE

The members of the Committee approve the Thesis of Salman Mohammad

Ismail defended on 16/12/2017.

---

Dr. Saud Abdul Ghani  
Thesis/Dissertation Supervisor

---

Dr. Samer Fikry Ahmed  
Committee Member

---

Dr. Tarek Echehki  
Committee Member

Approved:

---

Khalifa Al-Khalifa, Dean, College of Engineering

## ABSTRACT

ISMAIL, SALMAN, M, Masters : January : 2018, Masters of Science in Mechanical Engineering

Title: EXPERIMENTAL and CFD INVESTIGATION of SOLAR CENTRAL RECEIVER TUBES

Supervisor of Thesis: Saud, A, Ghani.

Lower electricity cost corresponds to high efficiency, which in turn corresponds to high operating temperatures in Concentrated Solar Power technology. Central receiver of such system constitutes 15% of the cost and plays an important role in achieving high operating temperatures. Central receiver systems are composed of tubes with heat transfer fluid flowing inside them that transports heat from radiation on the outer wall of tubes. Circular cross-sectional tubes are conventionally used for this application, but many different variable geometry tubes have been proposed for better heat transfer. Numerous experiments have shown the enhanced heat transfer behavior of different corrugated tubes. This work proposes a tube of new cross-sectional geometry and performs experiment using water as heat transfer fluid. The experiment is conducted on four different samples of corrugated tubes adopted from literature and compared to a circular tube and a new proposed tube. The experimental and CFD results are compared and reported. It is found that the new tube design can be used for such heat transfer applications but is not an ideal option. Meanwhile, corrugated tubes have higher heat transfer than circular tube, but not without the addition of extra material and pressure drop. If the material is to be kept similar for all tubes, circular tube is found to be the best option for central receiver systems.

## DEDICATION

*Dedicated to my parents and siblings who have always been my source of motivation and confidence.*

## ACKNOWLEDGMENTS

All praise be to Almighty ALLAH, the most beneficent and the most merciful. My warm gratitude extends to Department of Mechanical & Industrial Engineering Qatar University for providing me an opportunity and supporting me in my pursuit of Masters of Science in Mechanical Engineering. This would not be possible without Dr. Saud A. Ghani's determined supervision, proficient guidance, and sincere motivation. Dr. Saud A. Ghani has always inspired me with his ideas and ways to solve problems. I am also lucky to be part of a very friendly and professional environment. I am grateful to my colleagues who have always encouraged and supported me with great enthusiasm, especially Engr. Mohammad Mustafa Rashwan who assisted me in the fabrication of much of the apparatus. I am also thankful to Engr. Ayman Mohamed Abdelhalim for lending me his computational resource to solve some of my important simulations. I am also very grateful to Engr. Seifelislam Mahmoud Gamaledin, Dr. Esmail Mohamed ElBialy, Engr. Foteini Bakochristou, for their support, they would happily listen to my work and make valuable suggestions. They supported me whenever I needed help and answered whenever I had queries, with great enthusiasm.

I have learned a great deal from everyone around me. But this section would be incomplete without making mention of my parents and all the teachers I have ever had, without whom, I would not be able to achieve any bit of this.

## TABLE OF CONTENTS

DEDICATION .....	iv
ACKNOWLEDGEMENTS .....	v
LIST OF TABLES .....	ix
LIST OF FIGURES .....	x
<b>CHAPTER 1: INTRODUCTION .....</b>	<b>1</b>
<b>1.1 Renewable Energy .....</b>	<b>3</b>
<b>1.1.1 Solar Power .....</b>	<b>4</b>
<b>1.1.1.1 Solar PV .....</b>	<b>5</b>
<b>1.1.1.2 Concentrated Solar Power (CSP) .....</b>	<b>5</b>
<b>1.1.1.2.1 Types of CSP .....</b>	<b>8</b>
<b>1.2 Central Receiver System (CRS) .....</b>	<b>9</b>
<b>1.2.1 Next Generation CSP .....</b>	<b>10</b>
<b>1.3 Passive Heat Transfer Enhancement .....</b>	<b>11</b>
<b>1.4 Objectives of This Work .....</b>	<b>11</b>
<b>1.5 Scope of This Work .....</b>	<b>12</b>
<b>CHAPTER 2: LITERATURE REVIEW .....</b>	<b>13</b>
<b>2.1 Central Receiver System (CRS) .....</b>	<b>13</b>
<b>2.2 Receiver Efficiency .....</b>	<b>14</b>
<b>2.2.1 Gas Receivers .....</b>	<b>15</b>
<b>2.2.2 Solid Particle Receivers .....</b>	<b>15</b>
<b>2.2.3 Liquid Receivers .....</b>	<b>15</b>
<b>2.2.4 Cavity Receiver .....</b>	<b>16</b>
<b>2.2.5 External Tubes Receiver .....</b>	<b>16</b>
<b>2.3 Passive Heat Transfer Enhancement .....</b>	<b>17</b>
<b>2.4 Corrugated Tubes .....</b>	<b>18</b>
<b>2.4.1 Multi-start Spirally Corrugated Tubes .....</b>	<b>18</b>
<b>2.4.2 Other Corrugated Tubes .....</b>	<b>20</b>
<b>2.5 Tube Selected for Study .....</b>	<b>22</b>
<b>2.5.1 Spirally Corrugated Tube 1 .....</b>	<b>22</b>
<b>2.5.2 Spirally Corrugated Tube 2 .....</b>	<b>23</b>
<b>2.5.3 W-Type Spirally Fluted Tube .....</b>	<b>24</b>
<b>2.5.4 Spirally Grooved Tube .....</b>	<b>25</b>
<b>2.5.5 Reuleaux Triangle Cross Section Tube .....</b>	<b>26</b>
<b>2.6 Conclusion .....</b>	<b>27</b>
<b>CHAPTER 3: COMPUTATIONAL FLUID DYNAMICS .....</b>	<b>28</b>
<b>3.1 ANSYS Fluent .....</b>	<b>28</b>
<b>3.2 Background .....</b>	<b>28</b>
<b>3.2.1 Navier-Stokes Equations .....</b>	<b>29</b>
<b>3.3 Turbulent Flow .....</b>	<b>30</b>
<b>3.4 Turbulence Modelling in Fluent .....</b>	<b>30</b>
<b>3.4.1 One Equation Models .....</b>	<b>31</b>

3.4.2 Two Equation Models .....	31
3.4.2.1 The standard K-E (SKE) model .....	31
3.5 Methodology .....	31
3.5.1 The Geometry .....	32
3.5.1.1 Circular Tube .....	33
3.5.1.2 SC-1 Tube .....	34
3.5.1.3 SC-2 Tube .....	35
3.5.1.4 WTC Tube .....	37
3.5.1.5 SG Tube .....	38
3.5.1.6 Rolo Tube .....	39
3.5.2 The Mesh .....	40
3.5.2.1 Circular Tube .....	40
3.5.2.2 SC-1 Tube .....	42
3.5.2.3 SC-2 Tube .....	44
3.5.2.4 WTC Tube .....	46
3.5.2.5 SG Tube .....	48
3.5.2.6 Rolo Tube .....	50
3.5.3 The Setup .....	52
3.5.3.1 The boundary conditions .....	54
<b>CHAPTER 4: EXPERIMENTAL STEUP .....</b>	<b>57</b>
<b>4.1 Design of Experiment .....</b>	<b>57</b>
4.1.1 Refrigerated Circulator .....	58
4.1.2 Flow Control Valve .....	60
4.1.3 Flow Meter .....	60
4.1.4 Universal DC Input Meter .....	61
4.1.5 Thermocouples .....	62
4.1.5.1 Leak Prevention .....	64
4.1.6 Data Acquisition .....	64
4.1.7 Solar Irradiance Simulator .....	65
<b>4.2 Fabrication of Tubes .....</b>	<b>67</b>
4.2.1 Direct Metal Laser Sintering (DMLS) .....	67
4.2.2 Working of DMLS .....	68
4.2.3 Saftey precautions with DMLS .....	70
<b>4.3 The Test Samples .....</b>	<b>71</b>
<b>4.4 Connections and Reducers .....</b>	<b>72</b>
<b>4.5 The Test Rig .....</b>	<b>73</b>
4.5.1 Support for The Rig .....	75
<b>4.6 Calibration .....</b>	<b>76</b>
4.6.1 Thermocouples Calibration .....	76
4.6.2 Flow Meter Calibration .....	77
<b>CHAPTER 5: RESULTS &amp; DISCUSSION .....</b>	<b>79</b>
<b>5.1 CFD Results .....</b>	<b>79</b>
5.1.1 Circular Tube .....	79
5.1.2 SC-2 Tubes .....	82

<b>5.1.3 WTC Tube</b> .....	<b>85</b>
<b>5.1.4 SG Tube</b> .....	<b>86</b>
<b>5.1.5 Rolo Tube</b> .....	<b>89</b>
<b>5.1.6 Validation</b> .....	<b>92</b>
<b>5.2 Experimental Results</b> .....	<b>93</b>
<b>5.2.1 Inlet</b> .....	<b>93</b>
<b>5.2.2 Station 1</b> .....	<b>94</b>
<b>5.2.3 Station 2</b> .....	<b>96</b>
<b>5.2.4 Station 3</b> .....	<b>98</b>
<b>5.2.5 Station 4</b> .....	<b>100</b>
<b>5.2.6 Outlet</b> .....	<b>102</b>
<b>5.2.7 Heat Transfer in Tubes</b> .....	<b>104</b>
<b>5.2.8 Pressure Drop in Tubes</b> .....	<b>107</b>
<b>CHAPTER 6: CONCLUSION &amp; RECOMMENDATIONS</b> .....	<b>109</b>
<b>REFERENCES</b> .....	<b>112</b>



## LIST OF TABLES

Table 1: Dimensions of Circular Tube.....	33
Table 2: Dimensions of SC-1 Tube.....	34
Table 3: Dimensions of SC-2 Tube.....	35
Table 4: Dimensions of WTC Tube.....	37
Table 5: Dimensions of SG Tube.....	38
Table 6: Dimensions of Rolo Tube.....	39
Table 7: Mesh specifications of Circular Tube.....	41
Table 8: Mesh specifications of SC-1 Tube.....	43
Table 9: Mesh specifications of SC-2 Tube.....	45
Table 10: Mesh specifications of WTC Tube.....	47
Table 11: Mesh specifications of SG Tube.....	49
Table 12: Mesh specifications of Rolo Tube.....	51
Table 13: Material properties for fluid & solid domains.....	53
Table 14: Solution methods.....	54
Table 15: Inlet velocity magnitudes in m/s.....	56

## LIST OF FIGURES

Figure 1: Share of global demand met by renewables in selected sectors in the New Policies Scenario and 450 Scenario [5].....	3
Figure 2: Global solar irradiation [11]. .....	4
Figure 3: Electricity generation from 2000 to 2050 in MENA & South-European countries [15]. .....	6
Figure 4: Schematic of a CSP plant [16].....	7
Figure 5: Types of CSP; (a) Parabolic Trough, (b) Solar Tower, (c) Fresnel Reflectors, (d) Dish Collector. ....	8
Figure 6: Projected cost of CSP solar tower [19].....	9
Figure 7: A typical central receiver [22]. .....	10
Figure 8: Six-start spirally corrugated tube [70]. .....	19
Figure 9: Spirally corrugated tube by Zimparov et al. [115]. .....	23
Figure 10: Spirally corrugated tube by Lee et al. [118]. .....	24
Figure 11: W-type spirally fluted tube by Cui et al. [63]. .....	25
Figure 12: Spirally Grooved Tube by Jianfeng et al. [141]. .....	26
Figure 13: Cross sectional sketch of reuleaux triangle. ....	27
Figure 14: SolidWorks model of Circular Tube.....	34
Figure 15: SolidWorks model of SC-1 Tube. ....	35
Figure 16: SolidWorks model of SC-2 Tube. ....	36
Figure 17: SolidWorks model of WTC Tube.....	37
Figure 18: SolidWorks model of SG Tube.....	38

Figure 19: SolidWorks model of Rolo Tube.....	39
Figure 20: CFD mesh of Circular Tube. ....	41
Figure 21: CFD mesh of Circular Tube wall.....	41
Figure 22: Grid Independence of Circular Tube. ....	42
Figure 23: CFD mesh of SC-1 Tube. ....	43
Figure 24: CFD mesh of SC-1 Tube wall. ....	44
Figure 25: CFD mesh of SC-2 Tube. ....	45
Figure 26: CFD mesh of SC-2 Tube wall. ....	46
Figure 27: CFD mesh of WTC Tube.....	47
Figure 28: CFD mesh of WTC Tube wall.....	48
Figure 29: CFD mesh of SG Tube. ....	49
Figure 30: CFD mesh of SG Tube wall.....	50
Figure 31: CFD mesh of Rolo Tube.....	51
Figure 32: CFD mesh of Rolo Tube wall.....	52
Figure 33: UDF example for Inlet boundary condition.....	55
Figure 34: Schematic of the closed loop flow.....	58
Figure 35: Julabo FP50 Chiller. ....	59
Figure 36: HDPE shut-off valve.....	60
Figure 37: High precision turbine wheel flow meter. ....	61
Figure 38: Universal DC input meter.....	62
Figure 39: Fluke 80PK-1; bead probe K-Type thermocouple.....	63
Figure 40: Thermocouples installed in tubes. ....	63

Figure 41: Fluke data acquisition system. ....	65
Figure 42: (a) Solar Irradiance Simulator sketch; (b) Top view; (c) Actual photo; (d) Inside box. ....	66
Figure 43: DMLS machine. ....	68
Figure 44: DMLS technique. ....	69
Figure 45: Manufactured tubes; (a) Circular, (b) SC-1, (c) SC-2, (d) WTC, (e) SG, (f) Rolo. ....	71
Figure 46: Reducers and connections for tubes. ....	73
Figure 47: The test rig. ....	74
Figure 48: The rig installed with its support. ....	75
Figure 49: Thermocouples error curves (Temp vs error). ....	77
Figure 50: Flow meter calibration curve. ....	78
Figure 51: Temperature contour of flow in Circular Tube. ....	80
Figure 52: Radial Velocity contour of flow in Circular Tube. ....	81
Figure 53: Turbulent Kinetic Energy contour of flow in Circular Tube. ....	81
Figure 54: Turbulent Intensity contour of flow in Circular Tube. ....	82
Figure 55: Temperature contour of flow in SC-2 Tube. ....	83
Figure 56: Radial Velocity contour of flow in SC-2 Tube. ....	84
Figure 57: Turbulent Intensity contour of flow in SC-2 Tube. ....	85
Figure 58: Radial Velocity contour of flow in WTC Tube. ....	86
Figure 59: Temperature contour of flow in SG Tube. ....	87
Figure 60: Radial Velocity contour of flow in SG-Tube. ....	88

Figure 61: Turbulent Kinetic Energy contour of flow in SG-Tube.....	88
Figure 62: Turbulent Intensity contour of flow in SG Tube. ....	89
Figure 63: Temperature contour of flow in Rolo Tube.....	90
Figure 64: Turbulent Kinetic Energy contour of flow in Rolo Tube. ....	91
Figure 65: Turbulent Intensity contour of flow in Rolo Tube.....	92
Figure 66: Nusselt Number predicted by CFD vs Dittus Boelter equation.....	93
Figure 67: Temperature vs flow rate plot at Inlet of all tubes.....	94
Figure 68: Temperature vs flow rate plot at station 1 of all tubes. ....	96
Figure 69: Temperature vs flow rate plot at station 2 of all tubes ....	98
Figure 70: Temperature vs flow rate plot at station 3 of all tubes. ....	100
Figure 71: Figure 4: Temperature vs flow rate plot at station 4 of all tubes. ....	102
Figure 72: Temperature vs flow rate plot at outlet of all tubes.....	104
Figure 73: Heat transfer vs. flow rate plot for all tubes. ....	105
Figure 74: Pressure drop comparison of all tubes. ....	107

## CHAPTER 1: INTRODUCTION

From everyday commute to lighting homes at night, nearly everything humans do require energy. Energy has become the backbone of existence and modern civilization. Human beings have made use of energy in different ways for thousands of years, mostly by burning fuels. Fossil fuels such as coal and oil are among the most energy rich resources found on earth. Coal became a primary source of energy since the first industrial revolution in the 17<sup>th</sup> century whereas Oil and electricity became driving forces of the second industrial revolution in 19<sup>th</sup> century. The transport industry is heavily dependent on oil due to its high energy density, ease of storage, and ease of transport [1].

Although very efficient, fossil fuels have two major drawbacks. Firstly, these fuels are expected to deplete over time with the growth of industry and human population. Secondly, these fuels produce CO<sub>2</sub> on combustion and contaminates the atmosphere. Excessive CO<sub>2</sub> in the atmosphere is a major threat to environment because it can cause climate change across the globe. This results in global warming which is proven to have catastrophic impact on environment and thus considered a major threat [2][3]. Majority of current global CO<sub>2</sub> emissions are a result of burning fossil fuels for power generation and transport sector [4].

Renewable and clean sources of energy as substitute to fossil fuels have been heavily pursued since 19<sup>th</sup> century. As of 2014, only 23% of electricity, 9% of heating, and 3% of transport demand was met by renewables. The current world demand for energy is expected to grow to a considerable amount. It is estimated that approximately 37% to 58% of world electricity

will be derived from renewable sources by 2040 (Figure 1) [5]. However, even after policies that promote renewables are put in place, the global temperature is expected to rise by 2°C till 2035. Diligent efforts in development of renewable energy technologies is required. A prime rationale behind the use of fossil fuels is its economic price [6]. This calls for efforts in making renewable energy systems cost competitive [7]. Substantial research attention and efforts has focused on making renewable energy systems cost competitive. One such example is that of Concentrated Solar Power (CSP) plant, which is expected to compete fossil fuels by 2020. 15% of the cost of CSP technology corresponds to its central receiver, where the heat transfer takes place [8]. Improved heat transfer corresponds to higher operating temperature, which in turn corresponds to higher efficiency, thus lower cost [9]. These facts form the motivation behind this work to focus on passive heat transfer enhancement of the receiver tubes by using various corrugated tubes.

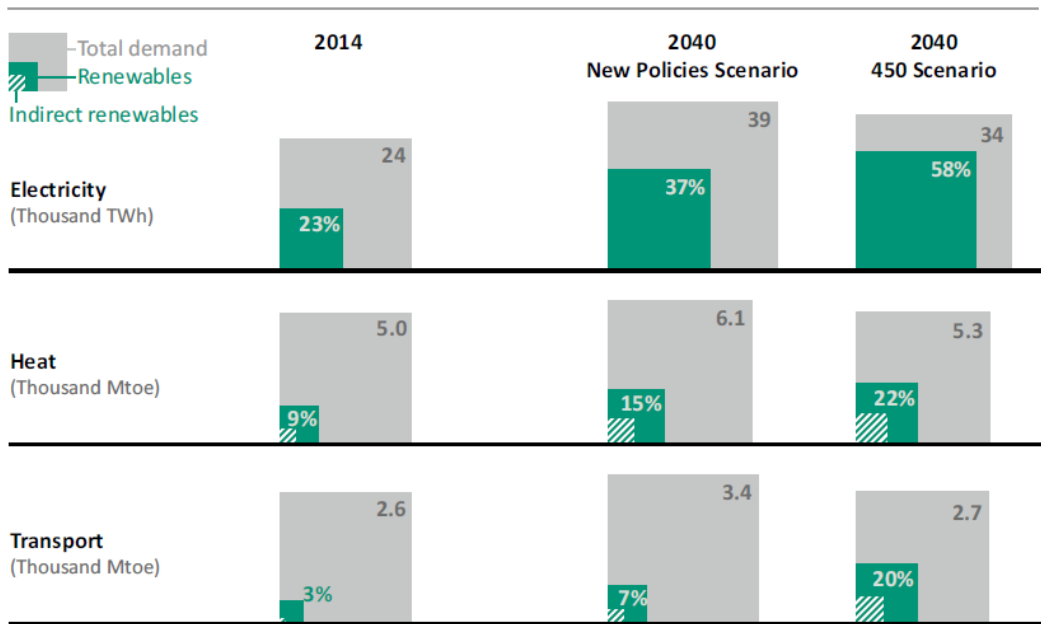


Figure 1: Share of global demand met by renewables in selected sectors in the New Policies Scenario and 450 Scenario [5].

### 1.1. Renewable Energy

The need for renewable sources of energy was realized as early as the 1870s. Various affordable renewable energy technologies are available today after decades of research and development since the 19<sup>th</sup> century [10]. 22.8% of global electricity production came from renewable sources in 2014, making it the third largest source of electricity [5]. Examples of some of the mainstream commercially viable sources include hydropower, wind power, geothermal energy, solar power, and biomass.



### 1.1.1. Solar Power

Solar is the most abundant source of energy [11]. In the early stages of renewables, a lot of attention was given to energy from the sun [12]. Energy from sun is received on earth as light and heat energy. The earth receives 174 petawatts of solar radiation at the upper atmosphere. Much of this radiation is absorbed by landmasses, clouds, and oceans while 30% is reflected to space [13]. Most of the world's population lives in areas with irradiation levels of 150 to 300 W/m<sup>2</sup> (Figure 2). There are two main types of solar energy. The light energy is harvested using technology called Photovoltaics (PV). While the heat energy is harvested by concentrating solar heat on one point where it can be collected. The basic difference lies in the wavelength of radiation being harvested.

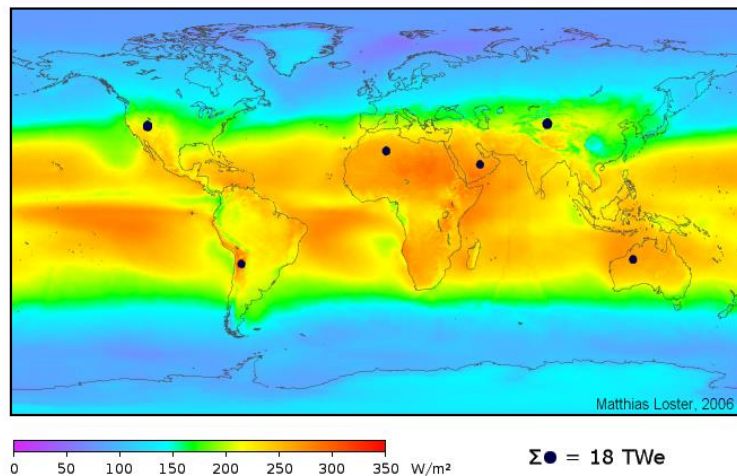


Figure 2: Global solar irradiation [11].

#### **1.1.1.1. Solar PV**

PV technology involves the use of semiconductors that convert light energy to electrical energy. Solar PV is a clean energy source and can be readily harvested almost anywhere. It has some major drawbacks that has hindered its growth. Solar PV generally has a very low efficiency and is expensive to manufacture. It also requires batteries as storage technology, which increases the cost substantially. The efficiency of PV is also dependant on climate and clarity of the atmosphere on site. Hence this technology is not suitable for hot and dusty regions [12]. Current business and research trends indicate more efficient and cheaper solar panels soon, but it is not an ideal solution for hot climates like Qatar. These systems are also best suited for small scale applications like homes.

#### **1.1.1.2. Concentrated Solar Power (CSP)**

This technology concentrates a large area of solar irradiance onto a small area. Large mirrors or lens are used to collect the heat to one point. This heat is further used to drive heat engine to produce electricity, heat water, or perform a thermochemical reaction [12]. CSP is considered a technology that will play an important role in the future of energy and it has recently gained increased interest worldwide due to its rising economic competitiveness with fossil fuels [14]. This technology is recently commercialized and a generating capacity of more than 800 MW has been installed in the past decade. It is expected that countries in Africa, Middle East, and Oceania may see half of their electricity produced from CSP plants by 2050 (Figure 3) [15].

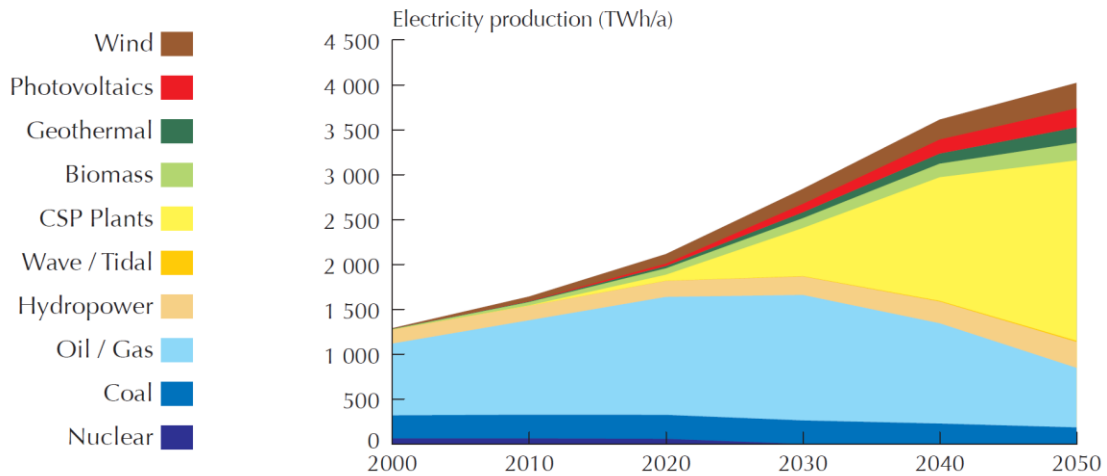


*Figure 3: Electricity generation from 2000 to 2050 in MENA & South-European countries [15].*

CSP is composed of large mirrors or lens positioned in a way that it concentrates sunlight to a single receiver. The solar receiver consists of one or more tubes in which the heat transfer fluid flows. The heat transfer fluid used varies depending on the type of CSP system and its end use. In case of molten salts, the system also has thermal storage tanks to store the captured heat. The fluid is then used to drive an engine to generate electricity, either directly using water or indirectly using molten salt, where it goes through heat exchanger to produce steam that will run a Rankine cycle (Figure 4) [12].

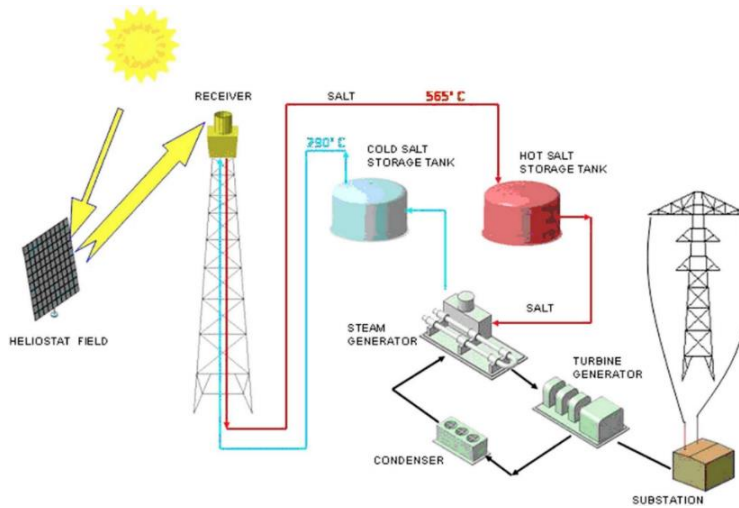
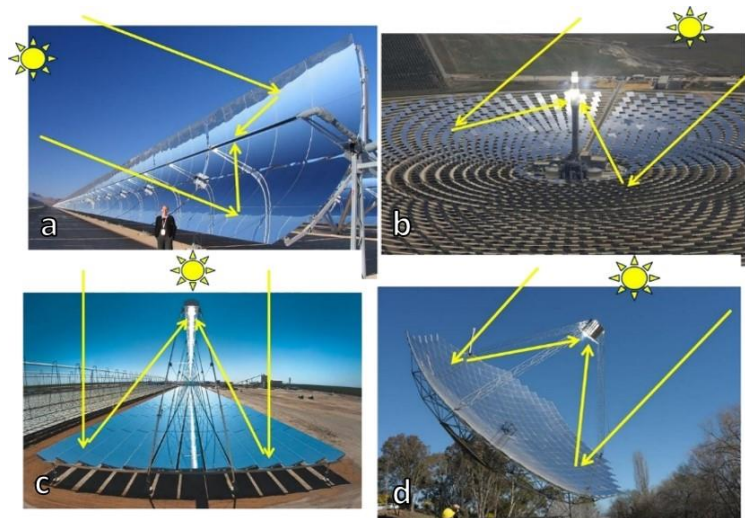


Figure 4: Schematic of a CSP plant [16].

CSP has an advantage over PV in terms of efficiency and better storage technology. Heat transfer fluid retaining the heat can be stored in insulated tanks. Phase Changing Material (PCM) can be sometimes used for longer duration storage. This technology is more efficient and cheaper than battery technology [12] [17]. CSP is an ideal solution for hot regions and can be used in large scale for electricity generation. It can be easily integrated in fossil plant for hybrid operation. Although this technology cannot be used for electricity generation in small scale like homes, it can be used for domestic water heating.

### 1.1.1.2.1. Types of CSP

There are some types of CSP including parabolic trough, Fresnel reflectors, dish collectors, and solar tower (Figure 5). They work on same principle but the difference lies in their construction and application.



*Figure 5: Types of CSP; (a) Parabolic Trough, (b) Solar Tower, (c) Fresnel Reflectors, (d) Dish Collector.*

## 1.2. Central Receiver System (CRS)

Among all CSP technologies, CRSs are the best choice for large scale application. CRS, also known as Solar Tower, consists of an array of reflectors that concentrate sunlight on central receiver located on a tower [9] [14]. The receiver contains fluid flow that transports the heat energy to heat engine. This is a less developed technology, but has better efficiency and storage capabilities. Solar tower is expected to reach lower levelized cost of electricity compared to other CSP technologies (Figure 6) [18].

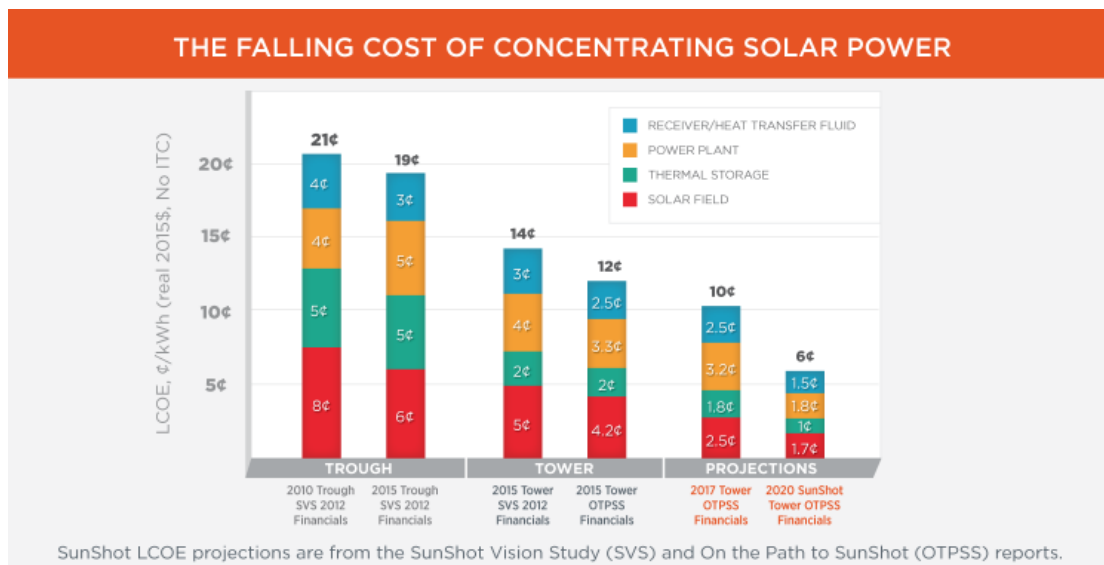


Figure 6: Projected cost of CSP solar tower [19].

### 1.2.1. Next Generation CSP

To increase efficiency, thus lower the costs, next generation CSP systems will need to scale up to higher fluxes [20]. Next generation CSP are expected to reach a price of 6 cents/kwh. The central receiver is a key component of CSP and forms 15% of the total CSP cost [8]. Improving performance of the receiver will improve efficiency of a CSP system. This is done either by increasing the operating temperature of the Heat Transfer Fluid (HTF) or improving the receiver design [21]. Molten salts are used as HTF currently, which has operating temperature of around 650°C. The next generation CSPs will have HTF with operating temperature of 900°C, which is the optimum for highest efficiency [12], [19]. A typical central receiver consists of panels containing tubes. The tubes are cooled by HTF from inside and heated from solar radiation from outside. The HTF has serpentine flow pattern in the tubes for more exposure to radiation heat (Figure 7).

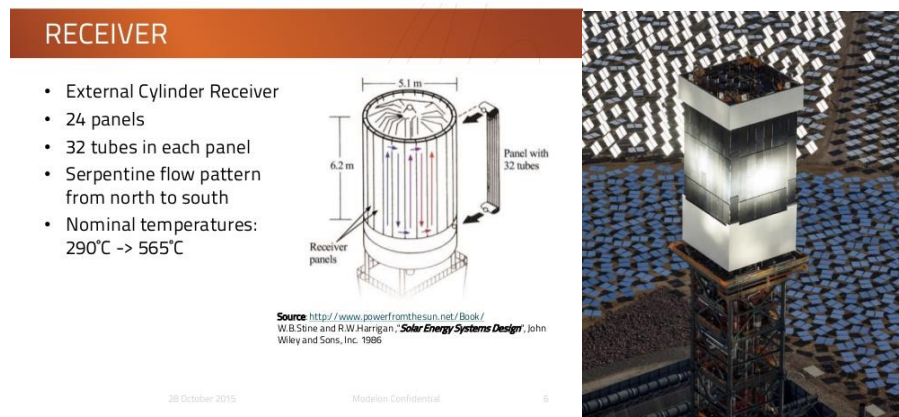


Figure 7: A typical central receiver [22].

### **1.3. Passive Heat Transfer Enhancement**

Heat transfer is crucial to many engineering applications, especially in energy production via systems like CSP. Extensive research goes into enhancing heat transfer in various systems. Active heat transfer constitutes the use of external energy to boost the heat transfer. Whereas passive heat transfer requires changes to system that will naturally promote heat transfer, such as surface modification. A common approach to passive heat transfer enhancement in fluid flow in tubes is changing the cross-sectional geometry. Tube corrugation is the most common way of enhancing heat transfer in tube flows [23]. Traditional CRS are composed of circular tubes in the central receiver [24], whereas corrugation may provide more surface area for heat transfer and promotes turbulence in internal flows. This way the heat can be efficiently transferred via conduction, convection, and advection.

### **1.4. Objectives of This Work**

This work uses passive heat transfer techniques to enhance heat transfer to receiver tubes. The author proposes a new tube design for central receiver of CRS and proposes the use of corrugated tubes. Therefore, the objectives are listed as,

- To assess the heat transfer performance of the proposed tube design in comparison to circular tube. The proposed tube has more surface area exposed to radiation as compared to circular tube.
- To investigate the heat transfer performance of corrugated tubes in comparison to circular tube and investigate their usefulness in central receiver of the CRS.



## **1.5. Scope of This Work**

The novel tube proposed in this work is hypothesized to provide better heat transfer than circular tube. This is because this design provides more surface area exposed to the sun when installed in similar fashion to the circular one, while having similar amount of tube material. This work can provide a better understanding of effects of passive heat transfer enhancement on central receiver. This work also investigates the use of corrugated tubes for receiver, which may provide a direction for future work in receiver tubes. Currently there has been very little work in use of corrugated tubes for radiation heat transfer, which shall be summarized in chapter 2. This work will provide a comprehensive literature review of central receiver tube technologies and the attempts at improving their efficiencies. Different tube geometries will also be discussed. All possible tube choices for central receiver shall be reported. Four tubes with most heat transfer and least pressure drop that can be easily acquired shall be chosen. The selected tubes shall be manufactured, experimented, and compared to circular and the proposed tube. The experiment consists of solar radiation simulator and distilled water flow loop for the samples. Computational Fluid Dynamics (CFD) simulation shall also be carried on each tube and the results from experiment will be compared. The pressure data and the turbulence inside the tubes will be investigated in CFD simulation results. A conclusion based on the experiment and CFD simulation will be drawn. The limitations of this work and future recommendations will be discussed.

## CHAPTER 2: LITERATURE REVIEW

### 2.1 Central Receiver System (CRS)

Earliest plants of CRS were built in the 1980s while the first demonstration facilities were built in the 1990s [20]. Tests on receivers with liquid sodium as heat transfer fluid were also carried in the 80s [25]. The conclusion from these tests were very positive in terms of thermal efficiency, but the experiments stopped due to fire accident caused by sodium leakage. This lead to a reduced interest in the area for a long period until very recently sodium cooled receivers were tested successfully [26]. CRS has very recently entered the stage of commercialization. 13% of operational CSP capacity in 2016 was formed by CRS and it is expected to soon become one of the best choices compared to other CSP technologies [9], [14], [19], [27], [28]. Some of the credit goes to the fact that solar tower enables far greater solar concentrations than other CSP technologies, hence they also have higher overall efficiencies. It is also easier to employ thermal storage in this technology as compared to others [29].

Many CRS plants are planned recently in USA, Spain, and China. The capacities of these plants range from 20MW to 2000MW. Numerous R&D projects for CRS are announced recently in USA, Spain, Cyprus, Italy, France, Portugal, Turkey, Greece, Israel, Algeria, and Germany. The budget for these projects range from approximately 3 million USD to 8 million USD [21]. There is a great potential to reduce production costs and improve energy efficiency, which has constantly been pursued by process industries [30]–[32]. Several recent

R&D activities such as ECOSTAR, SunShot CSP Program USA, Australian Solar Thermal Research Initiative (ASTRI), DLR, and CIEMAT are aiming to make CRS technology cost competitive. Significant cost reductions can be achieved by scaling up and mass production, increasing energy conversion efficiency, and improving receiver efficiency [21], [26]. Receiver efficiency, fluid and tube wall temperatures, and dynamic behaviour of the system are the most important parameters of CSP [33].

## **2.2 Receiver Efficiency**

Heat flux density as high as 2.5 MW/m<sup>2</sup> are irradiated on receiver tubes in a CRS [34]. Receiver acts as collecting system where the high fluxes are directly incident on tubes that contain heat transfer fluid [33], [35]. 15% of the initial investment cost of CRS is attributed to the receiver [8]. Receiver is a very crucial component of CRS and developing more efficient receiver will lead to more efficient acquisition of solar thermal energy [33], [35]. High efficiency leads to lower costs, which is achieved by increasing heat flux and consequently the operating temperature of the receiver [19], [27]. Typical commercial CRS operate at temperatures below 600°C, whereas the next generation CRS are expected to reach higher heat flux and higher temperatures [9], [29]. The optimum temperature for maximum thermal efficiency is found to be around 900°C [36], [37]. Geometric design of the receiver, material of the receiver, heat transfer fluid, processes to maximise solar irradiance, processes to maximize radiation absorption, processes to minimize heat loss, and reliability are the

primary challenges of high temperature receivers. High temperature receivers, are divided into three categories namely, gas receivers, liquid receivers, and solid particle receivers [38].

### **2.2.1 Gas Receivers**

A considerable amount of work in design, experiment, and enhancement has been done in development of volumetric air receivers, and tubular gas receivers. Volumetric air receivers consist of metal or ceramic porous wires which absorb the direct solar irradiation. Air passing through these wires absorb the heat and transfers it to heat exchanger [21], [38].

### **2.2.2 Solid Particle Receivers**

This kind of receiver uses solid particles as heat transfer medium that absorbs the direct solar irradiance. These systems are not well developed as compared to other receiver types. There is very little design, experiment, and enhancement work already performed in this area [21].

### **2.2.3 Liquid Receivers**

Liquid receivers are mainly of three types cavity, external tubes, or falling film type. Falling film type receivers constitute the flow of molten salt on the outer periphery of the receiver, keeping the fluid directly exposed to the radiation. Whereas the cavity and external types constitute the flow of heat transfer fluid inside tubes [38].

#### **2.2.4 Cavity Receiver**

The radiation from heliostats pass through an aperture into a box-like structure and then to the tubes surface. Considerable amount of work has been done in development of these type of receivers. Cavity receivers have less radiative and convective heat losses compared to external receiver but require taller towers. Much of the work focuses on the design of the whole box while some work focuses on design of the tubes [21].

Experiments were performed by Wu et al. [39] to examine the heat transfer characteristics of molten salt in a circular tube. After a 3-D numerical study, Wu et al. proposed a more accurate correlation of Nusselt number that can estimate natural convection heat losses in cavity receivers [40]. Use of helically coiled tubes have as heat absorbers in cavity receivers has been heavily investigated in the past decade [35], [41]–[50]. Some variations like Neber and Lee's [51] helically coiled square duct and Le Roux et al.'s [52] rectangular cavity shaped coiled tube have also been presented. Uhlig et al. [53] showed that the use of corrugated tubes increased the receiver efficiency from 71.9% to 83.5%.

#### **2.2.5 External Tubes Receiver**

External tubes receiver consists of panels of tubes arranged in a cylindrical or cubical configuration. The tubes are half exposed to solar irradiation and cooled by heat transfer fluid from the inside. Much of the work in this receiver focuses on the heat transfer outside the receiver surface while little work focuses on convective heat transfer inside the tube [29].

Lu et al. [54], Rabas et al. [55], and Ravigururajan et al. [56] investigated the spirally grooved pipe for heat transfer enhancement in molten salt receiver. Barba et al. [57] performed numerical analysis of spirally fluted tube. Akgun and Parlar [58] studied spiral tubing in flat plate solar collector. Yang et al. [59] tested solar receiver formed by spiral tubes and Garbrecht et al. [60] proposed a design composed of hexagonal pyramid shaped elements instead of circular pipes. Rodriguez-Sanchez et al. [24] proposed a bayonet receiver design and found that the thermal efficiency increases by 2%.

### **2.3 Passive Heat Transfer Enhancement**

Heat exchangers play an important role in many industrial applications like membrane dehumidification, nuclear reactor, solar water heater, and energy storage [61]. Active heat transfer includes enhancing heat transfer using external source while passive heat transfer is the enhancement via modification to surfaces [62]. Passive heat transfer is considered to have wider application due to its inexpensive cost in maintenance, reliability in operation, and low energy input [61]. Surface modification constitutes artificially roughened surfaces, extended surfaces, addition of twisted tapes, inserted coils, and corrugation [63], [64]. These methods induce swirl and vortices at the secondary flow region, hence better mixing of the fluid. Corrugated tubes have been widely used in various applications to enhance heat transfer by enhancing the secondary re-circulation flow [65]–[69]. Heat transfer enhancement in CSP can be done by increasing the heat transfer coefficient which is done by increasing fluid

mixing via roughened or finned inner surfaces. Such modifications also increase pressure loss, which must be an important design constraint and must not be neglected [31].

## **2.4 Corrugated Tubes**

There are many ways corrugation of tubes is achieved. Some literature in heat transfer in corrugated tubes will be discussed in this section.

### **2.4.1 Multi-start spirally corrugated tubes**

Research in corrugation has recently evolved from single start spirally corrugated to multi-start spirally corrugated tubes (Figure 8). There is substantial amount of literature on heat transfer of single start spirally corrugated tubes [70]. A numerical study on flow and heat transfer characteristics of single start spirally corrugated tube was conducted by Li et al. [71] Whereas Rainieri et al. [72] investigated high viscosity fluid in spirally corrugated tube and its heat transfer performance. Another numerical study on flow corrugations and heat transfer characteristics of turbulent flow in single start spirally corrugated tube was conducted by Promthaisong et al [73] whereas Pal and Saha [74] studied the laminar flow of viscous oil. Experimental and numerical simulation on helical baffled cooler with spirally corrugated tube was conducted by Liu et al [75]. Li et al. [71] conducted numerical investigation in turbulence and temperature in helical tubes with spiral corrugation. Seara and Francisco [76] experimentally evaluated the heat transfer and frictional characteristics of spirally corrugated

tubes. Kalendar et al. [77] investigated the anti-fouling property of single start spirally corrugated tube. Bhattacharyya and Saha [78] and Saha [69] investigated hydraulic performance of laminar flow through tube with integral corrugation and with inserted twisted tape and inserted helical screw-tape. All these studies show that corrugation has better heat transfer performance than smooth tube but increases pressure loss. This however, became the basis for further study in multi-start corrugated tube.

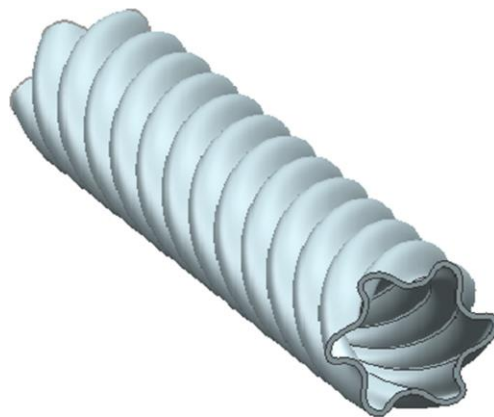


*Figure 8: Six-start spirally corrugated tube [70].*

Kareem et al. [79] conducted a study on two start spirally corrugated tube and then performed experiment on three start spirally corrugated tube [80]. Zimparov [81] experimentally investigated the heat transfer performance and pressure drop of three start spirally corrugated



tube. Eiamsa et al. [82] conducted a study on three start spirally corrugated tube. Lazim et al. [83] compared the heat transfer performance of four start spirally corrugated tube with smooth tube. Chen et al. [84] investigated the heat transfer performance of four start spirally corrugated tube and effect of corrugation angles on hydrodynamic performance. Ahn [85] conducted an experimental study on the heat transfer performance of four start spirally corrugated tube. Liu et al. [86] conducted numerical study on single start, two-start, three-start, and four-start spirally corrugated tubes. Jin et al. [70] proposed and investigated six-start spirally corrugated tube and its heat transfer performance. Balla [62] Numerically evaluated six-start spirally corrugated tube for its heat transfer performance and friction factor. The multi-start spirally corrugated tubes provide better heat transfer than single start spirally corrugated tube and has higher pressure loss.

#### **2.4.2 Other Corrugated Tubes**

Spirally fluted tubes have been found to be an attractive way of heat transfer enhancement [87]–[89]. Cui et al. [63] experimentally investigated the heat transfer performance and pressure drop in W-type spirally fluted tubes. The results showed heat transfer coefficients enhancement of up to 160% while the friction factor increased up to 300%, compared to a smooth tube. Other corrugated tubes investigated include, converging diverging tube [90], [91], transverse corrugated tubes [68], [92], internally grooved tubes [93], outward helically corrugated tubes [94], outward convex traverse [65], dimpled tube [95], helically dimpled tubes [96], [97], coiled corrugated tubes [72], helically finned tube [98], [99], twisted tri-

lobed tube [100], twisted elliptical tubes [101], [102], and discrete inclined rib tubes [103], [104]. Corrugated passages are proven to have better heat transfer performance than that of plain passages. Hence this type has also got substantial attention recently [105], [106].

Literature is laden with experimental study on corrugated tubes. Laminar flow in different corrugation methods were investigated by Rainieri et al. [107], Kang et al. [108], Raineiri and Pagliarini [109], Barba et al. [110], Raineiri and Pagliarini [68], Saha [111], Rainieri et al. [72], Saha et al. [112], Saha [69], Rainieri et al. [113], Pal and Saha [74]. Whereas turbulent flow in different corrugation methods were investigated by Vulchanov et al. [114], Zimparov et al. [115], Nozu et al. [116], Macbain et al. [117], Lee et al. [118], Salim et al. [119], Wang et al. [120], Wu et al. [121], Chen et al. [84], Dong et al. [122], Qi et al. [123], Zimparov [124], Zimparov [81], Ahn [85], Cui et al. [63], Inagaki and Ozawa [125], Vicente et al. [126], Vicente et al. [127], Targanski and Cieslinski [128], Laohalertdecha and Wongwises [129], Saha [130], Aroonrat and Wongwises [131], Laohalertdecha et al. [132], Laohalertdecha and Wongwises [133], Laohalertdecha and Wonwises [134], Pethkool et al. [135], Darzi et al. [136], Fernandez-Seara and Uhia [76], khoeini et al. [137], Wongcharee and Eiamsa-ard [138], Aroonrat et al. [139], Chen et al. [140], Jianfeng et al. [141], Liu et al. [75], Poredos et al. [142], Akhavan-Behabadi and Esmailpour [143], Balcilar et al., Balcilar et al. [144], Darzi et al. [145], Kathiat and Patil [146], and Laohalertdecha et al [147].

## **2.5 Tubes Selected for Study**

In this work, six different corrugated tubes are selected from the tubes used for turbulent flow in literature. The choice of these tubes is based on highest heat transfer to lowest pressure drop. The heat transfer performance of these tubes is compared to a circular tube and a new geometry tube. The total number of tubes to be compared with circular tube and the new design are four. These tubes are listed as follows.

### **2.5.1 Spirally Corrugated Tube 1**

Zimparov et al. [115] investigated heat transfer and friction characteristics of spirally corrugated tubes for power plant condensers (Figure 9). The experiment was performed on 25 spirally corrugated tubes of varying geometries and a standard circular tube. The 800mm corrugated section in test section of the rig had 9 thermocouples at 100mm intervals for temperature measurement. A U-manometer connected to inlet and outlet was used for measurement of pressure loss reading. The heat was supplied to test section via steam generated in a boiler. The results showed a maximum enhancement of 273% whereas the maximum friction factor coefficient was 400% in comparison to the smooth tube. Measurement specifications of the best tube was acquired from this study and the tube was then scaled down to required surface area for comparison with other tubes. This type of tube will be referred to as ‘SC-1 Tube’ further in this report.

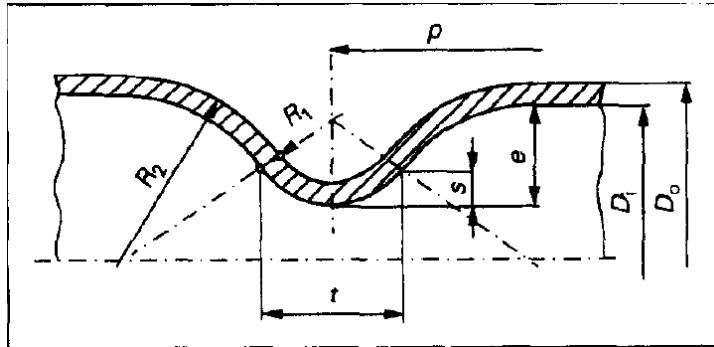


Figure 9: Spirally corrugated tube by Zimparov et al. [115].

### 2.5.2 Spirally Corrugated Tube 2

Lee et al. [118] conducted a performance heat transfer and pressure drop experiment on a spirally indented tube for Liquefied Natural Gas cold energy utilization (Figure 10). Ethylene-glycol water was used as working fluid to heat water inside a 5.38m test tube. Pressure was measured at inlet and outlet using pressure transducers whereas temperatures at inlet and outlet were measured for both cooling and heating mediums. The tests were run for Reynolds number 500 to 5000 for ethylene and 4000 to 25000 for water. The results showed that the heat transfer enhancement was greater than the increasing friction factor while the heat transfer coefficient was 8 times higher than that of plain tube. This type of tube will be referred to as 'SC-2 Tube' further in this report.

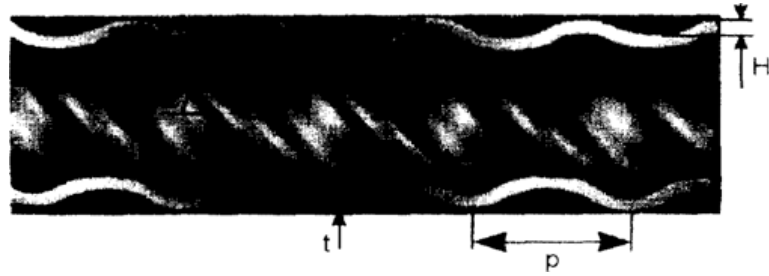


Figure 10: Spirally corrugated tube by Lee et al. [118].

### 2.5.3 W-Type Spirally Fluted Tube

Cui et al. [63] investigated heat transfer and pressure drop characteristics of W-Type spirally fluted tubes (Figure 11). Six w-type spirally fluted copper tubes and a standard smooth copper tube were studied. Electric boiler was used to generate steam as heat source to the test section in a shell and tube heat exchanger. The tube wall temperature was measured by 10 thermocouples in the test section. Pressure drop was measured at inlet and outlet separately without providing heat source. The results showed a maximum heat transfer enhancement of 160% and a friction factor 300% that of smooth tube. This type of tube will be referred to as 'WTC Tube' further in this report.

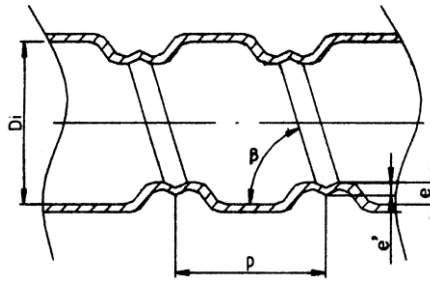


Figure 11: W-type spirally fluted tube by Cui et al. [63].

#### 2.5.4 Spirally Grooved Tube

Jianfeng et al. [141] investigated transition and turbulent heat transfer to molten salt in spirally grooved tube (Figure 12). Molten salt was used as heat transfer fluid in four test sample with different characteristics. Electric heaters were used as heat source to the tube. Six K-type thermocouples were used to measure the temperature at different positions on the tube. The maximum Nusselt number was 1.4 times that of smooth tube in turbulent convection. This type of tube will be referred to as ‘SG Tube’ further in this report.

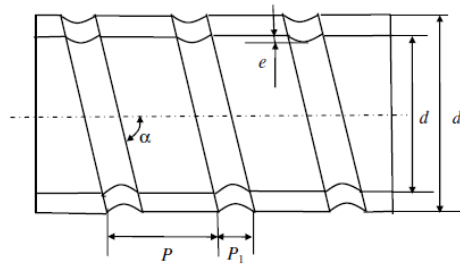
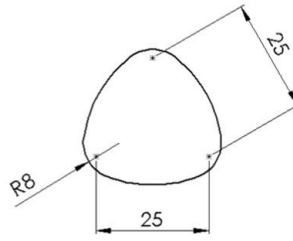


Figure 12: Spirally Grooved Tube by Jianfeng et al. [141].

### 2.5.5 Reuleaux Triangle Cross Section Tube.

Reuleaux Triangle (Rolo) is a geometric shape that is constructed by drawing curves on each side of an equilateral triangle, with radius equal to its side (Figure 13). This shape has never been used for flow applications before. The author proposes such shape because it provides similar perimeter with less cross-sectional area compared to a circle with similar width of curve. This implies that in a tube it will provide more surface area exposed to sun without addition of material, as compared to circular tube. It is also hypothesized that the pressure drop will not be much different from that of circular cross-sectional tube. The final shape has pointy edges, which are rounded to remove the pressure points for fluid inside the pipe, hence making it stronger. This type of tube will be referred to as ‘Rolo Tube’ further in this report.



*Figure 13: Cross sectional sketch of reuleaux triangle.*

## **2.6 Conclusion**

Tubes of various corrugation specifications for are available in literature for heat transfer enhancement. Four tubes with high heat transfer performance are chosen. These tubes are Spirally Corrugated Tube 1 (SC-1) reported by Zimparov et al., Spirally Corrugated Tube 2 (SC-2) reported by Lee et al., W-Type Spirally Fluted Tube (WTC) reported by Cui et al., and Spirally Grooved Tube (SG) reported by Jianfeng et al. The circular tube is chosen as benchmark for other tubes comparison. A new design of tube aka Rolo Tube, will also be compared to the other tubes as it can provide more surface area exposed to solar irradiation.



## CHAPTER 3: COMPUTATIONAL FLUID DYNAMICS

Computational Fluid Dynamics (CFD) is a branch of fluid mechanics that uses numerical analysis to solve real life engineering problems. Flow and interaction of liquids and gasses with surfaces, defined by boundary conditions, are simulated by performing calculations using computer [148].

### **3.1. ANSYS Fluent**

ANSYS Fluent is a CFD software used by Engineers for design and analysis. These tools can simulate fluid flows in a virtual environment. Its application includes but not limited to the fluid dynamics of ships, aircraft aerodynamics, pumps, fans, and HVAC systems [148].

### **3.2. Background**

The physical boundaries of a problem are defined using Computer Aided Design (CAD) whereas the data can be processed further. CAD models are made differently for various problems, i.e. fluid and solid domains. The volumes are divided into discrete cells called mesh. Mesh may be uniform or non-uniform, structured or unstructured, consisting of combination of hexahedral, tetrahedral, prismatic, pyramidal, or polyhedral elements. Physical models like equations of fluid motion is defined. Then the fluid behaviour and boundary properties are defined. In case of transient problem, the initial conditions are also

defined. The simulation is started and the equations are solved iteratively. A postprocessor is used to visualize and analyse the results [148].

### 3.2.1. Navier-Stokes Equations

Navier-Stokes equations, named after Claude-Louis Navier and George Gabriel Stokes, form the basis of almost all CFD problems. In physics, the Navier–Stokes equations describe the motion of viscous fluid substances. These balance equations are derived from applying Newton's second law to fluid motion. The equations are derived under the assumption that the stress in the fluid is the sum of a term proportional to the gradient of velocity (diffusing viscous) and a pressure term. These fundamental partial differential equations describe the flow of incompressible fluids [149]. Navier-Stokes equations assume the forms:

$$\frac{\partial \rho}{\partial t} + \nabla \cdot (\rho \mathbf{u}) = 0, \text{ Continuity Equation}$$

$$\frac{\partial \mathbf{u}}{\partial t} + (\mathbf{u} \cdot \nabla) \mathbf{u} = -\frac{1}{\rho} \nabla p + \mathbf{F} + \frac{\mu}{\rho} \nabla^2 \mathbf{u}, \text{ Equations of Motion}$$

$$\rho \left( \frac{\partial \varepsilon}{\partial t} + \mathbf{u} \cdot \nabla \varepsilon \right) - \nabla \cdot (K_H \nabla T) + p \nabla \cdot \mathbf{u} = 0, \text{ Conservation of Energy}$$

Where  $\mathbf{u}$  is the velocity vector field,  $\varepsilon$  is thermodynamic internal energy,  $p$  is pressure,  $T$  is the temperature,  $\rho$  is the density,  $\mu$  is the viscosity,  $K_H$  is heat conduction coefficient, and  $\mathbf{F}$  is the external force per unit mass, i.e. acceleration.

$$\nabla = \frac{\partial}{\partial x} \mathbf{i} + \frac{\partial}{\partial y} \mathbf{j} + \frac{\partial}{\partial z} \mathbf{k}$$

And,

$$\nabla^2 = \frac{\partial^2}{\partial x^2} + \frac{\partial^2}{\partial y^2} + \frac{\partial^2}{\partial z^2}$$

### **3.3. Turbulent Flow**

In fluid dynamics, turbulent flow regime is characterized by the abrupt changes in pressure and flow velocity. Turbulence is commonly observed in everyday events such as tap water flowing, fast wind, smoke from burning wood, and high-pressure jet washing. Turbulent flows occur commonly in nature and in engineering applications. The fluid particles exhibit additional transverse motion during turbulence, which enhances the rate of energy and momentum exchange between them, thus increasing the heat transfer and the friction coefficient [149]. Models are constructed and used to predict the effects of turbulence in various applications. Turbulence modelling depends on the flow being either external or internal.

### **3.4. Turbulence Modelling in Fluent**

Turbulence models used in Fluent are Reynolds-Averaged Navier-Stokes (RANS) based, which is the most widely used approach for using industrial flows. Other computational approaches include Large Eddy Simulation (LES) and Direct Numerical Simulation (DNS). Some of the RANS based models used in Fluent for simulating flow are as follows:

### **3.4.1. One Equation Models**

Spalart-Allmaras is a low-cost RANS model which solves a transport equation for modified eddy viscosity. In modified form, the eddy viscosity is easier to solve near the wall. This model is mainly used for the aerodynamic applications with mild separation [148].

### **3.4.2. Two Equation Models**

Some of the two-equation models used in Fluent include The Standard k-e (SKE), The Renormalization Group (RNG), Realizable k-e (RKE), Standard k-w (SKW), The Shear Stress Transport k-w (SSTK), Subgrid Scale (SGS), and Detached Eddy Simulation (DES).

#### **3.4.2.1. The standard k-e (SKE) model**

SKE is the most widely used engineering turbulence model for industrial applications. It is robust and reasonably accurate. It contains sub models for compressibility, buoyancy, and combustion. The epsilon equation contains a term that cannot be calculated at the wall, hence wall functions must be used with this model [148]. This work uses the SKE model due to its ease of use and accuracy. It is vastly used for internal flows and uses lesser computational power to solve.

## **3.5. Methodology**

This section describes in detail the CFD parameters used for each tube sample. The geometry construction, the mesh, the boundary conditions, and the approach to solution for each tube sample will be discussed in detail.

### **3.5.1. The Geometry**

The geometries were made using SolidWorks and saved in three different file formats. To edit and fix the tubes they were saved in '.SLDPRT' format. To manufacture in Direct Metal Laser Sintering (DMLS) machine, they were saved in '.stl' format. To import and simulate in ANSYS Fluent, they were saved in '.sat' format. The '.stl' is best suited geometry for the slicing software that comes with the DLSM while the '.sat' provides better and cleaner surface for the ANSYS design modeller environment.

These tubes were originally made hollow in SolidWorks and then filled with fluid domain in ANSYS design modeller. This was done using the fill option in the design modeller, after creating thin caps on inlets and outlets of each tube. The tubes were made in original size presented in literature, but then scaled to achieve similar outer surface area for all tubes. The surface areas of tubes remained in  $\pm 10\%$  of the surface area of the benchmark, i.e. circular tube. The outer surfaces of the tubes were split into two halves using the 'face split' option in design modeller. This was done so one half can be specified with different boundary condition. This half face will be subjected to heat flux because only half of the tube surface remains exposed in the experiment.

The original outer geometries were specified as solids while the inner geometries were specified as fluid domains. Aluminium is chosen for the tube material, and this choice will be explained in section 4.2.1 of Chapter 4. Specifications and pictures of each tube are provided as follows.

### 3.5.1.1. Circular Tube

The DLSSM is limited in size of product, hence no pipe could be manufactured longer than 200 mm. Additional 10 mm was left at the base of tubes to provide clearance while cutting the produced tube from the metal plate. The thickness was set at 2 mm for all tubes because the 1 mm thickness would result in breaking of the tubes during manufacturing, due to their complex geometry. Table 1 shows the dimensions of circular tube as modelled in CAD for manufacturing.

*Table 1: Dimensions of Circular Tube.*

<b>Inner Diameter</b>	25.9 mm
<b>Thickness</b>	2 mm
<b>Hydraulic Diameter</b>	25.9 mm
<b>Total Surface Area</b>	18786.72 mm <sup>2</sup>
<b>Length</b>	200 mm
<b>Volume / Weight</b>	3.506017e-5 m <sup>3</sup> / 0.035 KG

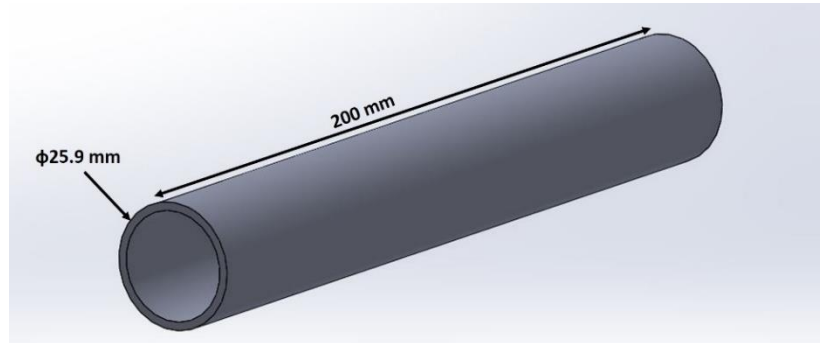


Figure 14: SolidWorks model of Circular Tube.

### 3.5.1.2. SC-1 Tube

Table 2 shows the dimensions of SC-1 Tube as modelled in CAD for manufacturing.

Table 2: Dimensions of SC-1 Tube.

<b>Inner Diameter</b>	25.2 mm
<b>Thickness</b>	2 mm
<b>Hydraulic Diameter</b>	24.15 mm
<b>Total Surface Area</b>	18830.66 mm <sup>2</sup>
<b>Total Length</b>	200 mm
<b>Volume / Weight</b>	3.492356e-5 m <sup>3</sup> / 0.0349 KG

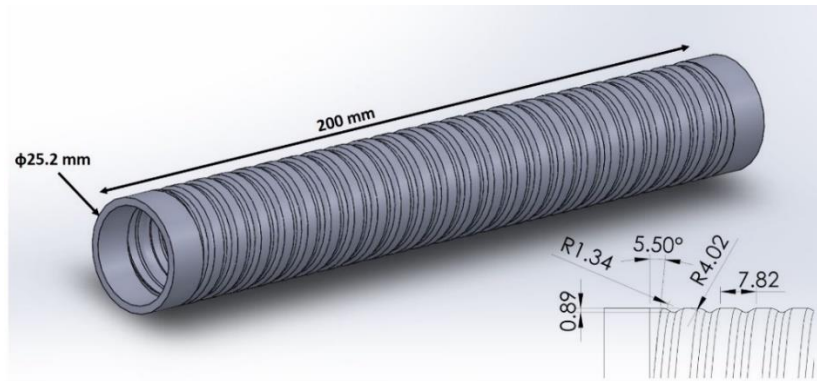


Figure 15: SolidWorks model of SC-1 Tube.

### 3.5.1.3. SC-2 Tube

Table 3 shows the dimensions of SC-2 Tube as modelled in CAD for manufacturing.

Table 3: Dimensions of SC-2 Tube.

<b>Inner Diameter</b>	21.94 mm
<b>Thickness</b>	2 mm
<b>Hydraulic Diameter</b>	21.57 mm
<b>Total Surface Area</b>	19161.29 mm <sup>2</sup>
<b>Total Length</b>	200 mm
<b>Volume / Weight</b>	3.715197e-5 m <sup>3</sup> / 0.03715 KG



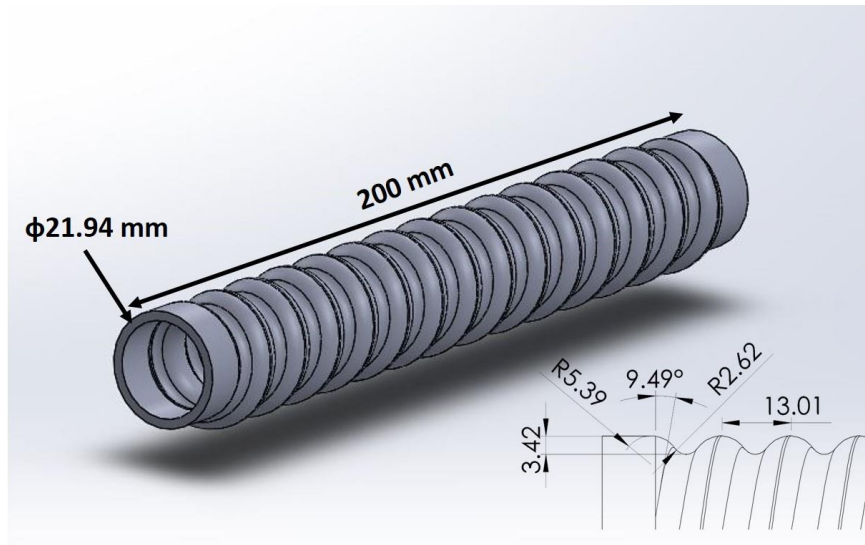


Figure 16: SolidWorks model of SC-2 Tube.

### 3.5.1.4. WTC Tube

Table 4 shows the dimensions of WTC Tube as modelled in CAD for manufacturing.

*Table 4: Dimensions of WTC Tube.*

<b>Inner Diameter</b>	22 mm
<b>Thickness</b>	2 mm
<b>Hydraulic Diameter</b>	23.51 mm
<b>Total Surface Area</b>	17775.72 mm <sup>2</sup>
<b>Total Length</b>	200 mm
<b>Volume / Weight</b>	2.810232e-5 m <sup>3</sup> / 0.0281 KG

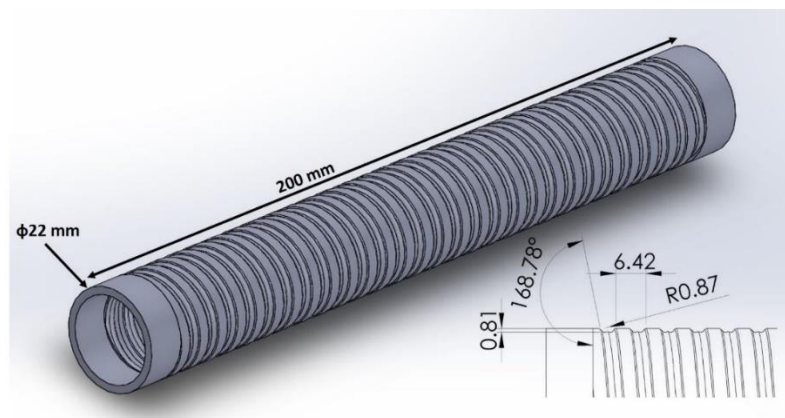


*Figure 17: SolidWorks model of WTC Tube.*

### 3.5.1.5. SG Tube

Table 5 shows the dimensions of SG Tube as modelled in CAD for manufacturing.

*Table 5: Dimensions of SG Tube.*

<b>Inner Diameter</b>	25.28 mm
<b>Thickness</b>	2 mm
<b>Hydraulic Diameter</b>	23.56 mm
<b>Total Surface Area</b>	19390.8 mm <sup>2</sup>
<b>Total Length</b>	200 mm
<b>Volume / Weight</b>	3.421133e-5 m <sup>3</sup> / 0.0342 KG

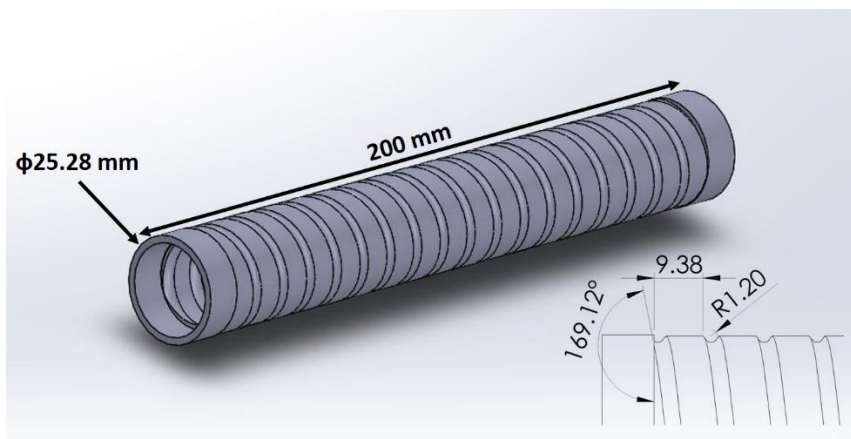


*Figure 18: SolidWorks model of SG Tube.*

### 3.5.1.6. Rolo Tube

Table 6 shows the dimensions of Rolo Tube as modelled in CAD for manufacturing.

Table 6: Dimensions of Rolo Tube.

<b>Inner Diameter</b>	29.12 mm
<b>Thickness</b>	2 mm
<b>Hydraulic Diameter</b>	21.65 mm
<b>Total Surface Area</b>	20921.26 mm <sup>2</sup>
<b>Total Length</b>	200 mm
<b>Volume / Weight</b>	4.064123e-5 m <sup>3</sup> / 0.0406 KG

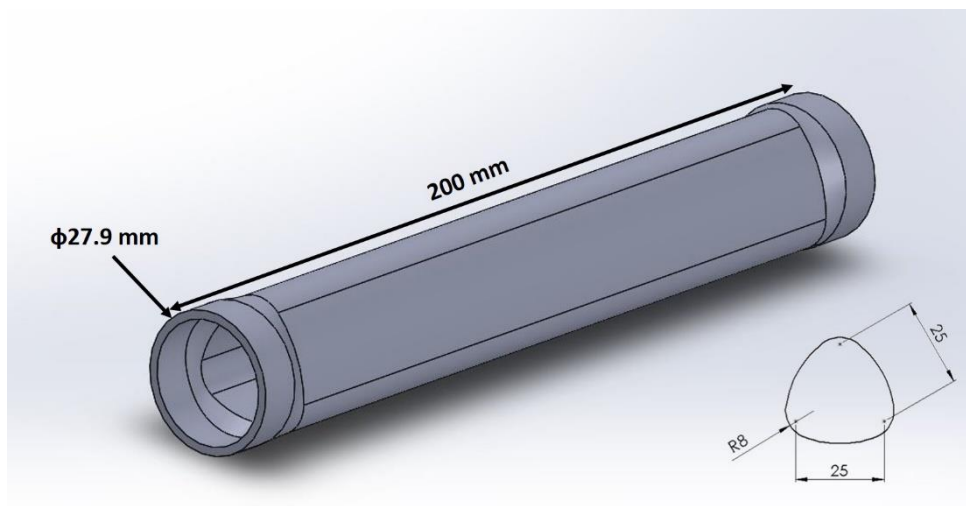


Figure 19: SolidWorks model of Rolo Tube.

### **3.5.2. The Mesh**

The boundaries were named in this section. The tubes had inlet, outlet, insulated walls (one half of the surface), and heat flux wall (the half surface exposed to heat). The interface connections between aluminium inner walls and the fluid outer walls were automatically defined in ANSYS mesh. These connections were manually checked and defined where they were missing. This step is crucial for establishing heat transfer between the two mediums. The mesh physics preference was set to CFD with Fluent solver and automatic method was used for meshing.

#### **3.5.2.1. Circular Tube**

Advanced size function on curvature with fine relevance centre was used. The smoothing was kept high with a slow transition and a fine span angle. Minimum element size was defined at 0.01mm and maximum element and face size was defined at 1mm. Growth rate remained default at 1.2. The patch conforming was left program controlled. The resulting mesh statistics for this tube are provided in Table 7.

*Table 7: Mesh specifications of Circular Tube.*

<b>Number of Elements</b>	7716093
<b>Number of Nodes</b>	8008598
<b>Maximum Aspect Ratio</b>	4.8576
<b>Maximum Orthogonal Quality</b>	0.99998
<b>Maximum Skewness</b>	0.56016

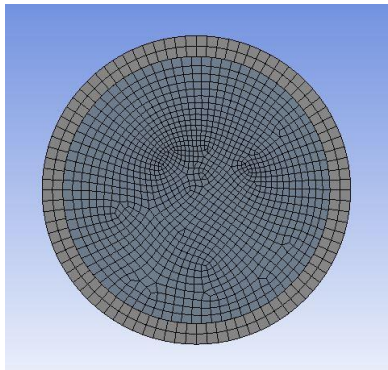


*Figure 20: CFD mesh of Circular Tube.*

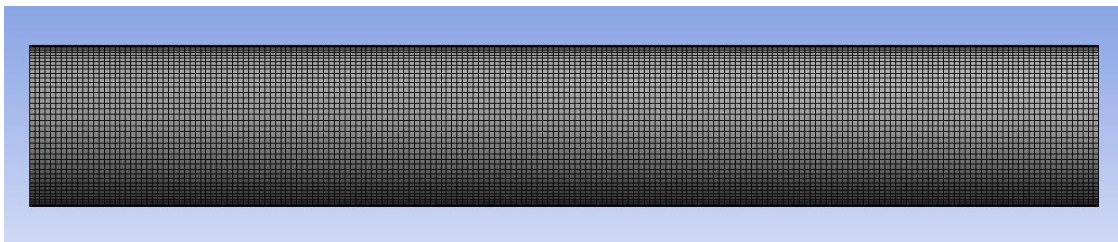


*Figure 21: CFD mesh of Circular Tube wall.*

Figure 22 shows the grid independence test of circular tube. Grid independence is a process where the sufficiency of number of mesh elements is established by observing the change in result with the change in number of mesh elements. Due to limited computational resource and time, the grid independence test could not be carried for all tubes. The number of elements of circular tube were kept as benchmark for all other tubes.

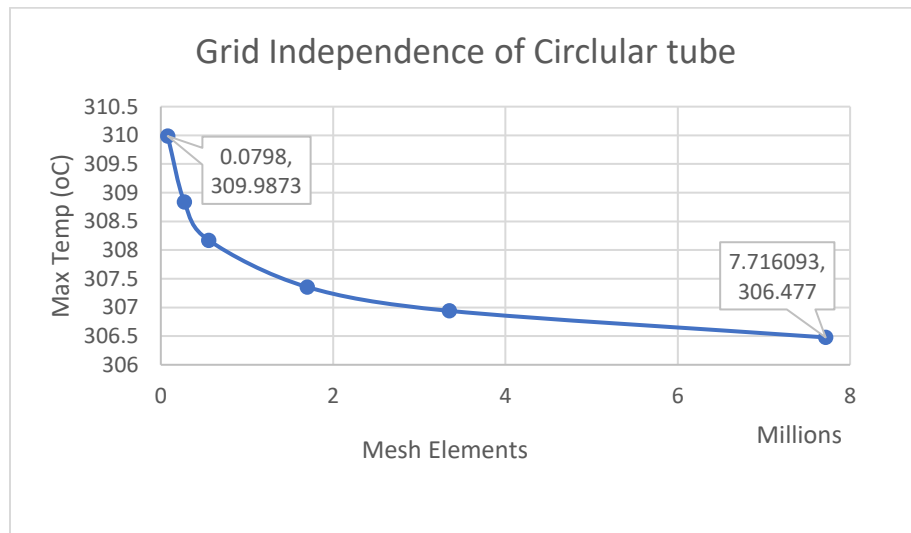


Figure 22: Grid Independence of Circular Tube.

### 3.5.2.2. SC-1 Tube

Advanced size function on curvature with fine relevance centre was used. The smoothing was kept high with a slow transition and a fine span angle. Minimum element size was defined at 0.01mm and maximum element and face size was defined at 1mm. Growth rate

remained default at 1.2. The patch conforming was left program controlled. The resulting mesh statistics for this tube are provided in Table 8.

*Table 8: Mesh specifications of SC-1 Tube.*

<b>Number of Elements</b>	6448642
<b>Number of Nodes</b>	7224319
<b>Maximum Aspect Ratio</b>	132.15
<b>Maximum Orthogonal Quality</b>	0.998
<b>Maximum Skewness</b>	0.75

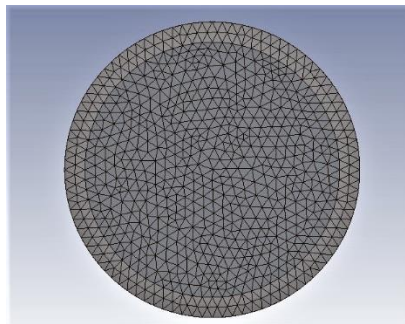


*Figure 23: CFD mesh of SC-1 Tube.*



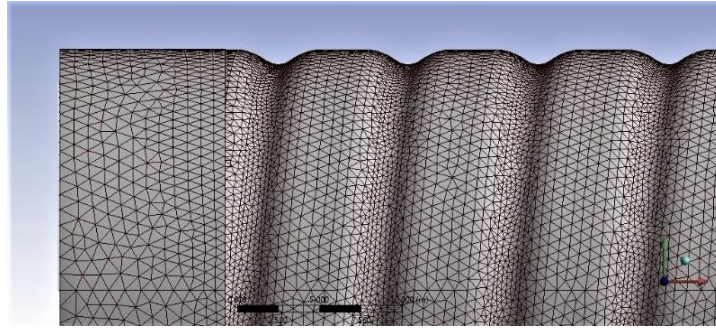


*Figure 24: CFD mesh of SC-1 Tube wall.*

### **3.5.2.3. SC-2 Tube**

Advanced size function on curvature with fine relevance centre was used. The smoothing was kept high with a slow transition and a fine span angle. Minimum element size was defined at 0.01mm and maximum element and face size was defined at 1mm. Growth rate remained default at 1.2. The patch conforming was left program controlled. The resulting mesh statistics for this tube are provided in Table 9.

*Table 9: Mesh specifications of SC-2 Tube.*

---

<b>Number of Elements</b>	4253411
<b>Number of Nodes</b>	768715
<b>Maximum Aspect Ratio</b>	14.373
<b>Maximum Orthogonal Quality</b>	0.99808
<b>Maximum Skewness</b>	0.94711

---

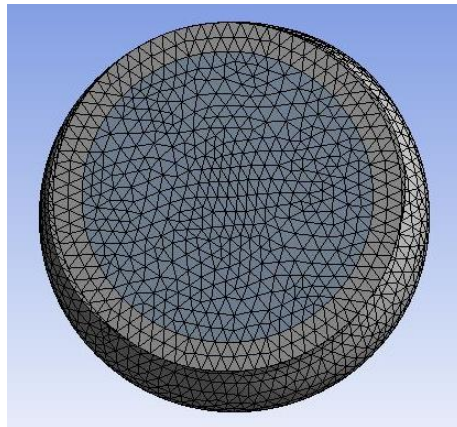


*Figure 25: CFD mesh of SC-2 Tube.*

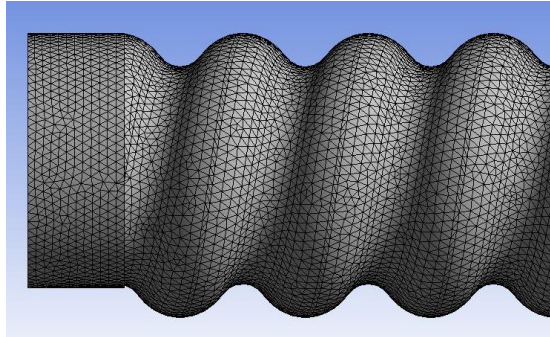


*Figure 26: CFD mesh of SC-2 Tube wall.*

#### **3.5.2.4. WTC Tube**

Advanced size function on curvature with medium relevance centre was used. The smoothing was kept medium with a slow transition and a fine span angle. Minimum element size was defined at 0.01mm and maximum element and face size was defined at 1mm. Growth rate remained default at 1.2. The patch conforming was left program controlled. Table 10 provides the resulting mesh statistics.

*Table 10: Mesh specifications of WTC Tube.*

<b>Number of Elements</b>	6079769
<b>Number of Nodes</b>	1219014
<b>Maximum Aspect Ratio</b>	54.67
<b>Maximum Orthogonal Quality</b>	0.99732
<b>Maximum Skewness</b>	0.98658

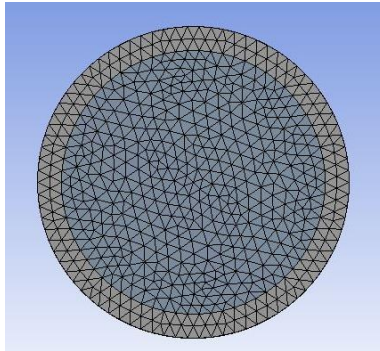


*Figure 27: CFD mesh of WTC Tube.*

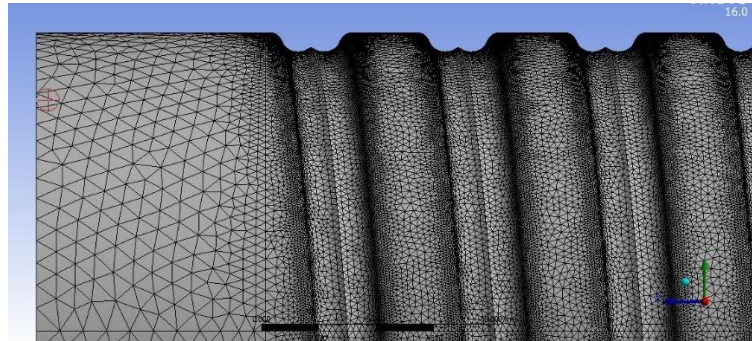


*Figure 28: CFD mesh of WTC Tube wall.*

#### **3.5.2.5. SG Tube**

Advanced size function on curvature with fine relevance centre was used. The smoothing was kept high with a slow transition and a fine span angle. Minimum element size was defined at 0.01mm and maximum element and face size was defined at 1mm. Growth rate remained default at 1.2. The patch conforming was left program controlled. The resulting mesh statistics for this tube are provided in Table 11.

*Table 11: Mesh specifications of SG Tube.*

<b>Number of Elements</b>	4462900
<b>Number of Nodes</b>	816421
<b>Maximum Aspect Ratio</b>	17.783
<b>Maximum Orthogonal Quality</b>	0.99725
<b>Maximum Skewness</b>	0.95664

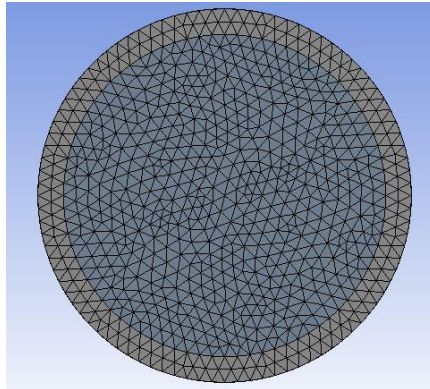


*Figure 29: CFD mesh of SG Tube.*

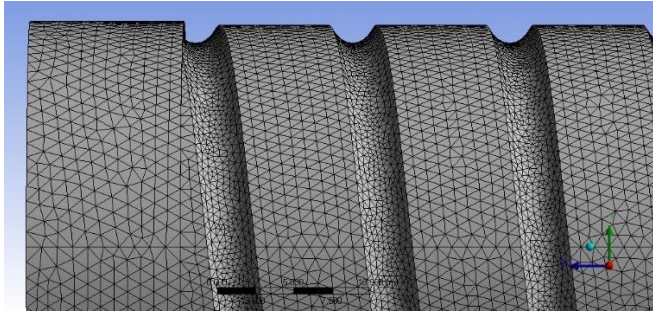


*Figure 30: CFD mesh of SG Tube wall.*

#### **3.5.2.6. Rolo Tube**

Advanced size function on curvature with fine relevance centre was used. The smoothing was kept high with a slow transition and a fine span angle. Minimum element size was defined at 0.01mm and maximum element and face size was defined at 1mm. Growth rate remained default at 1.2. The patch conforming was left program controlled. The resulting mesh statistics for this tube are provided in Table 12.

*Table 12: Mesh specifications of Rolo Tube.*

<b>Number of Elements</b>	4913356
<b>Number of Nodes</b>	887160
<b>Maximum Aspect Ratio</b>	10.521
<b>Maximum Orthogonal Quality</b>	0.99733
<b>Maximum Skewness</b>	0.84443

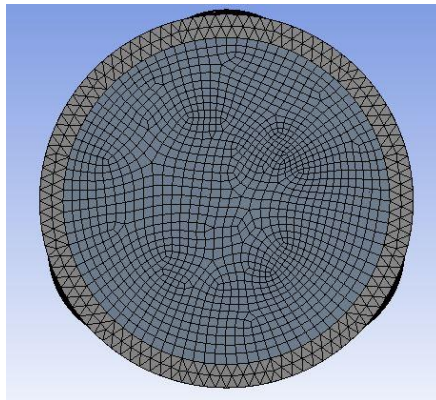


*Figure 31: CFD mesh of Rolo Tube.*



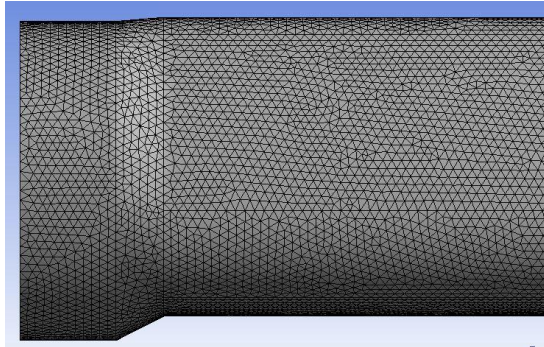


*Figure 32: CFD mesh of Rolo Tube wall.*

### **3.5.3. The Setup**

The entire computation was run with double precision and parallel processing. The solver was set to pressure-based steady state. The gravity was turned on and set to  $-9.81 \text{ m/s}^2$  in the Z axis (vertical). The energy model was turned on and the K-epsilon model with enhanced wall treatment was used.

The reason K-epsilon was used is that this model is robust and accurate for turbulent flows. It can easily adapt for compressibility, buoyancy, combustion, etc. With appropriate wall function, this model will solve the system with less computational power.

The surfaces of tubes were named in mesh editor as Inlet, Outlet, Insulated Walls, and Heated Walls. The boundary conditions will be further discussed in section 3.5.3.1. Materials were set to Aluminium and Water. Aluminium is the outer tube while the inner fluid was set to Water. These selections were carried out by choosing from FLUENT material database and then specifying in the cell zone conditions. The properties of both materials are given in Table 13.

Table 13: Material properties for fluid & solid domains.

<b>Water</b>	
<b>Density</b>	998.2 kg/m <sup>3</sup>
<b>Dynamic Viscosity</b>	0.001003 kg/m-s
<b>Thermal Conductivity</b>	0.6 W/m-k
<b>Specific Heat Capacity</b>	4182 j/kg-K

<b>Aluminium</b>	
<b>Density</b>	2719 kg/m <sup>3</sup>
<b>Thermal Conductivity</b>	202.4 W/m-k
<b>Specific Heat Capacity</b>	871 j/kg-K

Table 14 shows the solution method used for solving the system and was kept consistent for all tube samples.

Table 14: Solution methods.

---

<b>Pressure-Velocity Coupling</b>	SIMPLE
<b>Gradient</b>	Least Squares Cell Based
<b>Pressure</b>	Second Order
<b>Momentum</b>	Second Order Upwind
<b>Turbulent Kinetic Energy</b>	Second Order Upwind
<b>Turbulent Dissipation Rate</b>	Second Order Upwind
<b>Energy</b>	Second Order Upwind

---

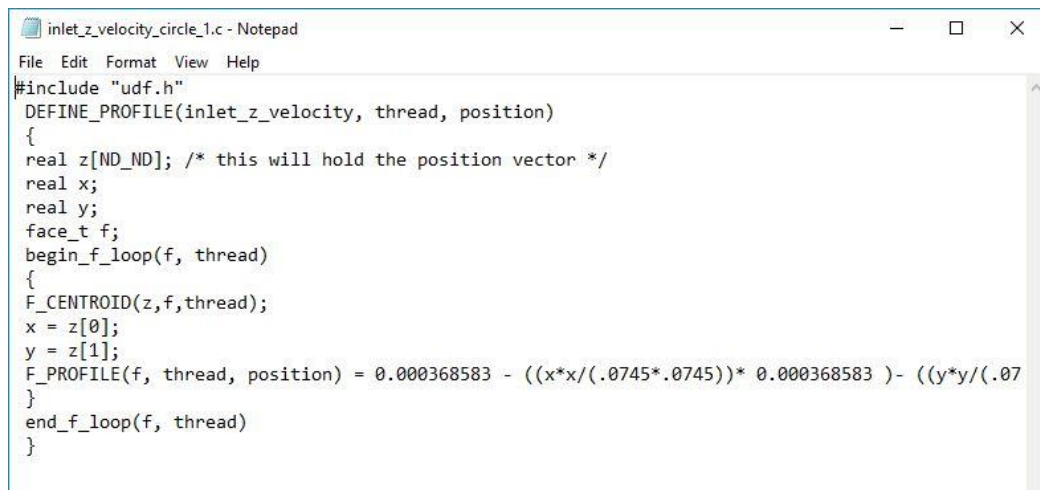
All residuals were set to  $1 \times 10^{-7}$ , the solution was initialized using hybrid initialization, and the number of iteration was set to 1000.

### 3.5.3.1. The Boundary Conditions

The inlet boundary was set to ‘velocity-inlet’ with magnitude specified normal to the boundary. The Turbulent intensity percentage is kept at 5% and a turbulent viscosity ratio of 10 was specified. The magnitude of velocity was different for all tubes, calculated from mass flow rate and hydraulic diameter of each tube, which corresponds to the same Reynolds number. The simulation was repeated with 24 different velocity magnitudes at inlet.

The inlets of each tubes are kept circular so they could be connected to rig easily and a UDF was used for developed flow in simulation. For this purpose, the velocity magnitude would be specified in the UDF file whereas the UDF was used in the inlet boundary condition

window. The UDF is defined for parabolic velocity profile and the code was written in a text editor. The code was saved as '.h' file format and then interpreted in Fluent, before being selected in the velocity magnitude (Figure33). The velocity magnitudes used for each trial of all samples are provided in Table 15.



```
inlet_z_velocity_circle_1.c - Notepad
File Edit Format View Help
#include "udf.h"
DEFINE_PROFILE(inlet_z_velocity, thread, position)
{
  real z[ND_ND]; /* this will hold the position vector */
  real x;
  real y;
  face_t f;
  begin_f_loop(f, thread)
  {
    F_CENTROID(z,f,thread);
    x = z[0];
    y = z[1];
    F_PROFILE(f, thread, position) = 0.000368583 - ((x*x/(.0745*.0745))* 0.000368583) - ((y*y/(.0745*.0745))* 0.000368583);
  }
  end_f_loop(f, thread)
}
```

Figure 33: UDF example for Inlet boundary condition.

Table 15: Inlet velocity magnitudes in m/s.

<b>Circular</b>	<b>SC-1</b>	<b>SC-2</b>	<b>WTC</b>	<b>SG</b>	<b>Rolo</b>
0.000368583	0.000422347	0.000530992	0.000450046	0.000444523	0.000442195
0.000332089	0.000382013	0.000479348	0.000403138	0.000402154	0.00039507
0.000302035	0.00034991	0.000438033	0.00036926	0.000366702	0.000364225
0.000281283	0.000325216	0.000407047	0.0003432	0.000340761	0.000335093
0.000252661	0.000290644	0.000366764	0.000307585	0.000307039	0.000301677
0.000225469	0.000257718	0.000324416	0.000273707	0.000271587	0.000269118
0.000187544	0.000217384	0.00027174	0.0002268	0.000229218	0.000224564
0.000173232	0.000199275	0.000252115	0.000212032	0.000208466	0.000207427
0.000146041	0.000167172	0.000209767	0.000175548	0.000176472	0.000174868
0.000110262	0.000126015	0.000159156	0.000134721	0.000131509	0.00013117
9.45197E-05	0.000113668	0.000137466	0.000119954	0.00011508	0.00011232
6.51814E-05	7.58035E-05	9.71836E-05	7.99954E-05	8.04931E-05	7.97614E-05

The half surface faces that were split in design modeller are specified as heat flux wall boundary. The heat flux values are kept at  $150 \text{ W/m}^2$  from outside, to simulate the irradiance which covers major portion of the globe (as discussed in section 1.1.1).

The tubes are modelled in computer and prepared for simulation. The simulation will focus on the flow turbulence inside each tube. The results from these simulations will be discussed in Chapter 5.

## CHAPTER 4: EXPERIMENTAL SETUP

Much of the apparatus used in this work was fabricated at the workshop and additive manufacturing laboratory of Qatar University. This chapter discusses the design of experiment, setup, and fabrication of each part of the apparatus in detail.

### **4.1. Design of Experiment**

The entire apparatus consisted of a closed flow loop to provide water at inlet of test sample tube at a fixed temperature (Figure 34). Radiation was provided to the outer surface of the tube which heated the water flowing inside. 10 thermocouples measured temperature at inlet, outlet, and 4 stations of the test sample. The test was repeated for 20 different flow rates ranging from 1 L/min to 11.5 L/min, i.e. in transitional, and turbulent flow regions. The flow was controlled via a valve while the flow and temperature data was recorded by a data acquisition system connected to a computer.

The apparatus consisted of two halogen lamps acting as solar irradiation simulator, a complete test rig with replaceable tube samples for the heat transfer test, thermocouples, and a flow meter for measuring temperatures at different stations on the samples, a data acquisition system to collect the data, and a computer to store the data. A tank, pump, and chiller apparatus was used to store, supply, and cool the distilled water.

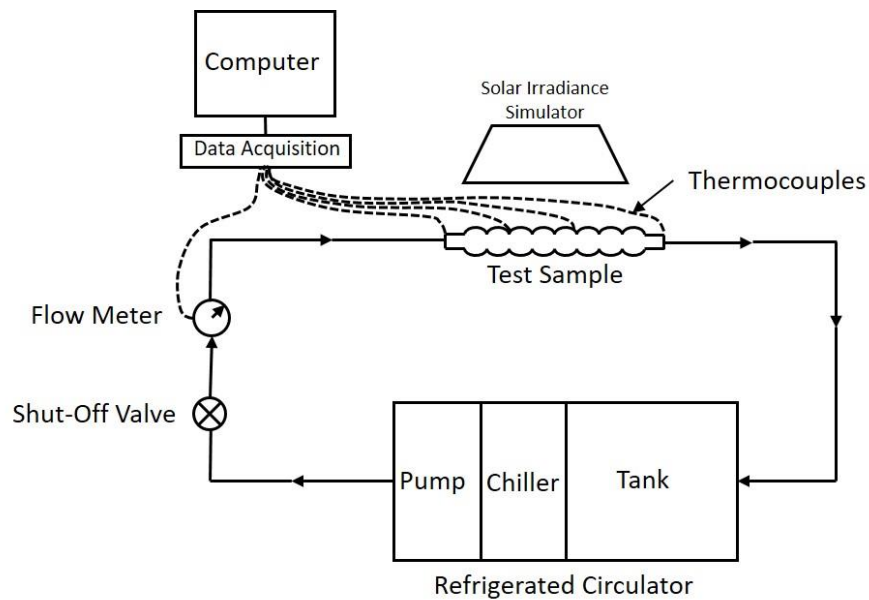


*Figure 34: Schematic of the closed loop flow.*

The thermocouples and flow meter were first calibrated and their calibration curves were produced. Parts of the system were readily available while some parts were manufactured. The following sections will discuss the parts that were readily available, the parts that were manufactured for this experiment, and the calibration of measurement devices.

#### **4.1.1. Refrigerated Circulator**

Julabo FP50 refrigerated circulator was used. It contains a tank, a chiller, and a pump that provided a closed loop cycle of distilled water at a constant inlet temperature (Figure 35). This model has a working temperature of  $-40^{\circ}\text{C}$  to  $200^{\circ}\text{C}$  with a  $0.68\text{kW}$  cooling capacity at  $20^{\circ}\text{C}$  and a temperature stability of  $\pm 0.01^{\circ}\text{C}$ . The pump has four stages of flow rate, ranging

from 22 L/min to 26 L/min at 0 pressure drop. The tank has a volume of 8 litres. This machine is 37 x 46 x 71 cm and weighs 49 kg. It has small rollers for mobility inside the laboratory. 230 Volts 3 phase power at 50 Hz is required to run this machine. The electronic interface was used to start/stop the water flow and set temperature for the outlet water. The flow could not be controlled freely, so a separate external valve was used in the loop to control the flow according to need.



*Figure 35: Julabo FP50 Chiller.*



#### 4.1.2. Flow Control Valve

A plastic shut-off valve was used for controlling the flow (Figure 36). A flow meter was used for determining the valve position corresponding to flow rates for each tube sample. The valve is made of HDPE plastic with connections for snap-in adapters. This is used with refrigerated circulator to flexibly adapt to various systems.



*Figure 36: HDPE shut-off valve.*

#### 4.1.3. Flow Meter

High precision turbine wheel flow meter manufactured by KOBOLD was used for measurement of flow in this experiment (Figure 37). These type of flow meters have a wide range of applications. This type of flow meter was chosen so the rig can be used in future for different fluid flows. Furthermore, these flow meters are durable and easy to maintain. The flow meter used for this experiment is made of stainless steel and has a range of 0.5 L/min

to 25 L/min. It has a diameter of  $\frac{3}{4}$  inch and a measurement accuracy of  $\pm 1.25\%$  with water as fluid. The inlet and outlet are threaded for connection to the loop.



*Figure 37: High precision turbine wheel flow meter.*

These flow meters have a maximum operating temperature of  $135^{\circ}\text{C}$  and produce pulses that are transmitted to universal DC input meter.

#### **4.1.4. Universal DC Input Meter**

A universal DC input meter by Red Lion was used for flow rate measurement (Figure 38). It has a display that shows the voltage generated from the flow meter. This AC powered device was connected to the data acquisition for storing the flow rate data and has an uncertainty of  $\pm 10\%$ . The display was used for live monitoring and controlling of flow rate. The flow meter was calibrated with the voltage output displayed in this device. The calibration curves will be presented in section 4.6.



*Figure 38: Universal DC input meter.*

#### **4.1.5. Thermocouples**

Fluke 80PK-1 bead probe thermocouple was used for measuring temperatures (Figure 39). The complex geometry tubes did not have uniform surface and were only 2 mm thick. For this reason, the thread or probe type thermocouple could not be used. Such thermocouples would also prevent the radiation from reaching the surface. Hence bead probe thermocouples were used. 1.5mm holes were drilled at inlet/outlet and 4 stations of test sample and the bead probes were inserted in a way that only the bead would intrude inside the tube. This way the bead is kept in water close to the tube wall without disturbing the flow of water. The K-Type thermocouple is widely used most accurate thermocouple with a measurement range of -40°C to 260°C. It has an accuracy of 1.1°C. These thermocouples had 1-meter Teflon cable which terminated with a Type K miniature thermocouple connector with 0.792-mm pin spacing.



*Figure 39: Fluke 80PK-1; bead probe K-Type thermocouple.*

These thermocouples were installed at 4 stations, named as St-1, St-2, St-3, and St-4. The thermocouples at inlet and outlet were named as 'Inlet' and 'Outlet'. The distance between each station was 35mm. Each station had two thermocouples coded as 1 and 2, hence the thermocouples could be identified as Th 1-1, Th 1-2, i.e. 'Station-1: Thermocouple-2' and 'Station-1: Thermocouple-2' respectively. Both the thermocouples were kept at a radial distance of  $30^\circ$  from vertical (Figure 40).

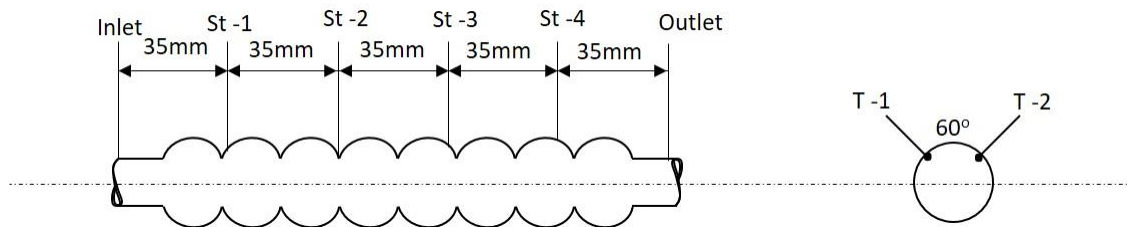


*Figure 40: Thermocouples installed in tubes.*

#### **4.1.5.1. Leak Prevention**

Thermocouples inserted in the drilled holes resulted in water leakage from the measurement points. The leakage needed to be stopped by using methods that would not prevent radiation from reaching the surface of tube, resist the heat, and not obstruct the fluid flow inside the pipe. Adhesive used for this purpose would also have to be easily removable to enable the reuse of thermocouples. Some solutions that could prevent the leak would not hold the thermocouple fixed to the tube whereas other that could hold the thermocouple fixed to the tube could not prevent the leak. For these reasons epoxy adhesive was used to fix the thermocouple to the tube while silicon paste would be applied above it to prevent the leak. The silicon would be allowed to dry overnight. The epoxy would hold the thermocouples tight and was easily removed after use. Epoxy becomes hard and somewhat brittle and can be scraped off by using sharp tool or plier.

#### **4.1.6. Data Acquisition**

Fluke Hydra 2635A/C Portable Data Acquisition was used for recording and collecting data. It has a range of 90mV to 300/25% V on AC power and a resolution of 1uV to 10 uV. It supports many types of thermocouples including J, K, and T types. This acquisition system has 20 channels and a storage card with a memory capacity of 4M (Figure 41). The system was compatible with Fluke thermocouple but the connectors were different. The thermocouples had to be connected to the acquisition via wired connection to the system. The thermocouples were labelled close to the acquisition and the tube, for identification.



*Figure 41: Fluke data acquisition system.*

#### **4.1.7. Solar Irradiance Simulator**

A wooden box with dimensions 30cm x 25cm x 25cm was fabricated in the wood workshop. It was covered with aluminium tape to keep the wood from absorbing radiation heat. Two 500W halogen lamps were fitted inside the box at an angle to each other, in a way that all the light can be concentrated to one line. A hole was drilled at the back of the box, to allow for the wire connection of the halogen lamps. The lamps were separated from the wooden box by a layer of refractory ceramic fibres to prevent the wood from catching fire due to the heat of the lamps. The box dimensions were kept sufficient to cover only the test sample. The box was designed for a vertical test rig, so a ‘U’ shaped cut was made in the wooden box so the sample tube could be moved towards and away from the halogen lamps. The box was placed on a table with the ‘U’ shaped cut hanging outside the edge of table, while the rig was supported from the ground (Figure 42).

Two 500W Philips tungsten halogen lamps were used. The tungsten bulbs were 4.7 inches double end connected to halogen lamp casings. These casings facilitated concentrating light efficiently on the test section. With the distance of the U-shaped cut, two 500W lamps were calculated to provide  $150 \text{ W/m}^2$  at the surface of the tube (solar irradiation map, section 1.1.1). This was verified by measuring the light close to surface of the test tube. A lux meter was used, the value in lux was then converted to watts per square meter, while considering the wavelength of the light from halogen lamp.

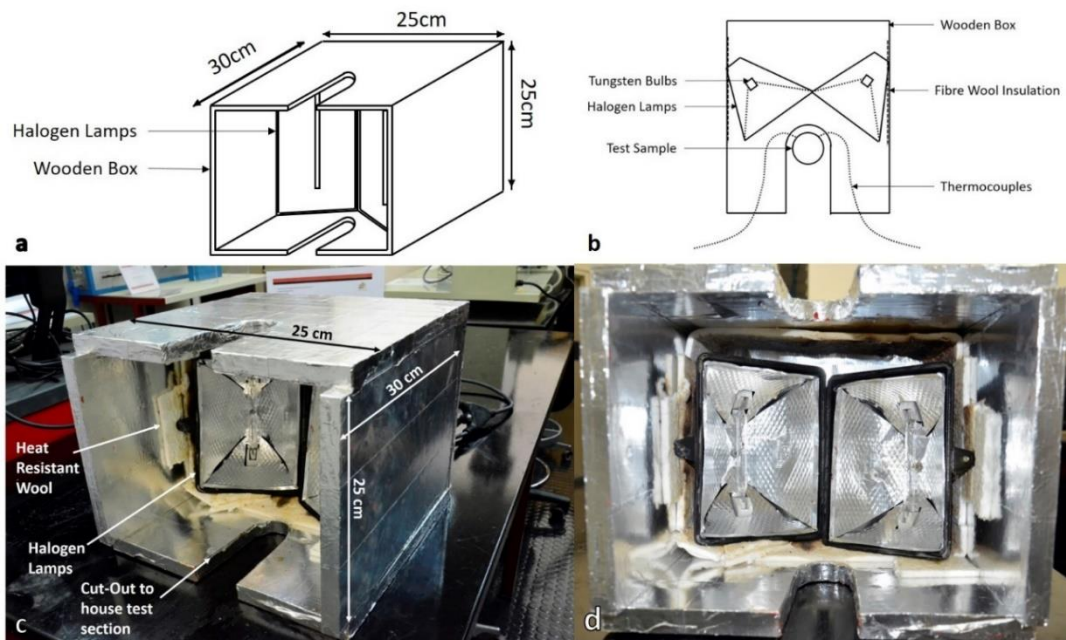


Figure 42: (a) Solar Irradiance Simulator sketch; (b) Top view; (c) Actual photo; (d) Inside box.

## **4.2. Fabrication of Tubes**

The geometry for tubes were adopted from the literature, as discussed in chapter 2. The required tubes were first designed and modelled using SolidWorks. The SolidWorks models were scaled down to desired size for the experiment. These complex unconventional tube shapes are difficult to manufacture or acquire from market. Hence the tubes had to be made either by casting or Direct Metal Laser Sintering (DMLS) technique. Casting is an expensive and time-consuming process. Moreover, this technique is not ideal for tubes of 2mm thickness. Hence the DMLS machine was used for manufacturing the tubes. DMLS machine can fabricate thin walled tubes of complex cross-sectional geometry.

### **4.2.1. Direct Metal Laser Sintering (DMLS)**

DMLS is an additive manufacturing metal fabrication technology that produces metal parts from CAD model (Figure 43). DMLS uses a variety of alloys and enables the design of organic geometries, internal features, complex features, and challenging passages that were impossible to be cast or otherwise machined. This is because the parts are built layer by layer in this technique.



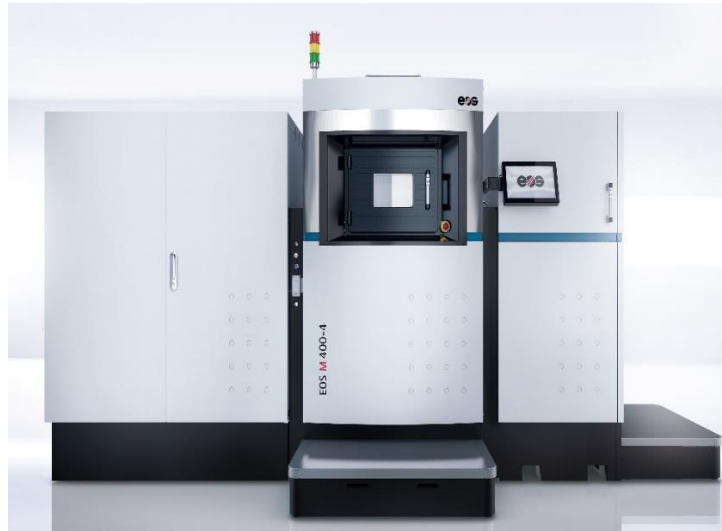


*Figure 43: DMLS machine.*

A 3D CAD model is created using CAD software, converted to '.stl' format, and then sent to the machine's computer. A trained technician properly orients the 3D model in the computer program for part building. Support structures are added where required. The resulting data is called "build file", which is then sliced into thin layers via slicing software compatible with the machine. The DMLS uses a 200 watt Yb-doped fiber optic laser which is used to focus laser beam at the metal powder to fuse it.

#### **4.2.2. Working of DMLS**

The print chamber consists of three platforms. A space for storing aluminium or titanium powder, a metal plate where the part is made, and a space for discarded powder. Aluminium or titanium powder is spread out on the metal plate in thin layer by a roller. The print chamber

is then heated up but the powder does not melt yet. It is melted when the laser touches it, at those areas of the layer that are part of the design. The 3D printer will repeat spreading out one layer of powder after another, and the laser will systematically focus beam on the correct spots of each layer and this way the object is sintered together. This way the entire part is produced layer by layer (Figure 44). This technology is used to manufacture parts for a variety of industries including medical, aerospace, dental, tooling industry, and other industries that have highly complex parts. DMLS is used for rapid prototyping and production manufacturing of complex geometries as it is a very cost and time effective technology.

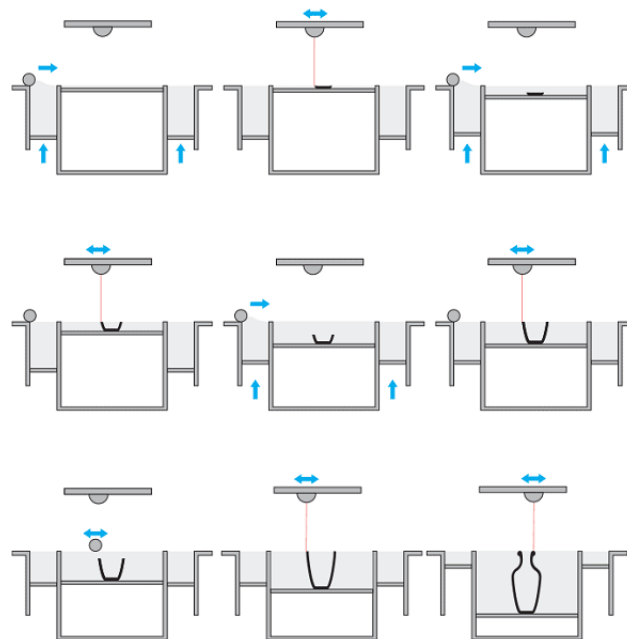


Figure 44: DMLS technique.

The maximum dimension of the chamber is 20cm, hence the tubes could not be built more than this in length. 10mm on each side of the tubes were kept circular for easy connection to the rig. The tubes were manufactured with a thickness of 2mm. Once the tubes were printed, they were sandblasted to remove excess aluminium powder. The tubes were then cut from the base plate and sandblasted again. This time all the aluminium powder was removed and the surface was slightly smoothed. Aluminium powder is hazardous to health in the long run, hence safety was practiced with utmost importance. This machine can house many metals like tin and stainless steel, but aluminium was chosen for this experiment because of its better heat conduction property.

#### **4.2.3. Safety Precautions with DMLS.**

Qatar University's '*Laboratory\_Safety\_Policy\_Oct\_2013*' was followed always while working on the machine. Coverall, cleanroom gloves, headcover, and full-face respirators were used while handling the fine aluminium powder. No one was allowed inside the laboratory without the required safety harness.

### 4.3. The Test Samples

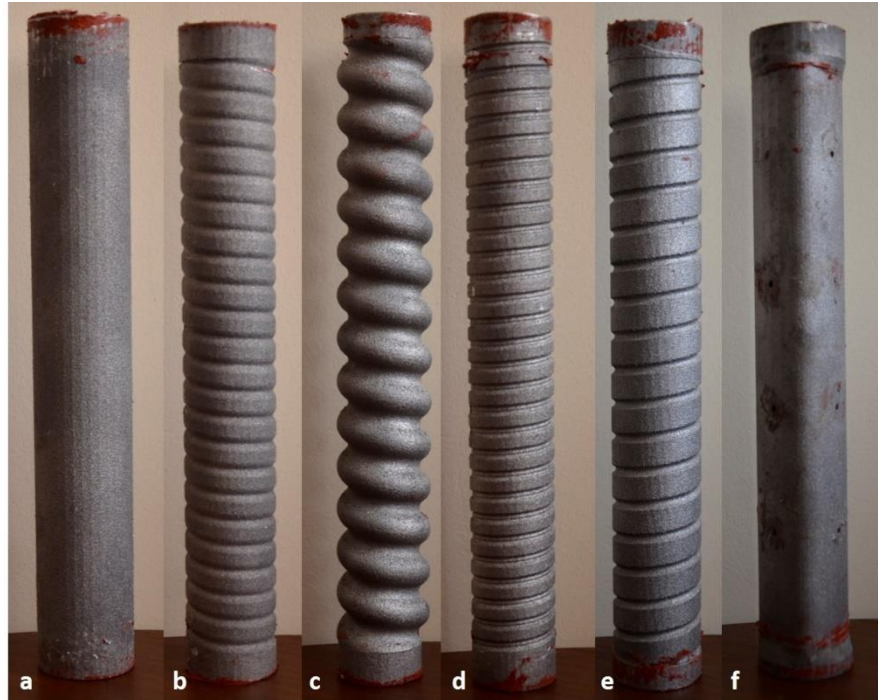


*Figure 45: Manufactured tubes; (a) Circular, (b) SC-1, (c) SC-2, (d) WTC, (e) SG, (f) Rolo.*

Because the part is made from powder, the final products have a very coarse finish and needs to be polished by sand blasting or laser polishing. However, due to inaccuracy in achieving smooth surface inside as well as outside the tube, all the tubes were kept similarly rough to mitigate any effect while saving time. The work space dimensions are limited to 20 cm only, hence a larger part could not be made. All tubes were made 200mm with 10mm circular

section on each side for connection (Figure 45). This left only 180mm of complex geometry length.

#### **4.4. Connections and Reducers**

Because the tubes were of different diameters than the standard sizes available in the market, reducers and connectors were to be printed separately for each tube. These reducers were not subject to heat transfer so they were not required to be made from aluminium. Plastic 3D printer was used instead, to manufacture the required connections made of ABS material. The connectors printed to fit perfectly on each tube while the reducers to fit the connectors on one end and a 32-mm aluminium pipe on the other end (Figure 46). The connectors and reducers were then covered with aluminium foil tape to reflect the incident radiation. These ABS connectors also serve as an insulator that prevents heat being transferred normal to the axis in the tube wall.

The printers basically work on the concept of additive manufacturing. Additive manufacturing is a process used to manufacture part by layers. Layers of materials are formed under computer control to get the final object. This way any complex shape or geometry can be made using 3D printers. These machines are also limited by size, but was sufficient for our application as the reducers and connectors were very small. Hence similar procedure was followed for the connectors, SolidWorks model was created for the connectors and then exported as '.stl' files. These files were then loaded to the program, reoriented, 'build' file was made, and then sliced into layers.

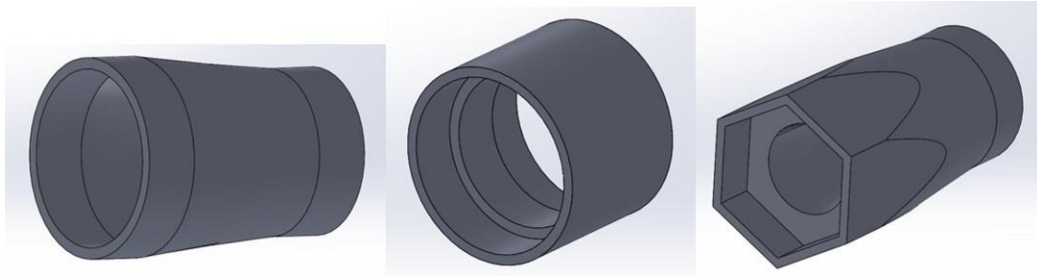


*Figure 46: Reducers and connections for tubes.*

#### **4.5. The Test Rig**

Rubber pipe connected from pump was  $\frac{1}{2}$ " in diameter. This pipe was connected to a  $\frac{3}{4}$ " flow meter via a 32mm aluminium pipe. The aluminium pipe was connected to rubber tube using a brass nozzle plug. Jubilee clip was used to tighten the rubber pipe on the nozzle. The 32mm pipe was 150mm in length, so it could provide enough space for the incoming flow to develop. The 32mm pipe was further connected to the  $\frac{3}{4}$ " flow meter using a threaded socket reducer. The other end of flow meter was having a threaded socket with one end open for 3D printed ABS reducer. Teflon tape was used at each threaded fitting to keep it water tight and red silicon paste was further applied to the joints.

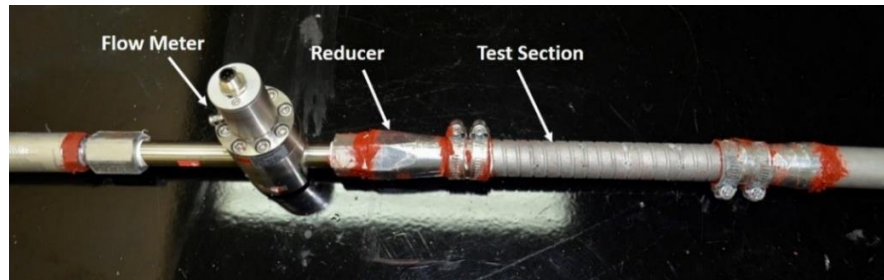


*Figure 47: The test rig.*

The ABS reducer was made watertight in similar fashion, i.e. Teflon tape on inner side and the red silicon paste on outside. The test sample was attached to the ABS reducer and connector, in similar way. The whole rig setup except for flow meter was repeated on the other side of the test sample (Figure 47). 2mm holes were drilled at inlet and outlet of the sample, i.e. in the ABS connectors. The flow meter was kept close to the inlet of test sample so to have the least pressure drop before the water reaches the tube. The control valve was installed before the test section, to prevent high static pressure on the walls of the tube. Such pressure in test section would result in leakage through the thermocouples and increased the risk of rig failure. Jubilee clips were used at the connectors to hold and tightly connect the test sample with the rest of the rig. This rig was designed for vertical flow so it can remain full in low flow rates and also because the central receiver systems have vertical tubes. This vertical rig was kept at the edge of the table in a way that the test section would be housed inside the U-shaped cut in the solar irradiance simulator.

#### 4.5.1. Support for The Rig

The rig was supported by a 6" PVC pipe with an opening on the surface close to ground. This PVC pipe was the same height as the table and was chosen for its ease of mobility. The inlet pipe ran through the opening while the flow meter of the rig rested (and glued) on its upper end. The length of PVC was such that the test sample would end up being inside the solar irradiance simulator box on table (Figure 48). The whole rig was moveable and could be moved closer to the halogen lamps and away.

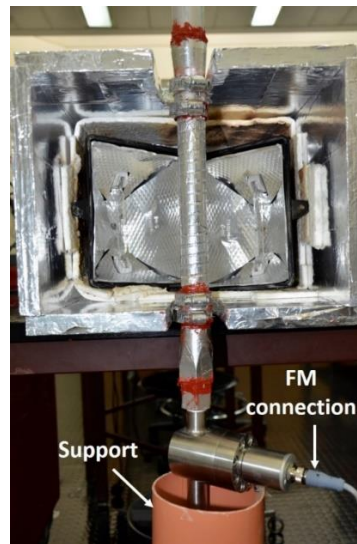


*Figure 48: The rig installed with its support.*



## **4.6. Calibration**

The measurement devices were calibrated before use and a calibration curve was made. The error correction was applied to all the data collected.

### **4.6.1. Thermocouples Calibration**

The thermocouples were calibrated with a mercury thermometer. The thermometer and all thermocouples were placed in boiling water and the readings were recorded while the water boiled and then cooled. The errors at each point were then plotted against temperature and a curve was obtained (Figure 49). These errors were then deduced from all thermocouple readings.

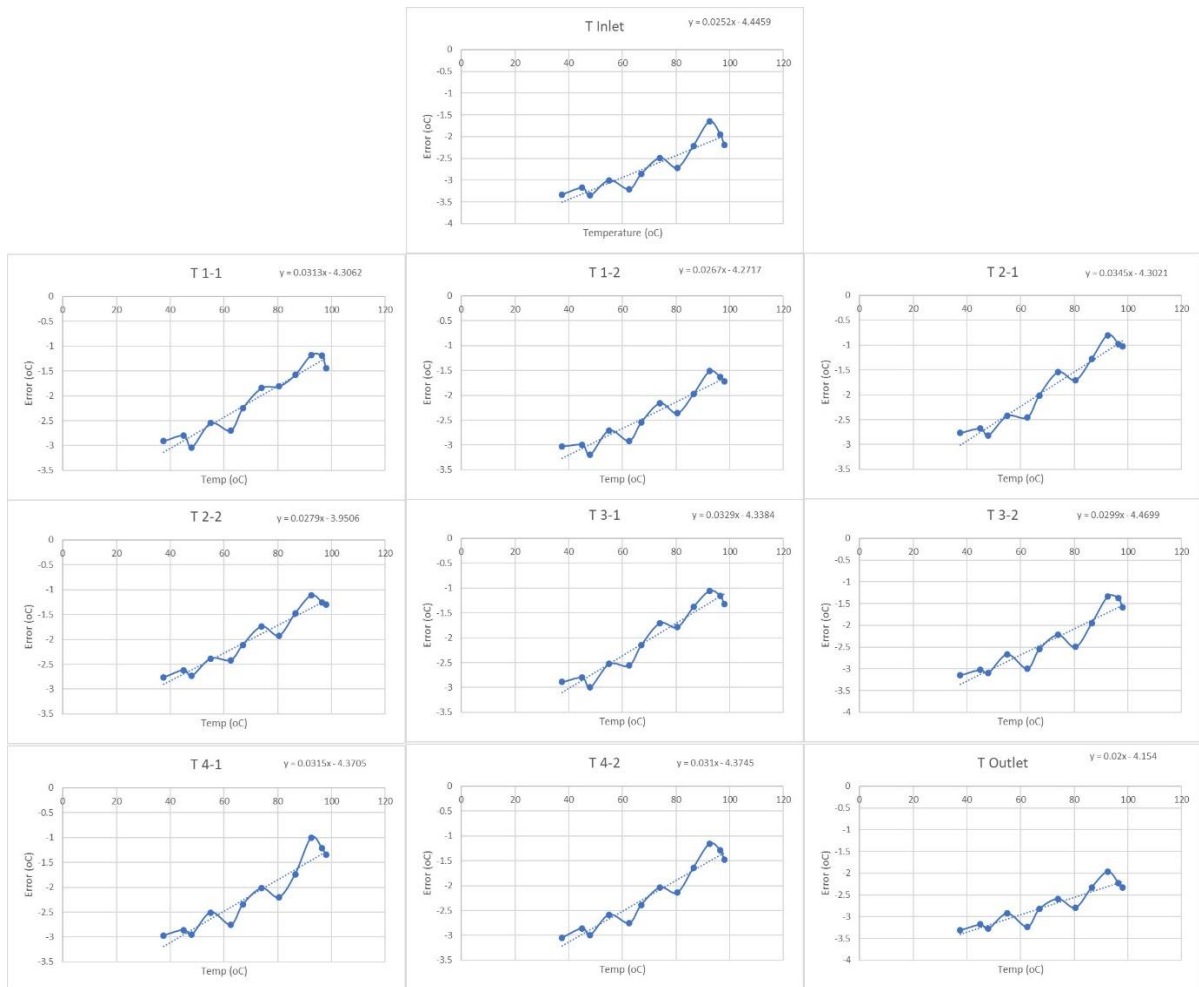
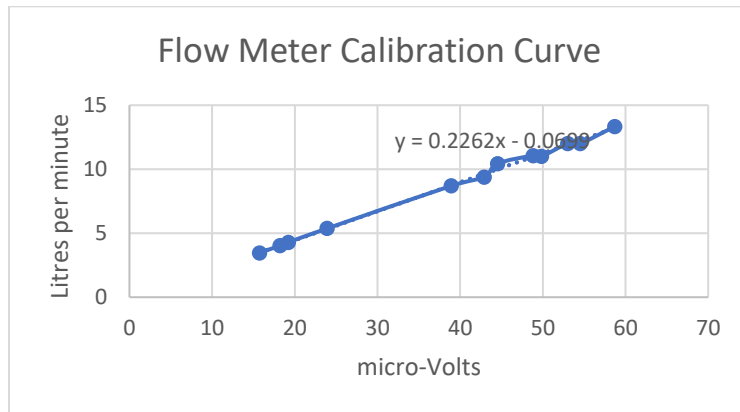


Figure 49: Thermocouples error curves (Temp vs error).

#### 4.6.2. Flow Meter Calibration.

The flow meter was calibrated by using bucket and stop watch method. Each measurement was taken three times and averaged to remove human error in measuring the correct flow rate. The measurements were acquired as volts from the flow meter, which was recorded for

each flow rate. The litres per minute flow rate was then plotted against voltage and the obtained curve was used for error correction in all measurements (Figure 50).



*Figure 50: Flow meter calibration curve.*

The entire loop was set up where parts were fabricated, including the test samples. The measurement devices and their calibration curves are reported here. The leak from tubes hindered operation, which was eventually solved. The results from experiments will be discussed in the chapter 5.

## CHAPTER 5: RESULTS & DISCUSSION

This section will present results for each tube separately and then in comparison. The results are presented as averaged values from thermocouples at each station defined in Figure 40.

### 5.1. CFD Results

#### 5.1.1. Circular Tube

Figure 51 shows temperature contour of water flow through circular tube at 11.5 L/min. The temperature rises gradually towards the outlet. The total change in average temperature is approx. 1.36 K whereas the highest temperature is 294.95 K. This corresponds to a heat transfer of approx. 1300 W which is very close to the value calculated from the experiment at similar flow rate.

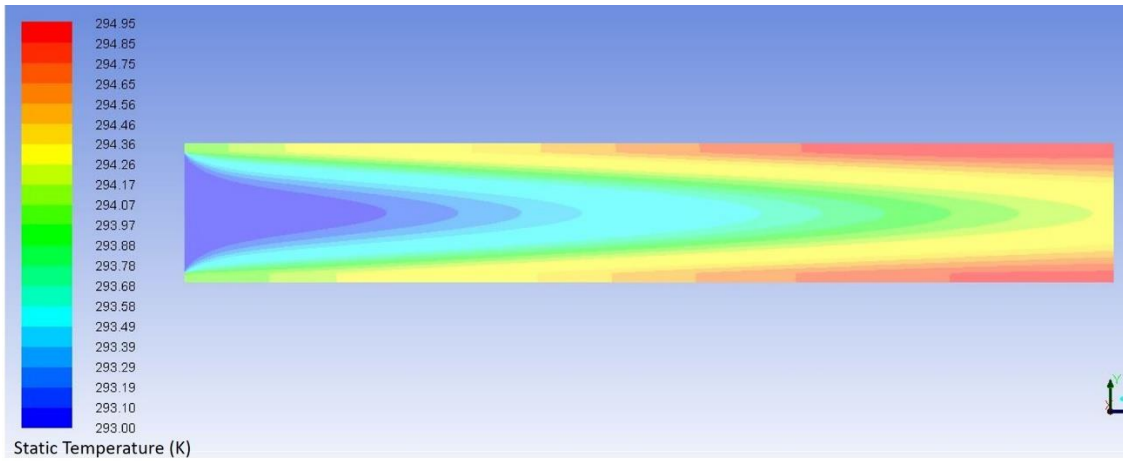


*Figure 51: Temperature contour of flow in Circular Tube.*

The contours for radial velocity, turbulent kinetic energy, and turbulent intensity in circular tube are presented in Figure 52, Figure 53, and Figure 54 respectively. The circular tube has negligible radial velocity but it is used for comparison with other tubes.



Figure 52: Radial Velocity contour of flow in Circular Tube.

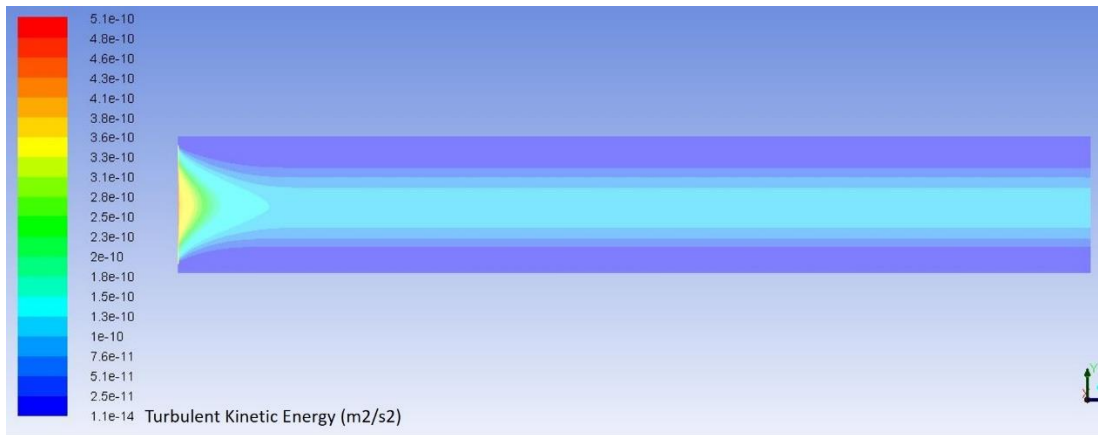
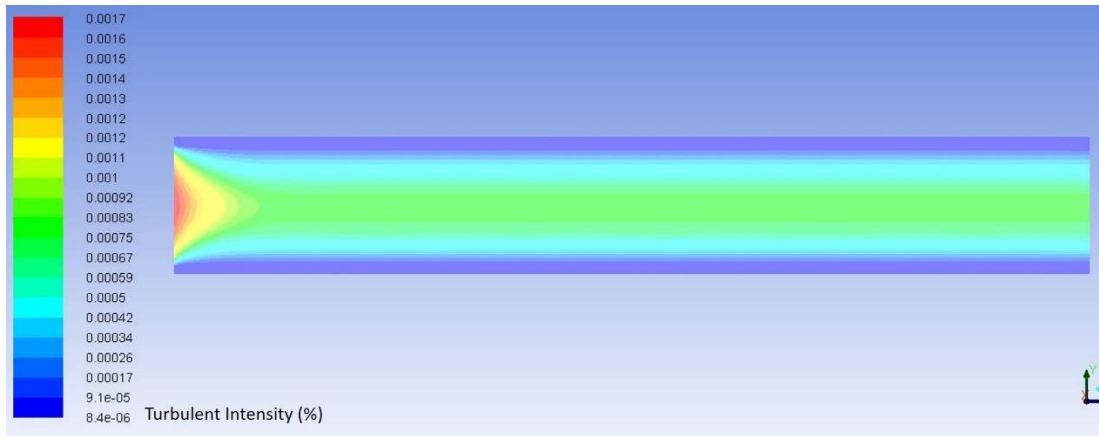


Figure 53: Turbulent Kinetic Energy contour of flow in Circular Tube.



*Figure 54: Turbulent Intensity contour of flow in Circular Tube.*

### **5.1.2. SC-2 Tube**

Figure 55 shows the temperature contour in a of SC-2 Tube at the 11.5 L/min. The temperature rises gradually towards the outlet. The total change in average temperature is approx. 1.22 K whereas the highest temperature is 295.03 K which is higher than the maximum temperature of the circular tube. The average temperature difference corresponds to a heat transfer of approx. 1100 Watts. This is close to the computed heat transfer of circular tube, but higher than the experimental value of SC-2 Tube. This is perhaps due to the uncertainty and errors in the experimental system.

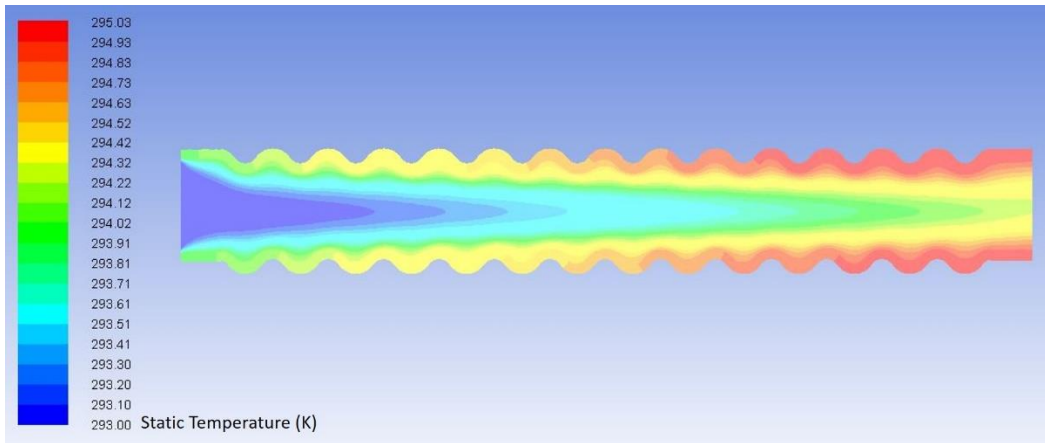


*Figure 55: Temperature contour of flow in SC-2 Tube.*

Figure 56 shows the radial velocity in SC-2 Tube at 11.5 L/min. This contour indicates the turbulence cause by mixing of water near the tube wall. The radial velocities in this tube are higher than the circular tube.



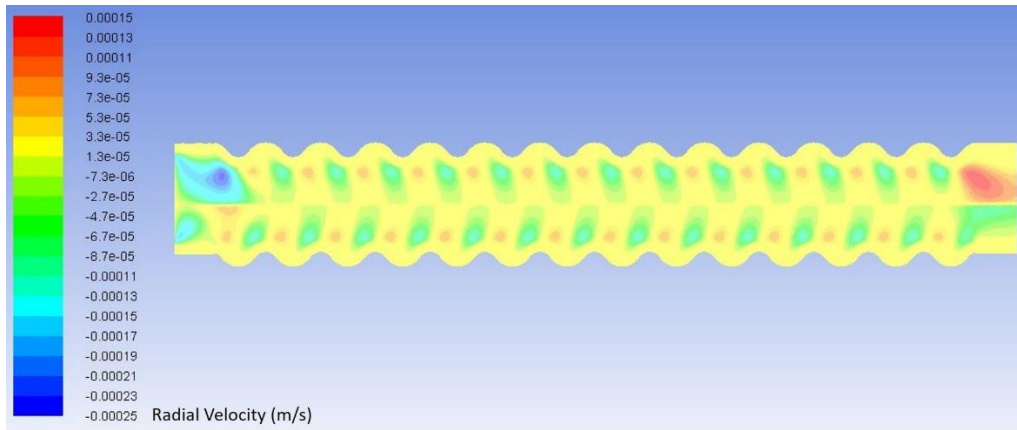


*Figure 56: Radial Velocity contour of flow in SC-2 Tube.*

Figure 57 shows the turbulent intensity contour of flow in SC-2 Tube. At the same flow rate this tube has a higher turbulent intensity than circular. This is caused by the fluid mixing as it flows near the wall.

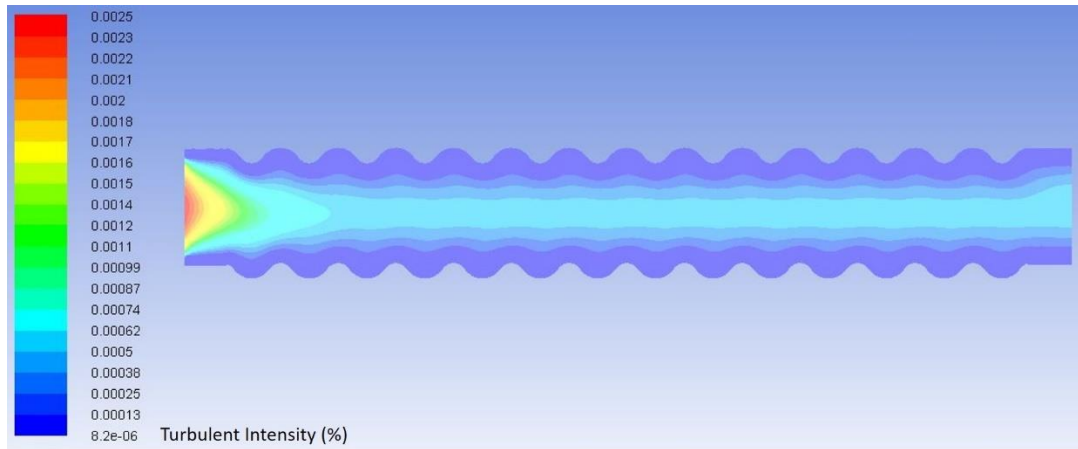


*Figure 57: Turbulent Intensity contour of flow in SC-2 Tube.*

### **5.1.3. WTC Tube**

Figure 58 shows radial velocity in WTC Tube at 11.5 L/min. It is evident from the radial velocity that the flow is more turbulent than circular tube. Although the velocities are higher in pockets close to the tube wall, generally the flow has less mixing as compared to SC-2 Tube. SC-2 has more radial velocity magnitude at many locations inside the tube as compared to WTC Tube.

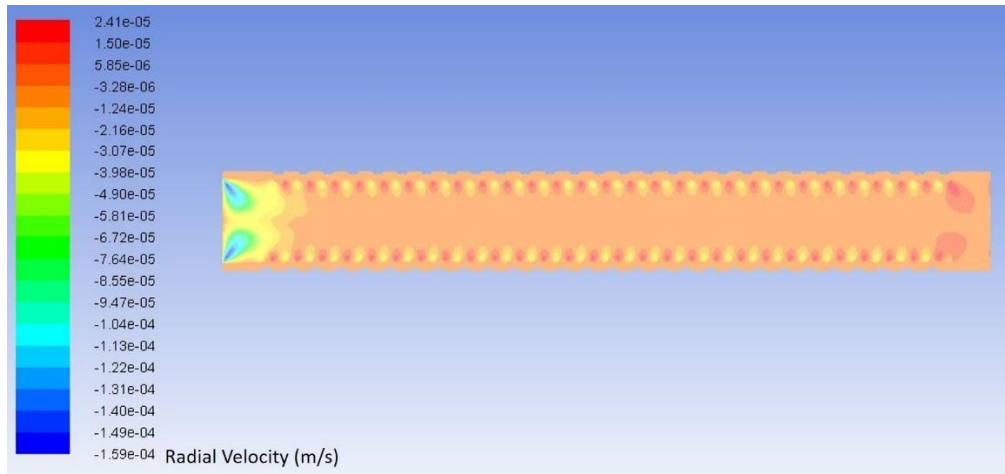


*Figure 58: Radial Velocity contour of flow in WTC Tube.*

#### 5.1.4. SG Tube

Figure 59 shows the temperature contour in SG Tube at 11.5 L/min. The temperature rises gradually towards the outlet. The total change in average temperature is approx. 1.13 K, which corresponds to a heat transfer of approx. 920 Watts. The heat transfer is lower than the value obtained from experimental results. The highest temperature is 294.89 K, which is less than the highest temperature in circular tube.

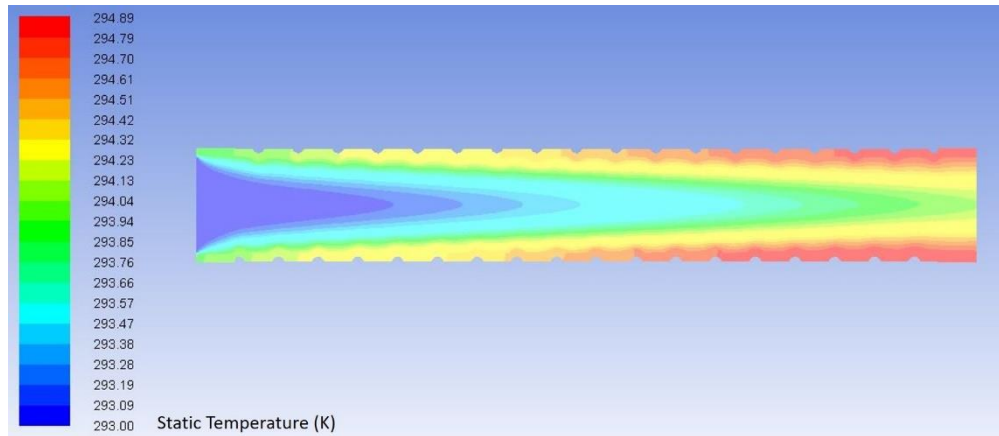


*Figure 59: Temperature contour of flow in SG Tube.*

Figure 60 shows the radial velocity at in SG Tube at 11.5 L/min. The contour indicates to the turbulence caused by mixing of water near the tube wall. The radial velocities in this tube are higher than the circular tube but lower than SC-2 Tube. Even the radial velocity in the grooves at tube wall are lower than the radial velocities in SC-2 Tube.

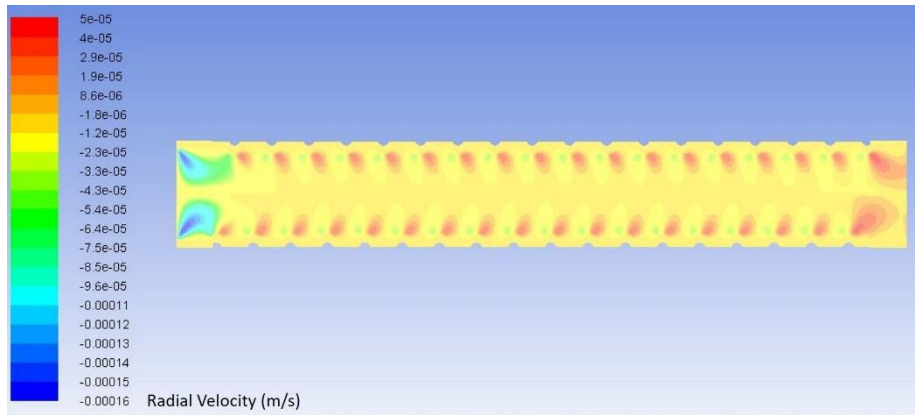


Figure 60: Radial Velocity contour of flow in SG-Tube.

Figure 61 shows the turbulent kinetic energy contour of flow in SG Tube. At the same flow rate this tube has a higher turbulent kinetic energy than circular.

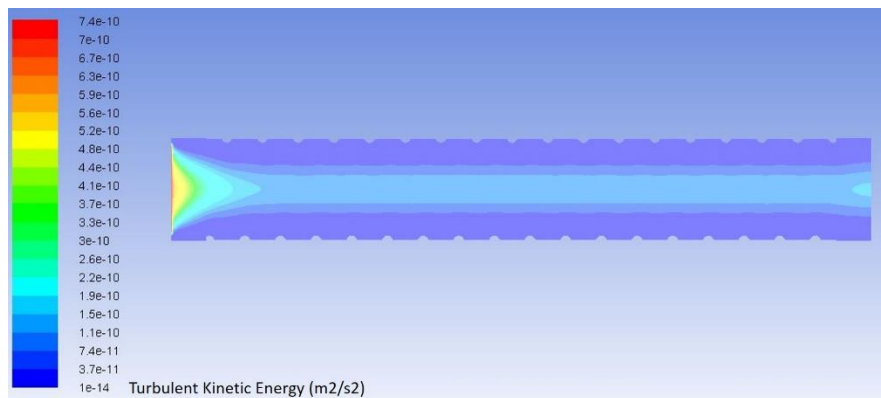
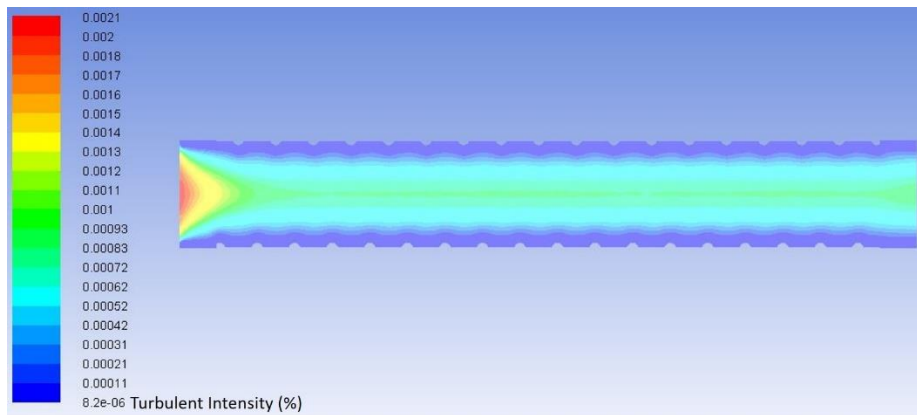


Figure 61: Turbulent Kinetic Energy contour of flow in SG-Tube.

Figure 62 shows the turbulent intensity contour of flow in SG Tube. At the same flow rate this tube has a higher turbulent intensity than circular and slightly higher than the SC-2 Tube. This is caused by the fluid mixing which is the result of fluid hitting the tube wall.



*Figure 62: Turbulent Intensity contour of flow in SG Tube.*

### **5.1.5. Rolo Tube**

Figure 63 shows the temperature contour in Rolo Tube at 11.5 L/min. The temperature rises gradually towards the outlet. The total change in average temperature is approx. 1.13 K, which corresponds to a heat transfer of approx. 1000 Watts. The heat transfer is more than twice as much as the value obtained from experimental results. The highest temperature is 294.90 K, which is less than the highest temperature in circular tube. This difference in

simulation and experiment can be attributed to the uncertainty in thermocouple and low variation in temperature at inlet and outlet of the tubes.

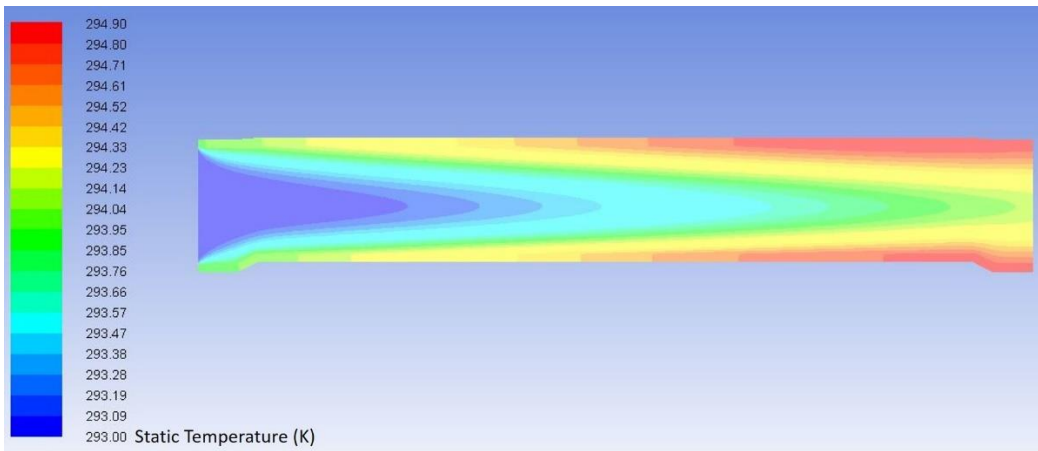


*Figure 63: Temperature contour of flow in Rolo Tube.*

Figure 64 shows the turbulent kinetic energy contour of flow in Rolo Tube. At the same flow rate this tube has a higher turbulent kinetic energy than circular but lower than SG Tube.

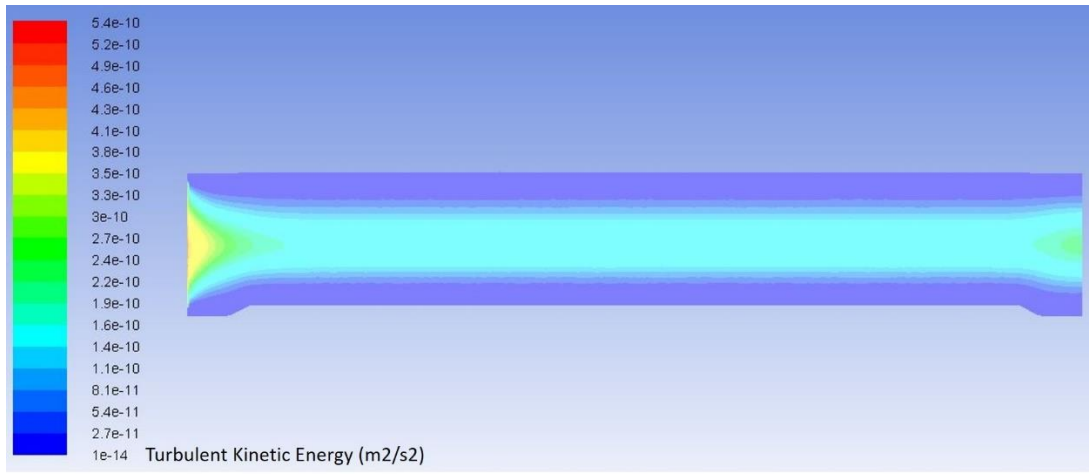


*Figure 64: Turbulent Kinetic Energy contour of flow in Rolo Tube.*

Figure 65 shows the turbulent intensity contour of flow in Rolo Tube. At the same flow rate this tube has a higher turbulent intensity than circular and SC-2 Tube but almost similar to that of SG Tube.



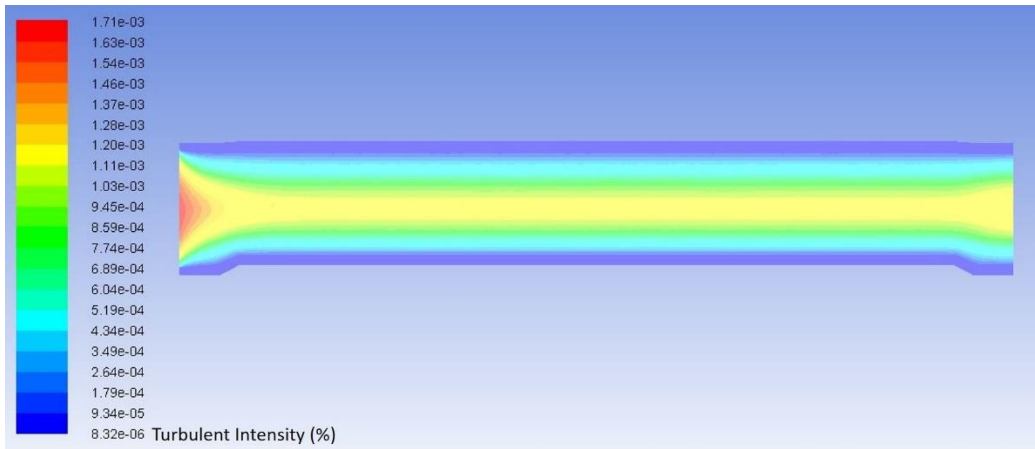


*Figure 65: Turbulent Intensity contour of flow in Rolo Tube.*

Investigation into the turbulence in each tube reveals that radial velocity promotes fluid mixing, hence turbulent kinetic energy. But it depends on the magnitude of the velocities and how much of the bulk has high radial velocities. The tubes SC-2 and SG have the best fluid mixing causing the high turbulent kinetic energy. Meanwhile Rolo tube performs better at mixing than the circular tube, it is comparable to SG tube.

### **5.1.6. Validation**

The Nusselt number for CFD results for circular tube were calculated and compared against the Dittus Boelter equation (Figure 66). At lower flow rates the CFD prediction remains in 10% range of the Dittus Boelter equation between Reynolds number 5000 to approx 7000. CFD under predicts the Nusselt number within a range of 27% of the Dittus Boelter equation from Reynolds number approx. 7000 to 11000.

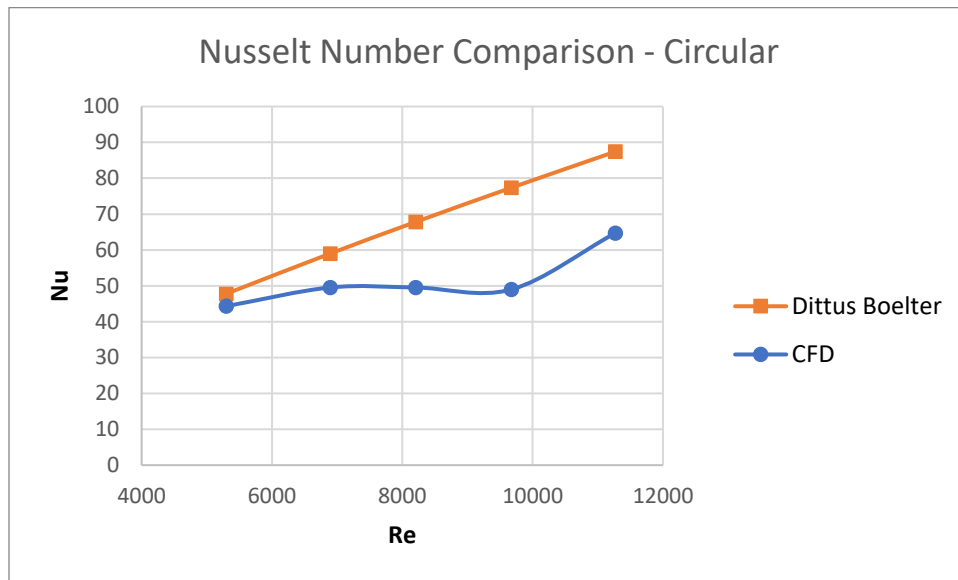


Figure 66: Nusselt Number predicted by CFD vs Dittus Boelter equation.

## 5.2. Experimental Results

This section presents comparison of the experimental results for each tube at each station.

### 5.2.1. Inlet

Figure 67 shows a comparison between all tubes at inlet. It is evident that the inlet remains at same temperature for all tubes because the fluid was regulated to be 20°C using the chiller. There is mild fluctuation in temperatures due to the uncertainty in the thermocouple readings. There is slight variation at high flow rates which can be attributed to the friction caused by turbulent flow.

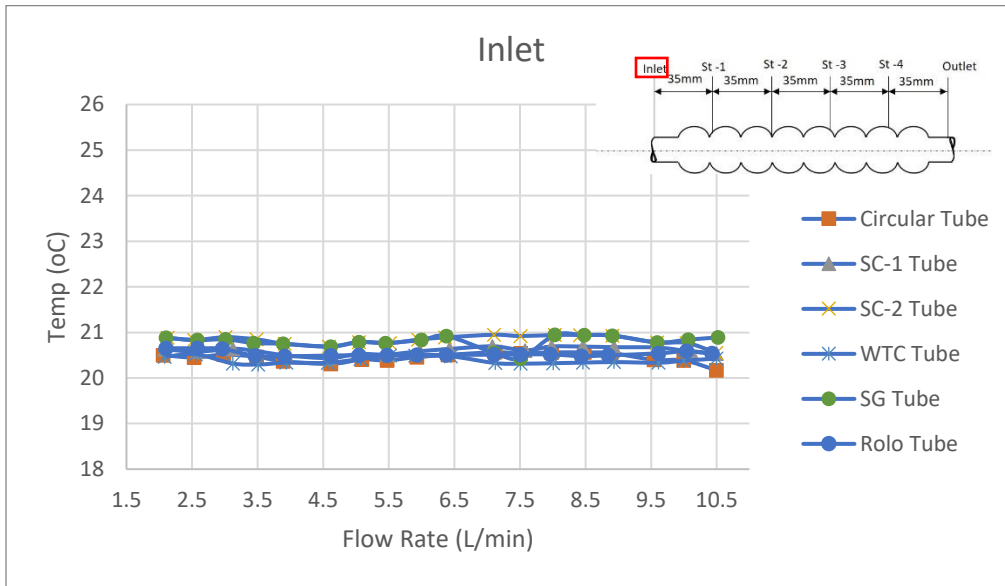


Figure 67: Temperature vs flow rate plot at Inlet of all tubes.

### 5.2.2. Station 1

Figure 68 shows a comparison between all tubes at station 1. SG Tube has the highest temperature at station 1 at low flow rates. SG Tube also has highest heat transfer at extreme high flow rates. WTC Tube has highest temperature at flow rate 6.2 L/min to 9.5 L/min. SC-2 Tube remains at lowest temperatures for all flow rates. Rolo and Circular tubes have lower temperatures than SG Tube, but higher temperature than SC-1 and SC-2 Tubes at all flow rates. Rolo Tube has temperature higher than Circular tube at high flow rates but lower at low flow rates.

The SG Tube has higher temperature at 1<sup>st</sup> station perhaps because the flow close to wall is slow enough to keep water trapped in grooves for longer period. The thermocouple bead is

close to the tube wall, so it records the temperature of almost stagnant fluid. While at higher flow rates the turbulent mixing increases at the grooves and hence the temperature becomes lower. All tubes have very close temperatures at high flow rates except for SC-2 Tube which remains at low temperature at all flow rates. The reason Rolo Tube has higher temperature at high flow rate can be attributed to the turbulent mixing that may occur at the lateral edges of the tube.

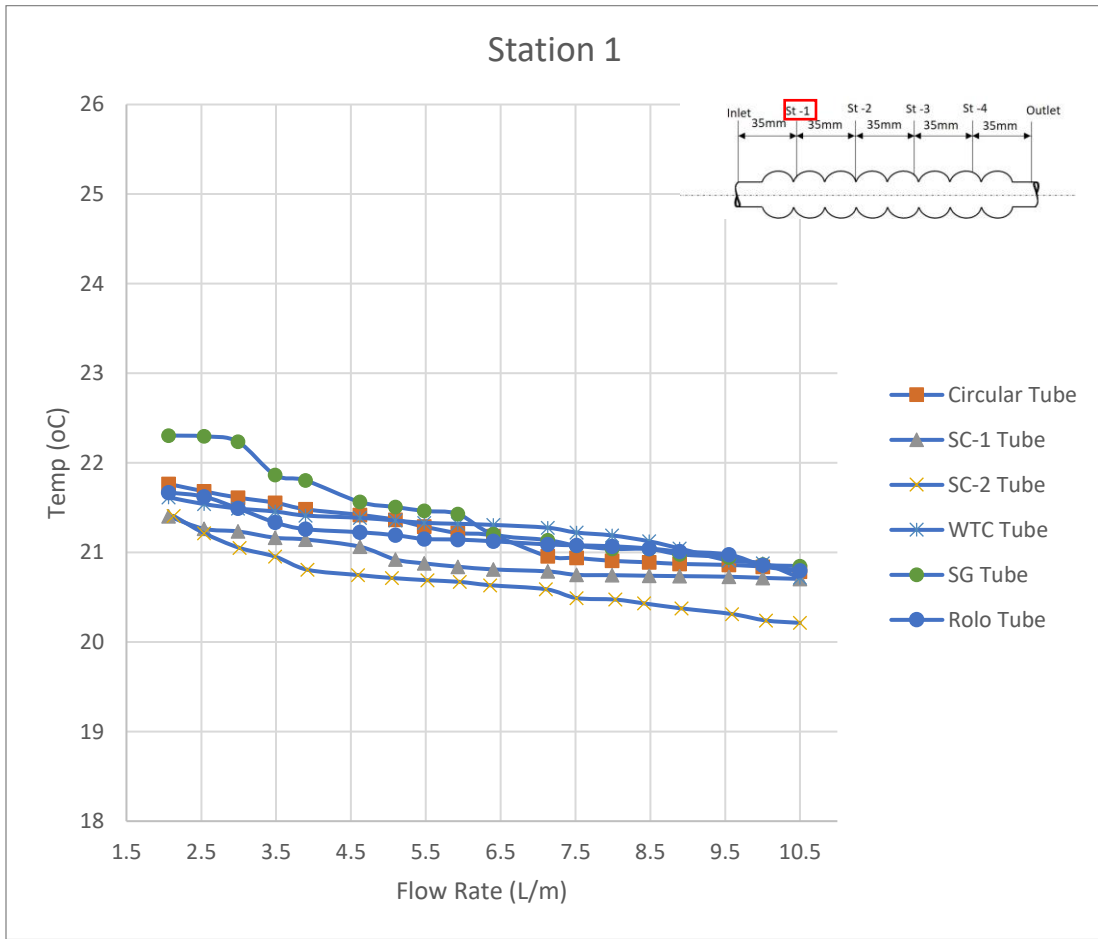


Figure 68: Temperature vs flow rate plot at station 1 of all tubes.

### 5.2.3. Station 2

Figure 69 shows comparison between all tubes temperature vs flow rate plot at station 2. The circular tube remains at highest temperature for all flow rates whereas SC-2 Tube remains at lowest temperature for all flow rates. All other tubes remain in a close range of temperature through all flow rates. This range of temperature narrows down as the flow rate increases.

SG Tube has high temperature than Rolo Tube at low flow rates. SC-1 Tube has higher

temperature than all tubes except the circular tube, at low flow rates while the WTC Tube has higher temperature than all tubes except the circular tube, at flow rates approx. 5 L/min to 9 L/min.

The high temperature at this station shows that heat transfer is faster at all flow rates in circular tube compared to others. One possible explanation is that turbulence in corrugated tubes may be causing read by the thermocouple beads read low temperature close to the tube wall. This can be made certain by further investigating the heat transfer in each tube, which will be presented in section 5.2.7. Furthermore, the reason that WTC Tube performs better than other tubes at moderate flow rates can be attributed to the fact that it has the most irregular wall as compared to others, which may substitute considerable amount of mixing, hence high temperature. Such behaviour may also be attributed to trapped water in the tiny grooves.

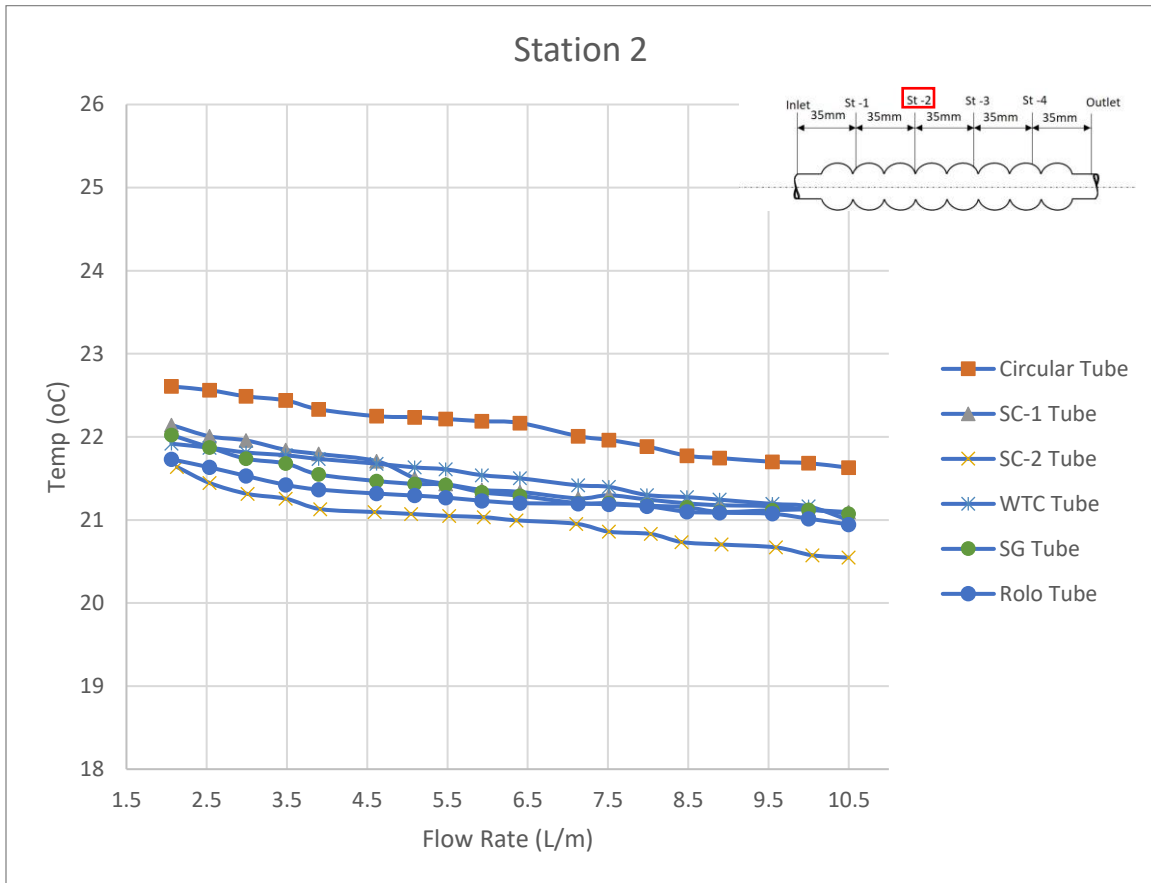


Figure 69: Temperature vs flow rate plot at station 2 of all tubes

### 5.2.4. Station 3

Figure 70 shows the comparison of all tubes temperature vs flow rate plot at station 3. Circular tube has the highest temperature at all flow rates at this station as well. Rolo Tube has the lowest temperature at low flow rates but the temperatures are close to that of SC-2 Tube, especially at high and low flow rates. WTC Tube has higher temperature than all tubes except the circular tube, at flow rates approx. 2 L/min to 8.4 L/min.

Circular tube still gets quickest heat transfer while WTC Tube retains the same effect of having higher temperature at moderate flow rates. This time the effect is amplified and the range is extended. This shows that while fluid flows towards outlet, WTC Tube has more effective heating of fluid than the other tubes at moderate flow rates.



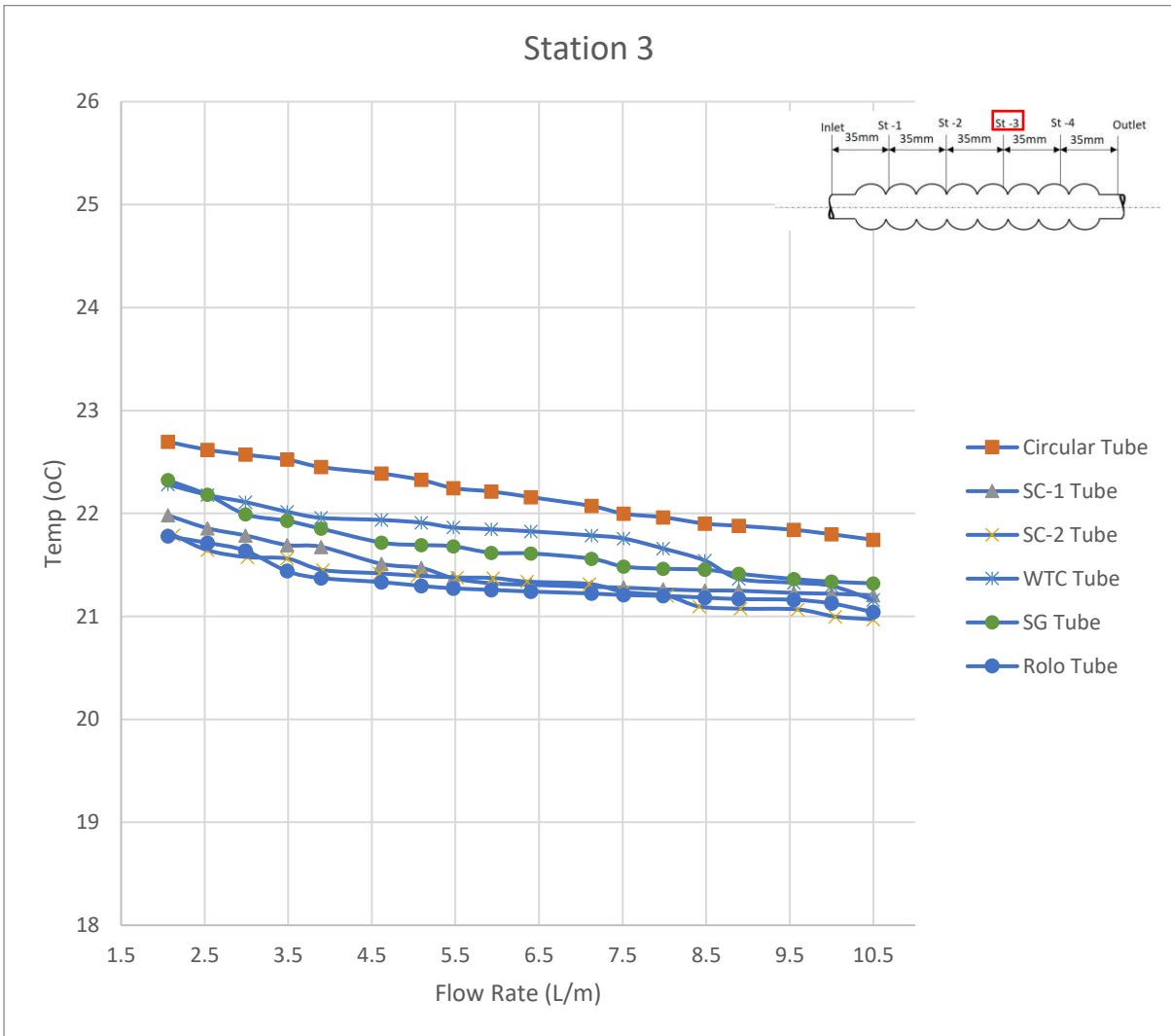


Figure 70: Temperature vs flow rate plot at station 3 of all tubes.

### 5.2.5. Station 4

Figure 71 shows comparison of all tubes in temperature vs flow rate plot at station 4. Circular tube remains best at all flow rates as previous stations. However, the temperature is quite close to that of SC-1 Tube at extreme high flow rate. There is a sharp drop of temperature at

approx. 6.5 L/min. SG Tube has higher temperature than other tubes at low flow rates while at high flow rates, SC-1 Tube has higher temperature than SG Tube. The SC-2 Tube has the lowest temperature rise compared to all tubes at all flow rates. Rolo Tube has higher temperature than SC-2 Tube but lower than all other tubes at all flow rates. The tubes SC-1, WTC, and circular have approx. same temperature at flow rates 7 L/min and higher.

The WTC Tube is not higher temperature at moderate flow rates anymore, as other tubes have higher temperatures at this station. This also indicates that the heat transfer occurs much faster towards this station. The sharp drop in temperature of circular tube at approx. 6.5 L/min may be caused due to the reduction in stagnation of fluid close to wall, which is normal at low flow rates.

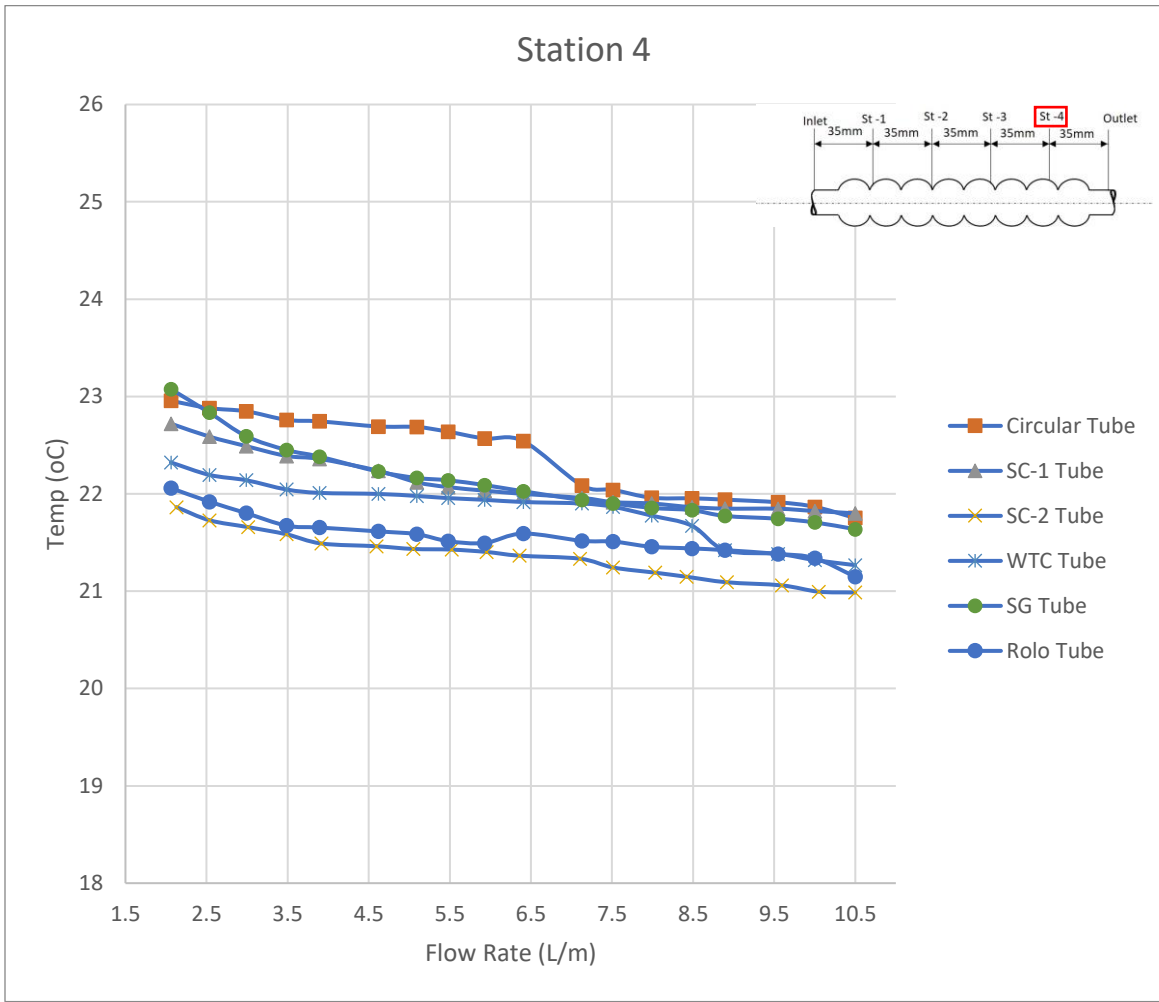


Figure 71:Figure 4: Temperature vs flow rate plot at station 4 of all tubes.

### 5.2.6. Outlet

Figure 72 shows a comparison of temperature vs flow rate at outlet of all tubes. Circular tube has the highest temperature at all flow rates except low flow rates. SG Tube has temperature higher than circular tube at low flow rates. SC-2 Tube remains at lowest temperature for all flow rates whereas Rolo Tube has slightly higher temperatures than SC-2 Tube at all flow

rates. The WTC and SC-1 tubes have temperature values very close at flow rates approx. 7.9 L/min and less. After this flow rate the temperature of SC-1 Tube remains higher.

The Rolo Tube performs poor perhaps because more surface area results in much of the radiation heat going to direct conduction. This heat further spreads out within the tube wall.

More surface area exposed may also result in more radiation reflected, hence lowering the heat transfer to the surface.

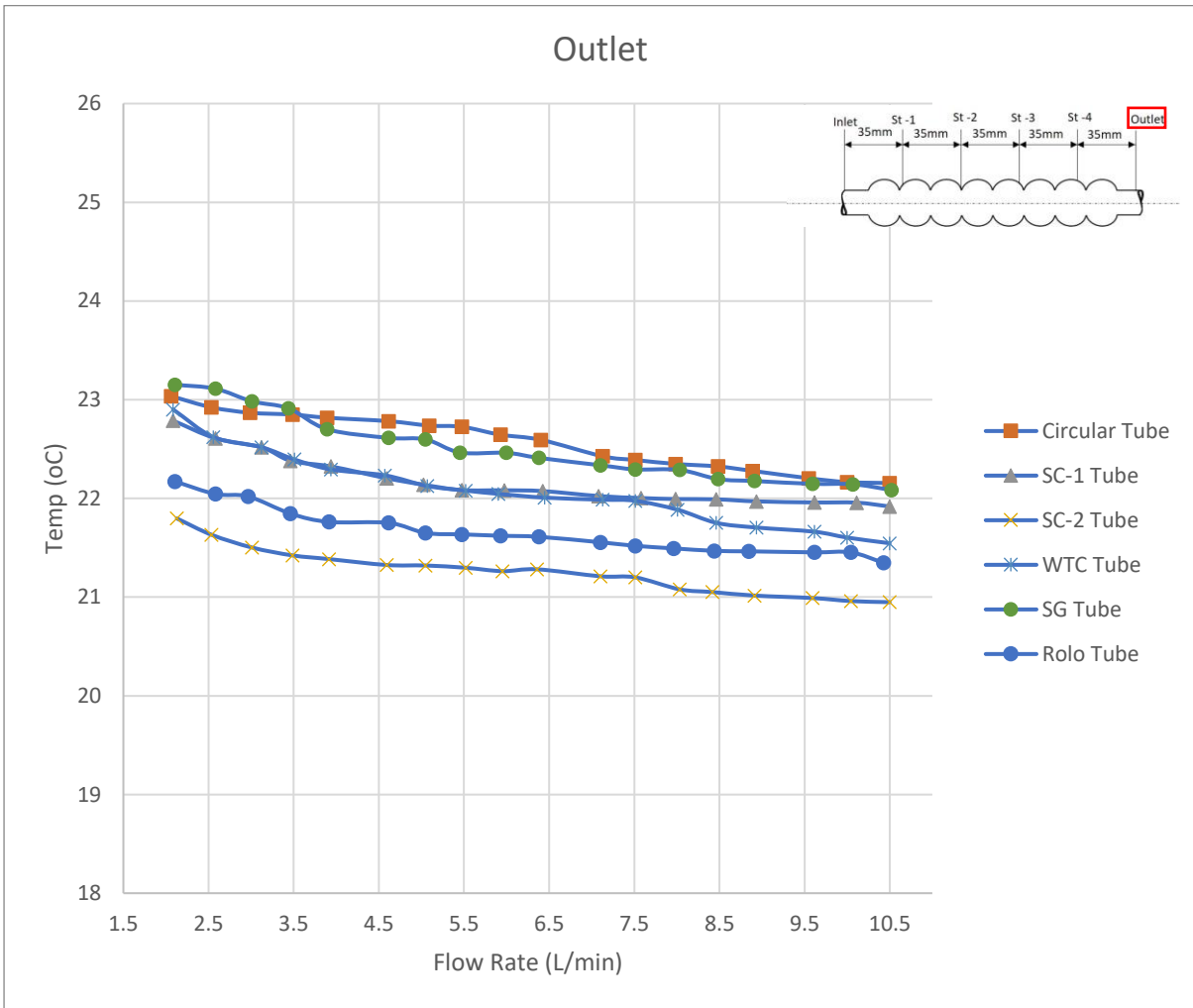


Figure 72: Temperature vs flow rate plot at outlet of all tubes.

### 5.2.7. Heat Transfer in Tubes

Figure 73 shows heat transfer in watts compared to the flow rate in all tubes. This heat transfer is calculated based on the temperature difference between the inlet and outlet while the beads of thermocouples reached the centre of flow. The heat transfer in circular tube

increases linearly until approx. 0.08 Kg/s. Beyond this, it reduces briefly and then increases again at high flow rates. Nevertheless, circular tube has the highest heat transfer than other tubes, i.e. 1,600 Watts which occurs at approx. 0.185 Kg/s.

The SC-1 Tube tube has the second-best heat transfer, after circular tube. The maximum heat transferred is close to that of circular tube, i.e. around 1100 Watts at approx. 0.177 Kg/s. The heat transfer generally increases linearly with the flow rate, with slight fluctuations, but increases sharply at higher flow rate. This may be explained by the turbulent mixing induced at higher Reynolds number.

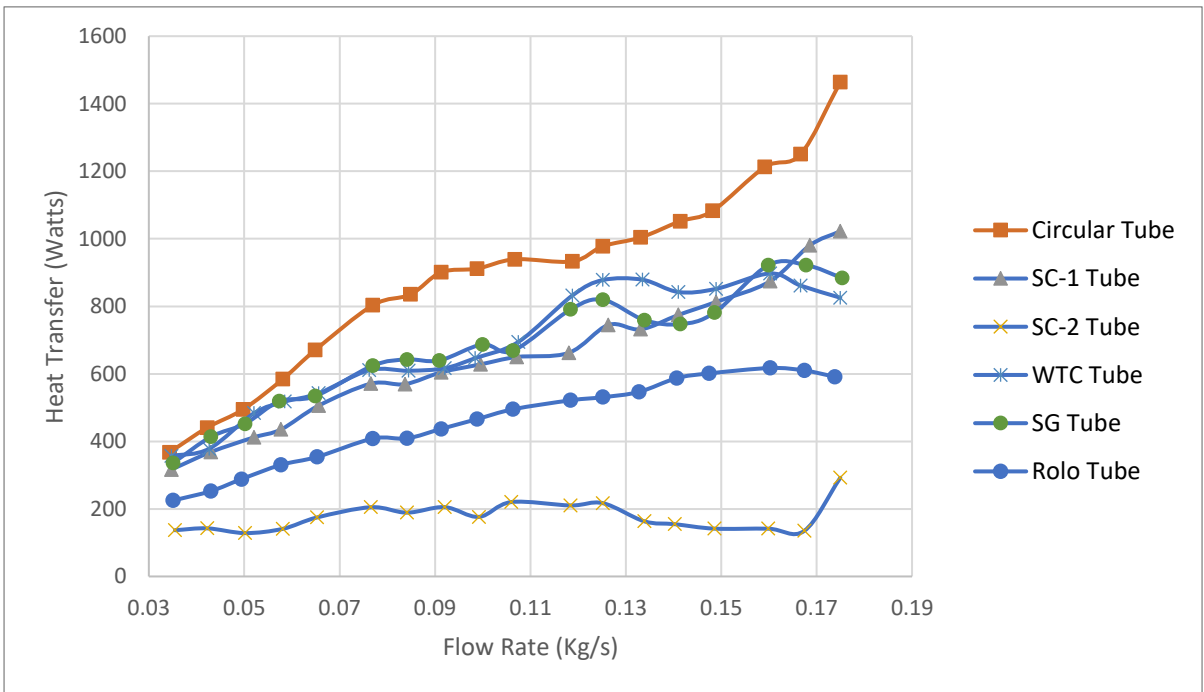


Figure 73: Heat transfer vs. flow rate plot for all tubes.

The SC-2 Tube has lowest heat transfer compared to all tubes. The maximum heat transfer is 400 Watts that occur at approx. 0.18 Kg/min. Previously it was discussed if low temperatures at each station were caused by turbulent mixing near wall. However, it is now clear that this was not the reason, otherwise the outlet temperature would be higher, thus providing higher heat transfer. The overall heat transfer rate is fluctuating without proper trend. The heat transfer rises substantially at higher flow rates.

In WTC Tube, the heat transfer increases with the flow rate with sudden decreases and increases. The heat transfer fluctuates wildly as it approaches higher flow rates. This may be attributed to the uncertainty in measurement of temperatures. The maximum value is around 900 Watts at approx. 0.16 Kg/s. This is still less than the circular tube.

In SG Tube, the maximum heat transfer occurs at approximately 0.17 Kg/s, i.e. close to 950 Watts. This tube performs better than Rolo Tube and WTC Tube. The heat transfer growth remains linear with flow rate till approx. 0.06 Kg/s, from where it starts fluctuating gradually. These fluctuations seem to amplify as the flow rate is increased. The high heat transfer is justified but the lowered heat transfer seems counter intuitive. This may be explained by the turbulent flow profile inside the tubes. It is possible that much of the heat at certain flow rates is lost to the unexposed side of the tube via conduction at higher flow rates.

The heat transfer in Rolo Tube increases with flow rate almost linearly until approx. 0.14 Kg/s where it starts becoming low. The heat transfer value stagnates for one flow rate step at approx. 0.075 Kg/s. The heat transfer also decreases substantially at extreme high temperature. The heat from radiation is transferred directly to the tube wall and then it is transferred via conduction, within the tube wall. The fluid takes this heat before it can be

conducted towards the unexposed portion of the tube. This effect can have negative consequence in Rolo Tube because more surface is exposed to direct radiation, which means there is faster heat conduction within the walls, hence the fluid cannot receive all the heat at higher flow rates. The maximum heat transfer reached by this tube is around 600 Watts at 0.16 Kg/s.

### 5.2.8. Pressure Drop in Tubes

A further observation into pressure drop obtained from simulations may provide a better clue of which tube would be optimum choice if material is the constrain. Figure 74 shows a comparison between pressure drops of all tubes at 10.5 L/min flow rate.

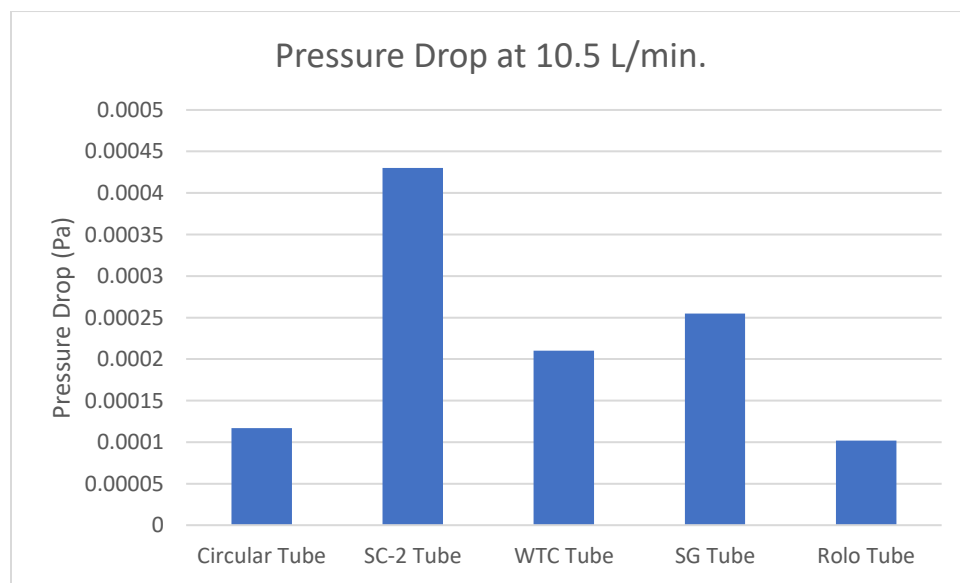


Figure 74: Pressure drop comparison of all tubes.



It is evident that SC-2 tube has the highest pressure drop followed by SG Tube and WTC Tube. Rolo has the least pressure drop compared to all other tubes. This is due to lack of corrugation.

## CHAPTER 6: CONCLUSION & RECOMMENDATIONS

CRS is one of the best CSP technologies that can become cost competitive to fossil fuel in near future. A great deal of research is being conducted by institutions and governments across the world to bring the costs down. One of the many effective research areas is the receiver system. Increasing the efficiency of receiver reduces the cost. This efficiency can be increased by improving the receiver design, improving the heat transfer fluid, or by improving the tubes of receiver for better heat transfer. Passive heat transfer is commonly achieved via corrugation. Corrugation induces fluid mixing that cools the tube walls and transports the energy to heat engine.

Substantial amount of work was previously done in corrugated tubes for various applications. But little work was done in corrugated tubes used in solar irradiation application. This work conducted a literature review and identified many corrugated tubes as options for receiver tube design. Corrugation or other surface modifications usually require the addition of extra material and extra machining. Corrugation also increases the pressure drop. Author chose four tubes with best heat transfer and least pressure drop characteristics and a standard circular tube. A new shape is also compared with these tubes. All tubes were first scaled down so they can have similar surface areas. Similar surface area means similar amount of material used and thus different diameters. In such scenario when the tubes are exposed to radiation, the corrugated tubes will have more surface exposed to radiation than the smooth tube. This study investigates if it is possible to improve heat transfer without having to

increase tube material. This study also aims at testing the potential usefulness of corrugated tubes in CRS or other solar irradiance heat transfer applications.

An experimental set up consisting of fabricated solar irradiance simulator and a test rig were installed in a distilled water flow loop containing a chiller and a control valve. Thermocouples and flow meter were used to measure temperatures and flow rates. The data was recorded using data acquisition system. CFD analysis was also carried to find the pressure difference because the length of actual tubes was very small for recording useful pressure drop. The results were analysed and reported.

It is concluded that the circular tube has performed better than other tubes tested, while the new proposed shape performed better than only one other tube. This is perhaps because keeping surface areas similar in corrugation reduces the diameter of the tube and more surface exposed to irradiation increases the heat lost to conduction within the tube material. However, it is also concluded that corrugated tubes and the new tube design can be used in such systems. The SG Tube and SC-1 Tube also had a very impressive heat transfer performance as compared to other tubes. In summary, the conclusion can be listed as:

- The circular tube provides better heat transfer than the Rolo tube but Rolo tube may be useful for CRS application where least pressure drop is preferred. The Rolo tube is better than only one corrugated tube, i.e. the SC-2 Tube.
- The circular tube provides better heat transfer than the corrugated tubes but corrugated tubes can be useful for CRS application. This is perhaps why traditional CRS have circular tubes rather than corrugated ones. It should be kept in mind that this comparison

is made while keeping the cost of material same, i.e. changing the diameters of tubes without adding more to material cost.

This study was limited in the size of tubes, the heat transfer fluid, and operating temperatures. Further study needs to be carried to investigate these tubes in different lengths, different operating temperatures, and different heat transfer fluids. Nusselt number correlations may be derived for the new tube. Furthermore, liquid metal simulations and experiments need to be carried out on these and other corrugated tubes. Hence the recommendations can be listed as:

- Longer tubes can be used to experimentally investigate the pressure drop in each tube.
- A higher heat flux source can be used to reach higher operating temperatures, which can provide more accurate results. Furthermore, the effect of heat flux may also be investigated.
- Experiments can be carried out using different fluids such as nano-fluids, molten salts and liquid metals, to further investigate the effectiveness of corrugation and the proposed tube design.
- A cost study may also be carried out that can investigate the tube manufacturing costs against the efficiency of receiver.
- Finally, a macro study into efficiency of receiver and cost of the whole system may also be carried for corrugated tubes and for the proposed tube design.

## REFERENCES

- [1] M. K. Hubbert, “Energy from fossil fuels: experiment,” *Science (80-. )*, vol. 109, pp. 103–109, 1949.
- [2] P. Droege, *Urban energy transition : from fossil fuels to renewable power*. Elsevier, 2008.
- [3] J. Yan, S. K. Chou, U. Desideri, and H. G. Jin, “Research, development and innovations for sustainable future energy systems,” *Appl. Energy*, vol. 112, pp. 393–395, 2013.
- [4] T. Nakata, M. Rodionov, D. Silva, and J. Jupesta, “Shift to a low carbon society through energy systems design,” *Sci. China Ser. E Technol. Sci.*, vol. 53, no. 1, pp. 134–143, 2010.
- [5] “World Energy Outlook 2016,” 2016.
- [6] W. Oates, *The RFF Reader in Environmental and Resource Policy*, Second. 2010.
- [7] T. F. Stocker *et al.*, “Climate Change 2013: The Physical Science Basis,” 2013.
- [8] D. B. M. R. Pitz-Paal, “European Concentrated Solar Thermal Road-Mapping,” 2003.
- [9] J. Pacio and T. Wetzel, “Assessment of liquid metal technology status and research paths for their use as efficient heat transfer fluids in solar central receiver systems,”

- Sol. Energy*, vol. 93, pp. 11–22, 2013.
- [10] M. Guarnieri, “A shining tale [Historical],” *IEEE Industrial Electronics Magazine*, vol. 10, no. 4, pp. 67–80, 2016.
- [11] M. Loster, “Total Primary Energy Supply — From Sunlight,” 2006. [Online]. Available: [http://www.ez2c.de/ml/solar\\_land\\_area/](http://www.ez2c.de/ml/solar_land_area/). [Accessed: 11-Oct-2017].
- [12] P. J. Reddy, *Solar Power Generation*. .
- [13] S. V, *General Energetics*. New York, NY (USA); John Wiley and Sons Inc., 1991.
- [14] D. A. Baharoon, H. A. Rahman, W. Z. W. Omar, and S. O. Fadhl, “Historical development of concentrating solar power technologies to generate clean electricity efficiently – A review,” *Renew. Sustain. Energy Rev.*, vol. 41, pp. 996–1027, 2015.
- [15] International Energy Agency, “Solar Energy Perspectives,” 2011.
- [16] M. Becker, *Solar Thermal Central Receiver Systems*. Springer, 1986.
- [17] International Energy Agency, “Technology Roadmap Concentrating Solar Power,” 2010.
- [18] J. Hinkley *et al.*, “Concentrating solar power – drivers and opportunities for cost-competitive electricity.”
- [19] M. Mehos, C. Turchi, and J. Jorgenson, “Advancing Concentrating Solar Power Technology, Performance, and Dispatchability,” 2016.
- [20] G. Kolb, C. Ho, T. Mancini, and J. Gary, “Power Tower Technology Roadmap and

Cost Reduction Plan,” 2011.

- [21] O. Behar, A. Khellaf, and K. Mohammedi, “A review of studies on central receiver solar thermal power plants,” *Renew. Sustain. Energy Rev.*, vol. 23, pp. 12–39, 2013.
- [22] W. Stine and M. Geyer, *Power From The Sun*. John Wiley & Sons, Inc., 2001.
- [23] S. Liu and M. Sakr, “A comprehensive review on passive heat transfer enhancements in pipe exchangers,” *Renew. Sustain. Energy Rev.*, vol. 19, pp. 64–81, 2013.
- [24] M. R. Rodríguez-Sánchez, A. Sánchez-González, C. Marugán-Cruz, and D. Santana, “New designs of molten-salt tubular-receiver for solar power tower,” *Energy Procedia*, vol. 49, pp. 504–513, 2013.
- [25] L. Marocco, G. Cammi, J. Flesch, and T. Wetzel, “Numerical analysis of a solar tower receiver tube operated with liquid metals,” *Int. J. Therm. Sci.*, vol. 105, pp. 22–35, 2016.
- [26] J. Coventry, C. Andraka, J. Pye, M. Blanco, and J. Fisher, “A review of sodium receiver technologies for central receiver solar power plants,” *Sol. Energy*, vol. 122, pp. 749–762, 2015.
- [27] IRENA, “Renewable Energy Technologies Cost Analysis Series: Concentrating Solar Power,” *Compr. Renew. Energy*, vol. 3, no. 2, pp. 595–636, 2012.
- [28] S. A. Kalogirou, “Solar thermoelectric power generation in Cyprus: Selection of the best system,” *Renew. Energy*, vol. 49, pp. 278–281, 2013.

- [29] C. K. Ho, “Advances in central receivers for concentrating solar applications,” *Sol. Energy*, vol. 152, pp. 38–56, 2017.
- [30] L. Yang, R. Zhou, X. Jin, X. Ling, and H. Peng, “Experimental investigate on thermal properties of a novel high temperature flat heat pipe receiver in solar power tower plant,” *Appl. Therm. Eng.*, vol. 109, pp. 610–618, 2016.
- [31] A. Steinfeld, “Solar thermochemical production of hydrogen - A review,” *Sol. Energy*, vol. 78, no. 5, pp. 603–615, 2005.
- [32] W. G. Le Roux, T. Bello-Ochende, and J. P. Meyer, “Operating conditions of an open and direct solar thermal Brayton cycle with optimised cavity receiver and recuperator,” *Energy*, vol. 36, no. 10, pp. 6027–6036, 2011.
- [33] A. Fritsch, R. Uhlig, L. Marocco, C. Frantz, R. Flesch, and B. Hoffschmidt, “A comparison between transient CFD and FEM simulations of solar central receiver tubes using molten salt and liquid metals,” *Sol. Energy*, vol. 155, pp. 259–266, 2017.
- [34] IEA-SSPS-Project, *The IEA/SSPS high flux experiment : testing the advanced sodium receiver at heat fluxes up to 2.5 MW/M<sup>2</sup>*. Springer-Verlag, 1987.
- [35] K. Kanatani, T. Yamamoto, Y. Tamaura, and H. Kikura, “A model of a solar cavity receiver with coiled tubes,” *Sol. Energy*, vol. 153, pp. 249–261, 2017.
- [36] N. Lorenzin and A. Abánades, “A review on the application of liquid metals as heat transfer fluid in Concentrated Solar Power technologies,” *Int. J. Hydrogen Energy*, vol. 41, no. 17, pp. 6990–6995, 2016.



- [37] J. Pacio, C. Singer, T. Wetzel, and R. Uhlig, “Thermodynamic evaluation of liquid metals as heat transfer fluids in concentrated solar power plants,” *Appl. Therm. Eng.*, vol. 60, no. 1–2, pp. 295–302, 2013.
- [38] C. K. Ho and B. D. Iverson, “Review of high-temperature central receiver designs for concentrating solar power,” *Renew. Sustain. Energy Rev.*, vol. 29, pp. 835–846, 2014.
- [39] W. Yu-ting, L. Bin, M. Chong-fang, and G. Hang, “Convective heat transfer in the laminar-turbulent transition region with molten salt in a circular tube,” *Exp. Therm. Fluid Sci.*, vol. 33, no. 7, pp. 1128–1132, 2009.
- [40] S. Y. Wu, L. Xiao, and Y. R. Li, “Effect of aperture position and size on natural convection heat loss of a solar heat-pipe receiver,” *Appl. Therm. Eng.*, vol. 31, no. 14–15, pp. 2787–2796, 2011.
- [41] M. Prakash, S. B. Kedare, and J. K. Nayak, “Investigations on heat losses from a solar cavity receiver,” *Sol. Energy*, vol. 83, no. 2, pp. 157–170, 2009.
- [42] M. Prakash, “Numerical Study of Natural Convection Heat Loss from Cylindrical Solar Cavity Receivers,” *Renew. Energy*, vol. 2014, p. 7, 2014.
- [43] W. Fuqiang, T. Zhexiang, G. Xiangtao, T. Jianyu, H. Huaizhi, and L. Bingxi, “Heat transfer performance enhancement and thermal strain restraint of tube receiver for parabolic trough solar collector by using asymmetric outward convex corrugated tube,” *Energy*, vol. 114, pp. 275–292, 2016.

- [44] W. Fuqiang, L. Qingzhi, H. Huaizhi, and T. Jianyu, "Parabolic trough receiver with corrugated tube for improving heat transfer and thermal deformation characteristics," *Appl. Energy*, vol. 164, pp. 411–424, 2016.
- [45] P. Good, G. Ambrosetti, A. Pedretti, and A. Steinfeld, "An array of coiled absorber tubes for solar trough concentrators operating with air at 600 °C and above," *Sol. Energy*, vol. 111, pp. 378–395, 2015.
- [46] K. Qiu *et al.*, "Simulation and experimental study of an air tube-cavity solar receiver," *Energy Convers. Manag.*, vol. 103, pp. 847–858, 2015.
- [47] J. Zhu, K. Wang, H. Wu, D. Wang, J. Du, and A. G. Olabi, "Experimental investigation on the energy and exergy performance of a coiled tube solar receiver," *Appl. Energy*, vol. 156, pp. 519–527, 2015.
- [48] A. M. Daabo, S. Mahmoud, R. K. Al-Dadah, and A. Ahmad, "Numerical investigation of pitch value on thermal performance of solar receiver for solar powered Brayton cycle application," *Energy*, vol. 119, pp. 523–539, 2017.
- [49] A. M. Daabo, S. Mahmoud, and R. K. Al-Dadah, "The optical efficiency of three different geometries of a small scale cavity receiver for concentrated solar applications," *Appl. Energy*, vol. 179, pp. 1081–1096, 2016.
- [50] R. Loni, A. B. Kasaeian, E. Askari Asli-Ardeh, and B. Ghobadian, "Optimizing the efficiency of a solar receiver with tubular cylindrical cavity for a solar-powered organic Rankine cycle," *Energy*, vol. 112, pp. 1259–1272, 2016.

- [51] M. Neber and H. Lee, "Design of a high temperature cavity receiver for residential scale concentrated solar power," *Energy*, vol. 47, no. 1, pp. 481–487, 2012.
- [52] W. G. Le Roux, T. Bello-Ochende, and J. P. Meyer, "The efficiency of an open-cavity tubular solar receiver for a small-scale solar thermal Brayton cycle," *Energy Convers. Manag.*, vol. 84, pp. 457–470, 2014.
- [53] R. Uhlig, B. Gobereit, and J. Rheinländer, "Advancing Tube Receiver Performance by Using Corrugated Tubes," *Energy Procedia*, vol. 69, pp. 563–572, 2015.
- [54] J. Lu, J. Ding, T. Yu, and X. Shen, "Enhanced heat transfer performances of molten salt receiver with spirally grooved pipe," *Appl. Therm. Eng.*, vol. 88, pp. 491–498, 2015.
- [55] J. Rabas, E. Bergles, and L. Moen, "Heat transfer and pressure drop correlations for spirally grooved (rope) tubes used in surface condensers and multistage flash evaporators," *ASME*, 1988.
- [56] T. S. Ravigururajan and A. E. Bergles, "Development and verification of general correlations for pressure drop and heat transfer in single-phase turbulent flow in enhanced tubes," *Exp. Therm. Fluid Sci.*, vol. 13, no. 1, pp. 55–70, 1996.
- [57] A. Barba, G. Bergeles, I. Demirdzic, A. D. Gosman, and B. E. Launder, "The computation of flow in a spirally fluted tube," *Comput. Methods Appl. Mech. Eng.*, vol. 44, no. 1, pp. 49–65, 1984.
- [58] M. Akugn and N. Parlar, "A flat-plate solar collector with spiral tubing," in

*Proceedings of the Miami International Conference on Alternative Energy*, 1980.

- [59] M. Yang, X. Yang, X. Yang, and J. Ding, “Heat transfer enhancement and performance of the molten salt receiver of a solar power tower,” *Appl. Energy*, vol. 87, no. 9, pp. 2808–2811, 2010.
- [60] O. Garbrecht, F. Al-Sibai, R. Kneer, and K. Wiegardt, “CFD-simulation of a new receiver design for a molten salt solar power tower,” *Sol. Energy*, vol. 90, pp. 94–106, 2013.
- [61] Y. Hong, J. Du, S. Wang, and S. M. Huang, “Heat transfer and flow behaviors of a wavy corrugated tube,” *Appl. Therm. Eng.*, vol. 126, pp. 151–166, 2017.
- [62] H. H. Balla, “Enhancement of heat transfer in six-start spirally corrugated tubes,” *Case Stud. Therm. Eng.*, vol. 9, pp. 79–89, 2017.
- [63] H. Cui, X. Yuan, and Z. Yao, “Experimental Investigation of Heat Transfer and Pressure Drop Characteristics of W-Type Spirally Fluted Tubes,” *Exp. Heat Transf.*, vol. 16, no. 3, pp. 159–169, 2003.
- [64] Z. S. Kareem, M. N. Mohd Jaafar, T. M. Lazim, S. Abdullah, and A. F. Abdulwahid, “Passive heat transfer enhancement review in corrugation,” *Exp. Therm. Fluid Sci.*, vol. 68, pp. 22–38, 2015.
- [65] H. Z. Han, B. X. Li, F. C. Li, and Y. R. He, “RST model for turbulent flow and heat transfer mechanism in an outward convex corrugated tube,” *Comput. Fluids*, vol. 91, pp. 107–129, 2014.

- [66] H.-Z. Han, B.-X. Li, B.-Y. Yu, Y.-R. He, and F.-C. Li, "Numerical study of flow and heat transfer characteristics in outward convex corrugated tubes," *Int. J. Heat Mass Transf.*, vol. 55, no. 25–26, pp. 7782–7802, 2012.
- [67] L. Liebenberg and J. P. Meyer, "In-tube passive heat transfer enhancement in the process industry," *Appl. Therm. Eng.*, vol. 27, pp. 2713–2726, 2007.
- [68] S. Rainieri and G. Pagliarini, "Convective heat transfer to temperature dependent property fluids in the entry region of corrugated tubes," *Int. J. Heat Mass Transf.*, vol. 45, no. 22, pp. 4525–4536, 2002.
- [69] S. K. Saha, "Thermohydraulics of laminar flow through a circular tube having integral helical corrugations and fitted with helical screw-tape insert," *Chem. Eng. Commun.*, vol. 200, no. 3, pp. 418–436, 2013.
- [70] Z. jiang Jin, F. qiang Chen, Z. xin Gao, X. fei Gao, and J. yuan Qian, "Effects of pitch and corrugation depth on heat transfer characteristics in six-start spirally corrugated tube," *Int. J. Heat Mass Transf.*, vol. 108, pp. 1011–1025, 2017.
- [71] Y. Li, J. Wu, H. Wang, L. Kou, and X. Tian, "Fluid Flow and Heat Transfer Characteristics in Helical Tubes Cooperating with Spiral Corrugation," *Energy Procedia*, vol. 17, pp. 791–800, 2012.
- [72] S. Rainieri, F. Bozzoli, and G. Pagliarini, "Experimental investigation on the convective heat transfer in straight and coiled corrugated tubes for highly viscous fluids: Preliminary results," *Int. J. Heat Mass Transf.*, vol. 55, no. 1–3, pp. 498–504,

2012.

- [73] P. Promthaisong, W. Jedsadaratanachai, and S. Eiamsa-Ard, “3D Numerical study on the flow topology and heat transfer characteristics of turbulent forced convection in spirally corrugated tube,” *Numer. Heat Transf. Part A Appl.*, vol. 69, no. 6, pp. 607–629, 2016.
- [74] S. Pal and S. K. Saha, “Experimental investigation of laminar flow of viscous oil through a circular tube having integral axial corrugation roughness and fitted with twisted tapes with oblique teeth,” *Heat Mass Transf.*, vol. 51, no. 8, pp. 1189–1201, 2015.
- [75] L. Liu, X. Ling, and H. Peng, “Analysis on flow and heat transfer characteristics of EGR helical baffled cooler with spiral corrugated tubes,” *Exp. Therm. Fluid Sci.*, vol. 44, pp. 275–284, 2013.
- [76] J. Fernández-Seara and F. J. Uhía, “Heat transfer and friction characteristics of spirally corrugated tubes for outer ammonia condensation,” *Int. J. Refrig.*, vol. 35, no. 7, pp. 2022–2032, 2012.
- [77] A. Kalendar, T. Galal, A. Al-Saftawi, and M. Zedan, “Enhanced tubing thermal performance for innovative MSF system,” *J. Mech. Sci. Technol.*, vol. 25, no. 8, pp. 1969–1977, 2011.
- [78] S. Bhattacharya and S. K. Saha, “Thermohydraulics of laminar flow through a circular tube having integral helical rib roughness and fitted with centre-cleared

- twisted-tape,” *Exp. Therm. Fluid Sci.*, vol. 42, pp. 154–162, 2012.
- [79] Z. S. Kareem, M. N. Mohd Jaafar, T. M. Lazim, S. Abdullah, and A. F. Abdulwahid, “Heat transfer enhancement in two-start spirally corrugated tube,” *Alexandria Eng. J.*, vol. 54, no. 3, pp. 415–422, 2015.
- [80] Z. S. Kareem, S. Abdullah, T. M. Lazim, M. N. Mohd Jaafar, and A. F. Abdul Wahid, “Heat transfer enhancement in three-start spirally corrugated tube: Experimental and numerical study,” *Chem. Eng. Sci.*, vol. 134, pp. 746–757, 2015.
- [81] V. Zimparov, “Enhancement of heat transfer by a combination of a single-start spirally corrugated tubes with a twisted tape,” *Exp. Therm. Fluid Sci.*, vol. 25, no. 7, pp. 535–546, 2002.
- [82] S. Eiamsa-ard, P. Promthaisong, C. Thianpong, M. Pimsarn, and V. Chuwattanakul, “Influence of three-start spirally twisted tube combined with triple-channel twisted tape insert on heat transfer enhancement,” *Chem. Eng. Process. Process Intensif.*, vol. 102, pp. 117–129, 2016.
- [83] T. M. Lazim, Z. S. Kareem, M. N. M. M. Jaafar, S. Abdullah, and A. F. Abdulwahid, “Heat transfer enhancement in spirally corrugated tube,” *Int. Rev. Model. Simulations*, vol. 7, no. 6, pp. 970–978, 2014.
- [84] X. D. Chen, X. Y. Xu, S. K. Nguang, and A. E. Bergles, “Characterization of the Effect of Corrugation Angles on Hydrodynamic and Heat Transfer Performance of Four-Start Spiral Tubes,” *J. Heat Transfer*, vol. 123, no. 6, pp. 1149–1158, 2001.

- [85] S. W. Ahn, "Experimental Studies on Heat Transfer in the Annuli with Corrugated Inner Tubes," *KSME Int. J.*, vol. 17, no. 8, pp. 1226–1233, 2003.
- [86] J. J. Liu, Z. C. Liu, and W. Liu, "3D numerical study on shell side heat transfer and flow characteristics of rod-baffle heat exchangers with spirally corrugated tubes," *Int. J. Therm. Sci.*, vol. 89, pp. 34–42, 2015.
- [87] A. E. Bergles, "1995 Max Jakob Memorial Award Lecture Heat Transfer Enhancement — The Encouragement and Accommodation of High Heat Fluxes," *J. Heat Transfer*, vol. 119, no. 1, pp. 8–19, 1997.
- [88] S. Garimella and R. N. Christensen, "Performance evaluation of spirally fluted annuli: Geometry and flow regime effects," *Heat Transf. Eng.*, vol. 18, no. 1, pp. 34–46, 1997.
- [89] S. Garimella and R. N. Christensen, "Heat Transfer and Pressure Drop Characteristics of Spirally Fluted Annuli: Part II--Heat Transfer," *J. Heat Transfer*, vol. 117, pp. 61–68, 1995.
- [90] I. Taymaz and Y. Islamoglu, "Prediction of convection heat transfer in converging-diverging tube for laminar air flowing using back-propagation neural network," *Int. Commun. Heat Mass Transf.*, vol. 36, no. 6, pp. 614–617, 2009.
- [91] E. Bellos, C. Tzivanidis, K. A. Antonopoulos, and G. Gkinis, "Thermal enhancement of solar parabolic trough collectors by using nanofluids and converging-diverging absorber tube," *Renew. Energy*, vol. 94, pp. 213–222, 2016.



- [92] H. Sadighi Dizaji, S. Jafarmadar, and F. Mobadersani, "Experimental studies on heat transfer and pressure drop characteristics for new arrangements of corrugated tubes in a double pipe heat exchanger," *Int. J. Therm. Sci.*, vol. 96, pp. 211–220, 2015.
- [93] K. Bilen, M. Cetin, H. Gul, and T. Balta, "The investigation of groove geometry effect on heat transfer for internally grooved tubes," *Appl. Therm. Eng.*, vol. 29, no. 4, pp. 753–761, 2009.
- [94] W. Wang, Y. Zhang, B. Li, H. Han, and X. Gao, "Influence of geometrical parameters on turbulent flow and heat transfer characteristics in outward helically corrugated tubes," *Energy Convers. Manag.*, vol. 136, pp. 294–306, 2017.
- [95] M. Li, T. S. Khan, E. Al-Hajri, and Z. H. Ayub, "Single phase heat transfer and pressure drop analysis of a dimpled enhanced tube," *Appl. Therm. Eng.*, vol. 101, pp. 38–46, 2016.
- [96] P. G. Vicente, A. Garc, and A. Viedma, "Heat transfer and pressure drop for low Reynolds turbulent flow in helically dimpled tubes," *Int. J. Heat Mass Transf.*, vol. 45, no. 3, pp. 543–553, 2002.
- [97] A. García, J. P. Solano, P. G. Vicente, and A. Viedma, "The influence of artificial roughness shape on heat transfer enhancement : Corrugated tubes , dimpled tubes and wire coils," *Appl. Therm. Eng.*, vol. 35, pp. 196–201, 2012.
- [98] G. J. Zdaniuk, L. M. Chamra, and P. J. Mago, "Experimental determination of heat transfer and friction in helically-finned tubes," vol. 32, pp. 761–775, 2008.

- [99] A. Özden, H. Demir, Ş. Ö. Atay, F. Kanta, and A. Selim, “Numerical investigation of heat transfer and pressure drop in enhanced tubes,” *Int. Commun. Heat Mass Transf.*, vol. 38, pp. 1384–1391, 2011.
- [100] X. Tang, X. Dai, and D. Zhu, “Experimental and numerical investigation of convective heat transfer and fluid flow in twisted spiral tube,” *Int. J. Heat Mass Transf.*, vol. 90, pp. 523–541, 2015.
- [101] S. Yang, L. Zhang, and H. Xu, “Experimental study on convective heat transfer and flow resistance characteristics of water flow in twisted elliptical tubes,” *Appl. Therm. Eng.*, vol. 31, pp. 2981–2991, 2011.
- [102] X. Tan, D. Zhu, G. Zhou, and L. Zeng, “Experimental and numerical study of convective heat transfer and fluid flow in twisted oval tubes,” *Int. J. Heat Mass Transf.*, vol. 55, no. 17–18, pp. 4701–4710, 2012.
- [103] N. Zheng, W. Liu, Z. Liu, P. Liu, and F. Shan, “A numerical study on heat transfer enhancement and the flow structure in a heat exchanger tube with discrete double inclined ribs,” *Appl. Therm. Eng.*, vol. 90, pp. 232–241, 2015.
- [104] N. Zheng, P. Liu, F. Shan, Z. Liu, and W. Liu, “Heat transfer enhancement in a novel internally grooved tube by generating longitudinal swirl flows with multi-vortexes,” *Appl. Therm. Eng.*, vol. 95, pp. 421–432, 2016.
- [105] D. Ndiaye, “Transient model of a refrigerant-to-water helically coiled tube-in-tube heat exchanger with corrugated inner tube,” *Appl. Therm. Eng.*, vol. 112, pp. 413–

423, 2017.

- [106] L. Yang, H. Han, Y. Li, and X. Li, “A Numerical Study of the Flow and Heat Transfer Characteristics of Outward Convex Corrugated Tubes With Twisted-Tape Insert,” *Heat Transf.*, vol. 138, no. 2, pp. 1–8, 2016.
- [107] S. Rainieri, A. Farina, and G. Pagliarini, “Experimental Investigation of Heat Transfer and Pressure Drop Augmentation for Laminar Flow in Spirally Enhanced Tubes,” in *Proceedings of the 2nd European Thermal-sciences and 14th UIT National Heat Transfer Conference*, 1996, vol. 1, pp. 203–209.
- [108] Y. T. Kang, R. Stout, and R. N. Christensen, “The effects of inclination angle on flooding in a helically fluted tube with a twisted insert,” *Int. J. Multiph. Flow*, vol. 23, no. 6, pp. 1111–1129, 1997.
- [109] S. Rainieri and G. Pagliarini, “Convective heat transfer to orange juice in smooth and corrugated tubes,” *Int. J. Heat Technol.*, vol. 15, no. 2, pp. 69–75, 1997.
- [110] A. Barba, S. Rainieri, and M. Spiga, “Heat transfer enhancement in corrugated tube,” *Int. Commun. Heat Mass Transf.*, vol. 29, no. 3, pp. 313–322, 2002.
- [111] S. K. Saha, “Thermohydraulics of laminar flow through rectangular and square ducts with axial corrugation roughness and twisted tapes with oblique teet,” *J. Heat Transfer*, vol. 132, p. 12, 2010.
- [112] S. K. Saha, B. N. Swain, and G. L. Dayanidhi, “Friction and thermal characteristics of laminar flow of viscous oil through a circular tube having axial corrugations and

- fitted with helical screw-tape inserts,” *J. Fluids Eng.*, vol. 134, 2012.
- [113] S. Rainieri, F. Bozzoli, L. Cattani, and G. Pagliarini, “Compound convective heat transfer enhancement in helically coiled wall corrugated tubes,” *Int. J. Heat Mass Transf.*, vol. 59, pp. 353–362, 2013.
- [114] L. Vulchanov and V. D. Zimparov, “Heat transfer and friction characteristics of spirally corrugated tubes for power plant condensers-2 . A mixing-length model for predicting fluid friction and heat transfer,” *Int. J. Heat Mass Transf.*, vol. 34, no. 9, pp. 2199–2206, 1991.
- [115] V. D. Zimparov and N. L. Vulchanov, “Heat transfer and friction characteristics of spirally corrugated tubes for power plant condensers- 1 . Experimental investigation and performance evaluation,” *Engineering*, 1990.
- [116] S. Nozu, H. Honda, and H. Nakata, “Condensation of Refrigerants CFC11 and CFC113 in the Annulus of a Double-Tube Coil with an Enhanced Inner Tube,” *Exp. Therm. Fluid Sci.*, vol. 11, no. 1, pp. 40–51, 1995.
- [117] S. M. Macbain, A. E. Bergles, and S. Raina, “Heat transfer and pressure drop characteristics of flow boiling in a horizontal deep spirally fluted tube,” *HVAC&R*, vol. 3, no. 1, pp. 65–80, 1997.
- [118] S. C. Lee, S. C. Nam, and T. G. Ban, “Performance of Heat Transfer and Pressure Drop in a Spirally Indented Tube,” *KSME Int. J.*, vol. 12, no. 5, pp. 917–925, 1998.
- [119] M. M. Salim, D. M. France, and C. B. Panchal, “Heat transfer enhancement on outer

- surface of spirally indented tubes,” *Enhanc. Heat Transf.*, vol. 6, pp. 327–341, 1999.
- [120] L. Wang, D. Sun, P. Liang, L. Zhuang, and Y. Tan, “Heat transfer characteristics of carbon steel spirally fluted tube for high pressure preheaters,” *Energy Convers. Manag.*, vol. 41, pp. 993–1005, 2000.
- [121] H. Wu, H. Cheng, and Q. Zhou, “Compound enhancement heat transfer inside tubes by combined use of spirally corrugated tube and inlet axial vane swirlers,” *Enhanc. Heat Transf.*, vol. 7, pp. 247–257, 2000.
- [122] Y. Dong, L. Huixiong, and C. Tingkaun, “Pressure drop, heat transfer and performance of single-phase turbulent flow in spirally corrugated tubes,” *Exp. Fluid Sci.*, vol. 24, pp. 131–138, 2001.
- [123] Y. Qi, Y. Kawaguchi, Z. Lin, M. Ewing, R. N. Christensen, and J. L. Zakin, “Enhanced heat transfer of drag reducing surfactant solutions with fluted tube-in-tube heat exchanger,” *Int. J. Heat Mass Transf.*, vol. 44, no. 8, pp. 1495–1505, 2001.
- [124] V. Zimparov, “Enhancement of heat transfer by a combination of three-start spirally corrugated tubes with a twisted tape,” *Int. J. Heat Mass Transf.*, vol. 44, no. 3, pp. 551–574, 2001.
- [125] K. Hwang *et al.*, “Heat transfer and pressure drop characteristics of enhanced titanium tubes,” *Desalination*, vol. 159, no. 1, pp. 33–41, 2003.
- [126] P. G. Vicente, A. García, and A. Viedma, “Mixed convection heat transfer and isothermal pressure drop in corrugated tubes for laminar and transition flow,” *Int.*

*Commun. Heat Mass Transf.*, vol. 31, no. 5, pp. 651–662, 2004.

- [127] P. G. Vicente, A. García, and A. Viedma, “Experimental investigation on heat transfer and frictional characteristics of spirally corrugated tubes in turbulent flow at different Prandtl numbers,” *Int. J. Heat Mass Transf.*, vol. 47, no. 4, pp. 671–681, 2004.
- [128] W. Targanski and J. T. Cieslinski, “Evaporation of R407C/oil mixtures inside corrugated and micro-fin tubes,” *Appl. Therm. Eng.*, vol. 27, no. 13, pp. 2226–2232, 2007.
- [129] S. Laohalertdecha and S. Wongwises, “The effects of corrugation pitch on the condensation heat transfer coefficient and pressure drop of R-134a inside horizontal corrugated tube,” *Int. J. Heat Mass Transf.*, vol. 53, no. 13–14, pp. 2924–2931, 2010.
- [130] S. K. Saha, “Thermohydraulics of turbulent flow through rectangular and square ducts with axial corrugation roughness and twisted-tapes with and without oblique teeth,” *Exp. Therm. Fluid Sci.*, vol. 34, no. 6, pp. 744–752, 2010.
- [131] K. Aroonrat and S. Wongwises, “Evaporation heat transfer and friction characteristics of R-134a flowing downward in a vertical corrugated tube,” *Exp. Therm. Fluid Sci.*, vol. 35, no. 1, pp. 20–28, 2011.
- [132] S. Laohalertdecha, A. S. Dalkilic, and S. Wongwises, “Correlations for evaporation heat transfer coefficient and two-phase friction factor for R-134a flowing through

- horizontal corrugated tubes,” *Int. Commun. Heat Mass Transf.*, vol. 38, no. 10, pp. 1406–1413, 2011.
- [133] S. Laohalertdecha and S. Wongwises, “An experimental study into the evaporation heat transfer and flow characteristics of R-134a refrigerant flowing through corrugated tubes,” *Int. J. Refrig.*, vol. 34, no. 1, pp. 280–291, 2011.
- [134] S. Laohalertdecha and S. Wongwises, “Condensation heat transfer and flow characteristics of R-134a flowing through corrugated tubes,” *Int. J. Heat Mass Transf.*, vol. 54, no. 11–12, pp. 2673–2682, 2011.
- [135] S. Pethkool, S. Eiamsa-ard, S. Kwankaomeng, and P. Promvonge, “Turbulent heat transfer enhancement in a heat exchanger using helically corrugated tube,” *Int. Commun. Heat Mass Transf.*, vol. 38, no. 3, pp. 340–347, 2011.
- [136] A. A. R. Darzi, M. Farhadi, K. Sedighi, R. Shafaghat, and K. Zabihi, “Experimental investigation of turbulent heat transfer and flow characteristics of SiO<sub>2</sub>/water nanofluid within helically corrugated tubes,” *Int. Commun. Heat Mass Transf.*, vol. 39, no. 9, pp. 1425–1434, 2012.
- [137] D. Khoeini, M. A. Akhavan-Behabadi, and A. Saboonchi, “Experimental study of condensation heat transfer of R-134a flow in corrugated tubes with different inclinations,” *Int. Commun. Heat Mass Transf.*, vol. 39, no. 1, pp. 138–143, 2012.
- [138] K. Wongcharee and S. Eiamsa-ard, “Heat transfer enhancement by using CuO/water nanofluid in corrugated tube equipped with twisted tape,” *Int. Commun. Heat Mass*

- Transf.*, vol. 39, no. 2, pp. 251–257, 2012.
- [139] K. Aroonrat, C. Jumholkul, R. Leelaprachakul, A. S. Dalkilic, O. Mahian, and S. Wongwises, “Heat transfer and single-phase flow in internally grooved tubes,” *Int. Commun. Heat Mass Transf.*, vol. 42, pp. 62–68, 2013.
- [140] C. Chen, Y. T. Wu, S. T. Wang, and C. F. Ma, “Experimental investigation on enhanced heat transfer in transversally corrugated tube with molten salt,” *Exp. Therm. Fluid Sci.*, vol. 47, pp. 108–116, 2013.
- [141] J. Lu, X. Sheng, J. Ding, and J. Yang, “Transition and turbulent convective heat transfer of molten salt in spirally grooved tube,” *Exp. Therm. Fluid Sci.*, vol. 47, pp. 180–185, 2013.
- [142] P. Poredoš, T. Šuklje, S. Medved, and C. Arkar, “An experimental heat-transfer study for a heat-recovery unit made of corrugated tubes,” *Appl. Therm. Eng.*, vol. 53, no. 1, pp. 49–56, 2013.
- [143] M. A. Akhavan-Behabadi and M. Esmailpour, “Experimental study of evaporation heat transfer of R-134a inside a corrugated tube with different tube inclinations,” *Int. Commun. Heat Mass Transf.*, vol. 55, pp. 8–14, 2014.
- [144] M. Balcilar, A. S. Dalkilic, A. C. Sonmez, and S. Wongwises, “Classification of in-tube boiling R134a data belonging to the smooth and corrugated tubes,” *Int. Commun. Heat Mass Transf.*, vol. 53, pp. 185–194, 2014.
- [145] A. A. Rabienataj Darzi, M. Farhadi, and K. Sedighi, “Experimental investigation of



convective heat transfer and friction factor of Al<sub>2</sub>O<sub>3</sub>/water nanofluid in helically corrugated tube,” *Exp. Therm. Fluid Sci.*, vol. 57, pp. 188–199, 2014.

[146] P. S. Kathait and A. K. Patil, “Thermo-hydraulic performance of a heat exchanger tube with discrete corrugations,” *Appl. Therm. Eng.*, vol. 66, no. 1–2, pp. 162–170, 2014.

[147] S. Laohalertdecha, K. Aroonrat, A. S. Dalkilic, O. Mahian, S. Kaewnai, and S. Wongwises, “Prediction of heat transfer coefficients and friction factors for evaporation of R-134a flowing inside corrugated tubes,” *Heat Mass Transf. und Stoffuebertragung*, vol. 50, no. 4, pp. 469–482, 2014.

[148] ANSYS, *ANSYS FLUENT 12.0 User’s Guide*. 2012.

[149] G. K. (George K. Batchelor, *An Introduction to Fluid Dynamics*. Cambridge University Press, 1999.